Intelligent Fault Location for Smart Power Grids

Hanif Livani

Dissertation submitted to the faculty of the Virginia Polytechnic Institute and State University in partial fulfillment of the requirements for the degree of

Doctor of Philosophy
in
Electrical Engineering

Cansin Yaman Evrenosoglu, Co-Chair
Jaime De La Reelopez, Co-Chair
Virgilio A. Centeno
William T. Baumann
Serkan Gugercin

March 6 2014
Blacksburg, VA

Keywords: Fault Location, Fault Classification, Smart Power Grids, Support Vector Machines, Traveling Waves, Wavelet Transformation

Intelligent Fault Location for Smart Power Grids

Hanif Livani

ABSTRACT

Modernized and advanced electricity transmission and distribution infrastructure ensures reliable, efficient, and affordable delivery of electric power. The complexity of fault location problem increases with the proliferation of unusual topologies and with the advent of renewable energy-based power generation in the smart grid environment. The proliferation of new Intelligent Electronic Devices (IEDs) provides a venue for the implementation of more accurate and intelligent fault location methods. This dissertation focuses on intelligent fault location methods for smart power grids and it aims at improving fault location accuracies and decreasing the cost and the mean time to repair damaged equipment in major power outages subsequently increasing the reliability of the grid.

The developed methods utilize wavelet transformation to extract the traveling wave information in the very fast voltage and current transients which are initiated immediately after a fault occurs, support vector machines to classify the fault type and identify the faulted branches and finally Bewley diagrams to precisely locate the fault. The approach utilizes discrete wavelet transformation (DWT) for analysis of transient voltage and current measurements. The transient wavelet energies are calculated and utilized as the input for support vector machine (SVM) classifiers. SVM learns the mapping between

inputs (i.e. transient voltages and/or currents wavelet energies) and desired outputs (i.e. faulty phase and/or faulty section) through processing a set of training cases.

This dissertation presents the proposed methodologies applied to three complex power transmission systems. The first transmission system is a three-terminal (teed) three-phase AC transmission network, a common topology in high- and extra high-voltage networks. It is used to connect three substations that are wide apart from each other through long transmission lines with a 'tee' point, which is not supported by a substation nor equipped with a measuring device. The developed method overcomes the difficulties introduced by the discontinuity: the tee point. The second topology is a hybrid high voltage alternative current (HVAC) transmission line composed of an overhead line combined with an underground cable. The proposed fault location method is utilized to overcome the difficulties introduced by the discontinuity at the transition point from the overhead line to the underground cable and the different traveling wave velocities along the line and the cable. The third topology is a segmented high voltage direct current (HVDC) transmission line including an overhead line combined with an underground cable. This topology is widely utilized to transmit renewable energy-based electrical power from remote locations to the load centers such as from off-shore wind farms to on-shore grids.

This dissertation introduces several enhancements to the existing fault type and fault location algorithms: improvement in the concept of fault type classification and faulty section identification by using SVMs with smaller inputs and improvements in the fault location in the complex configurations by utilizing less measurements from the terminals.

To my Father Morteza Livani, my lifetime inspiration,
and my beloved Mother Asieh Saffar

Acknowledgements

I would like to express my sincere gratitude to my advisor, Dr. Cansin Yaman Evrenosoglu for his significant role in my life. He provided me with guidance, inspiration, motivation and continuous support throughout my Ph.D. studies. I am also very grateful for his friendship and patience during all these years.

In addition, I would like to thank other members of my dissertation committee, Dr. Jaime De La Reelopez, Dr. Virgilio A. Centeno, Dr. William T. Baumann and Dr. Serkan Gugercin, for their precious time, valuable comments and suggestions during my studies.

One of the most effective factors deciding the success of one's research is the ambience of the lab one works in, and in this case, I am really fortunate to have as amazing officemates as Mohammad Hassanzadeh and Anibal Sanjab for these years in the Center for Power & Energy. I also thank all my past and present labmates.

I would also like to thank all my friends in Blacksburg, especially Reza Arghandeh and Reza Sarlak, for their encouragement and companionship. Their kindness and sense of humor helped me to get away from my studies and survive during all these years.

I don't want to miss the chance to thank Siavash Soroushian and Pouneh Rousta, my most constant and greatest friends since I started my Ph.D. in the United States. They provided me with a lot of kindness, support and encouragement over the years. Meeting them in the U.S. was a great happening. I would also like to thank two of my other friends in Reno, Nevada: Mahmoud Ghofrani and Saeed Jafazadeh. I appreciate their friendship and all the support they gave me during these years.

Last, but not least, I express my regards and thanks to my parents, my sister, Hoora, and her husband and my primary school friend, Ali, for their love and support during all the years of my education. Their belief and encouragement only made my achievements ever possible.

Thank you all.

Table of Contents

List of Figures

List of Tables

Chapter I: Introduction

1.1. Motivation

Electric power is essential to new modern societies. Economic prosperity, national security, and public health and safety will be jeopardized without it. The rapid growth of electricity demand over the last several decades and the advent of renewable energy-based power generations have resulted in a large increase of complex transmission and distribution lines in operation. The electric power grid is a vital component of the U.S. critical infrastructure and serves as an essential foundation for the nation. Electric power is transmitted and distributed to millions of people in homes, schools, offices, and factories across the United States through the electric power grid. Thus, investment in a modernized electric grid called 'smart power grid' has been an important issue in the 21st century. Smart power grid is more reliable, efficient, secure, and resilient to the external and internal causes of power outages, and aims at improving service for the millions of customers who rely on the grid for reliable power.

Faults in power transmission and distribution lines are happening as the result of storms, lightning, snow, freezing rain, insulation breakdown and short circuits by birds and other external objects [1]. Moreover, the aging nature of the U.S. electric grid, which was mostly constructed over a period of more than one hundred years, has caused more faults occurring and made customers more susceptible to outages caused by faults. In many fault cases, mechanical damages to the line equipment need to be repaired before restoring the line into service. Thus, accurate and fast detection and location of faults along power transmission and distribution lines are vital to decrease operation costs, to improve power system reliability, and to quickly restore the services for minimum economic losses.

Faults in transmission and distribution lines are either temporary or permanent. Fault locators in power grids provide estimates for both permanent and temporary faults. Temporary faults, the most dominant faults on overhead lines, are self-cleared [1]. Thus, the power supply is not permanently interrupted. However, they usually cause minor damages to the line equipment that are not easily visible to the maintenance crew during the periodic inspection. Fault locators help

identifying these locations for early repairs to prevent recurrence and consequent major damages to the line equipment [1]. If the fault is permanent, the identified faulty sections or equipment are disconnected permanently by the related protective relays and the faulty equipment or section is needed to be cleared by the maintenance crew. In the cases of a disconnected transmission line or a damaged transmission tower, repairs and/or equipment replacement might be needed before the transmission line is restored into service. Thus, it is important that the location of a fault is either known or can be estimated with reasonably high accuracy. This decreases the cost and time for the inspection and repair, as well as to provide a better service due to faster power supply restoration.

In modern societies and with the introduction of 'smart power grid', customers are more sensitive to the power outages. There are also more complex power transmission configurations to integrate renewable energy-based power generation at remote locations. Therefore, more efficient and accurate methods of fault location along these complex configurations are required, which target improving power supply restoration process, reducing the overall power outages time and costs, and enhancing customer satisfaction. Proliferation of advanced measurement technologies such as optic current and voltage transducers (CTs and VTs) can provide a venue for the implementation of more accurate fault location methods. Optic CTs and VTs are capable of capturing high-frequency transients in high- and extra-high-voltage power systems. These modern technologies offer the advantages of high accuracy, optical isolation, and wide range of frequency response [2]-[6]. Thus, the realization of precise fault location method using optical measurements with high sampling frequency (e.g. 200 kHz) becomes a reality with the proliferation of such modern technologies.

This dissertation aims at developing intelligent fault location methods along complex power transmission lines by using transient voltages and currents. The proposed traveling wave-based methods approaches utilize discrete wavelet transform (DWT) and support vector machine (SVM) where the main system conditions are taken into account through the learning step of SVM classifiers.

The contributions of this dissertation are introduced in the following section.

1.2. Contributions

The main contributions of this research work are itemized and briefly summarized below under three different subjects. The proposed methods and the relevant discussions are detailed further in the dissertation.

1.2.1. Fault Classification and Location for Three-Terminal Transmission Lines

A traveling wave-based method for fault classification and location for three-terminal power transmission systems is proposed. In the proposed method, DWT is utilized to extract transient information from the unsynchronized voltages measured only at two terminals. SVM classifiers are then used to classify the fault type and faulty line/half in the transmission networks. The first contribution of the proposed method is that it utilizes normalized wavelet voltage energies from only two terminals. Thus, the total cost of implementation is decreased by avoiding installation cost of optic voltage transducer and the required communication devices at the third terminal. The second contribution of the proposed method is the elimination of using time delay between the aerial mode and the ground mode traveling wave's arrival times for faulty half identification used in existing traveling wave–based fault location methods. Instead, the proposed method uses SVM for faulty half identification. This overcomes the challenging task of capturing the delay in the aerial mode and the ground mode traveling wave's arrival time as the wave velocities in these two modes are close to each other. The third contribution of the proposed method is that the SVM classifiers employ 8-dimensional input, which is significantly less than the dimension of the inputs used in the existing methods. Bewley diagrams are observed for the traveling wave patterns and the wavelet coefficients of the aerial mode voltage are used to locate the fault.

1.2.2. Fault Location for Hybrid HVAC Transmission Lines

A single-ended traveling wave-based fault location method for a hybrid high voltage alternative current (HVAC) transmission lines, an overhead line combined with an underground cable, is proposed. DWT is used to extract transient information from the measured voltages at the sending-end of the overhead line. SVM classifiers are utilized to identify the faulty section and faulty half by using the transient current and wavelet energies of voltages. The first contribution of the proposed method is that it utilizes a binary SVM classifier instead of using the time delay between arrival times of traveling waves in the aerial mode and the ground mode.

The second contribution of the proposed method is that the SVM classifiers employ 8-dimensional input, which is significantly less than the dimension of the inputs used in the existing methods. Bewley diagrams are observed for the traveling wave patterns and the wavelet coefficients of the aerial mode voltage are used to locate the fault.

1.2.3. Fault Location for Segmented HVDC Transmission Lines

A single-ended traveling wave-based fault location method for segmented high voltage direct current (HVDC) transmission lines, an overhead line combined with an underground cable, is proposed. DC transient voltage and current signals at the sending-end of the overhead line are assumed to be available. DWT is then applied to the DC voltage and current signals. The wavelet energies of voltage and current transients over 16 ms (i.e. 1-cyle in 60-Hz frequency) are calculated and then normalized. The normalized energies are used as the input to a binary SVM classifier for faulty section identification (i.e. underground cable or overhead line). The first contribution of the proposed method is that it requires measurement at only one terminal. The second contribution of the proposed method is that the SVM classifiers employ 2-dimensional input, which is less than the dimension of the inputs used in the existing methods. Once the faulty section is identified, the faulty half is determined by comparing polarity of the first two current traveling waves. Bewley diagrams are finally observed for the traveling wave pattern and the squared wavelet coefficients of DC voltage are used to locate the fault.

1.3. Chapter Organization

Chapter II gives a background on power system protection. Fundamentals of power system relaying are reviewed as well as the power system relaying for transmission lines. A general review of distance protection is briefly explained in this chapter.

In Chapter III, a general review of transmission line in steady-state and transient models are given first. Then, a review of existing power frequency-based fault location methods are given followed by a detailed description of traveling wave theory and traveling wave-based fault location methods. Artificial Intelligence based methods are briefly reviewed at the end of this chapter.

Chapter IV gives a review of wavelet transformation (WT) and fundamentals of support vector machines (SVM) and their applications in power systems are briefly reviewed.

Chapter V presents a traveling wave-based method for fault classification and location for three-terminal power transmission systems.

Chapter VI presents a single-ended traveling wave-based fault location method for a hybrid HVAC transmission line, i.e., an overhead line combined with an underground cable.

Chapter VII presents a single-ended traveling wave-based fault location method for segmented HVDC transmission lines, i.e., an overhead line combined with an underground cable.

The conclusions and the summaries of this dissertation are given in Chapter VIII.

Chapter II: Power System Protection

2.1. Introduction

Electric energy is one of the fundamental requirements of modern societies. Electric power is available to customers instantly, at certain voltage and frequency levels, and exactly in the amount that is needed. This remarkable performance is achieved through careful planning, design, installation and operation of power system, which is a very complex network of generators, transformers, transmission and distribution lines [7]. Disturbances and abnormal conditions occur in power grids due to load changes, faults created by natural causes and sometimes as a result of equipment or operator failure. Power system protection task is to design equipment (called 'relays' or 'protective relays') that detects abnormal power system conditions, and initiates corrective action as quickly as possible in order to return the power system to its normal state [7].

This chapter presents background relevant to power system protection and is organized into three sections. The first section reviews the concept of protective relaying in power system. The next section focuses on protective relaying of transmission lines. The most common relaying principle, distance protection, is reviewed in the third section.

2.2. Fundamentals of Power System Relaying

A power system is composed of a grid with power generators, loads, transmission and distribution lines, power transformers, circuit breakers, and other equipment, which are interconnected to provide electric power for customers. Fig. 1 shows an example of a simple 5-bus power system. The generations and loads are connected in the power grid through transmission lines. Power transfer capability, system stability, and voltage and frequency sustainability can be endangered with loss of even one critical transmission line. Circuit breakers are devices used to connect power system components and to carry transmission line currents under normal operating conditions, while interrupting the currents under specified abnormal operating conditions. They are located at both ends of a transmission line and by interrupting the current, they isolate the faulty equipment from the system [8].

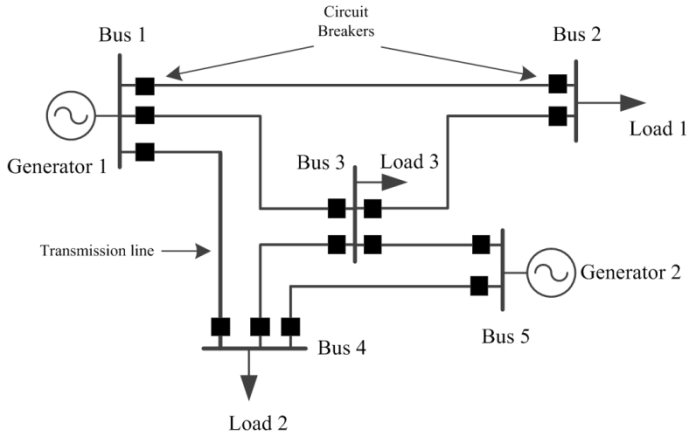

Figure 1. A 5-bus power system with two sources and three loads [7]

Transmission line faults occur randomly and they are typically an outcome of storms, lightning, snow, freezing rain, insulation breakdown, short circuits by birds or other external objects. The purpose of protective relaying is to minimize the impact of faults on the power system by preserving service availability and minimizing equipment damage [7]. Since the damage caused by a fault is mainly proportional to its duration, the protection system is required to operate as quickly as possible. The speed of response is an essential element of protective relaying systems. Response times, in the order of a few milliseconds are often required. Thus, human intervention in the protection system operation is not possible. The response must be automatic, quick and should cause a minimum amount of power system interruption. The essential task of power system protection is to open and close circuit breakers, thus changing the topology of the power system to isolate the fault and the faulty equipment from the power system.

2.3. Protective Relaying for Transmission Lines

Protective relays are intelligent devices located at both ends of each transmission line, nearby power system buses (i.e. substations) or other connection points [7], [8]. They quickly operate to protect the power system equipment once operating limits are violated due to a fault occurrence or other abnormal conditions. The protection system in power systems includes many components to detecte and to remove the faults. As shown in Figure 2, the major components of a protection system are the instrument transformers, relays, batteries and circuit breakers.

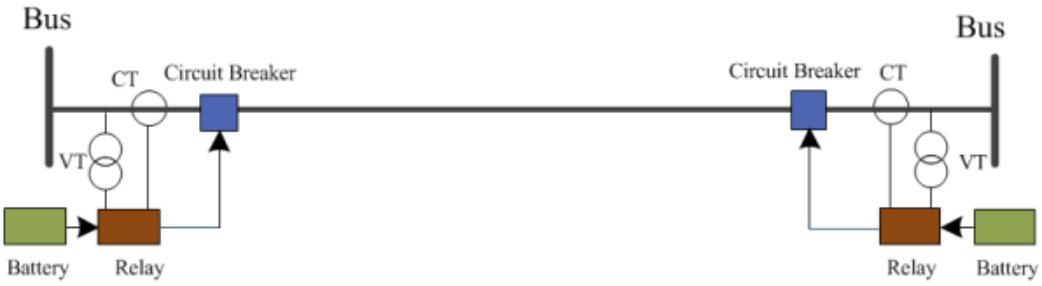

Figure 2. Components of protective relaying for a transmission line [8]

Instrument transformers, i.e. the current and voltage transformers (CT and VT), constitute a major component of a protection system. They obtain current and voltage measurements and reduce the transmission level signals into lower level signals appropriate to be fed into the relay. Relays are the logic elements which recognize the faults in the particular area of a power grid based on the measured three-phase voltage and current signals. The relay needs to reliably conclude whether and which type of a fault occurs and initiate the tripping and closing operations of the circuit breaker [8]. As the protection system is primarily responsible to remove a fault, it should be able to trip a circuit breaker during a fault, even though the AC voltage in the substation may not be of sufficient magnitude. Thus, the battery stations in the substation provide required power to operate circuit breakers, as well as to continuously run the protective relays.

A relay protects its assigned transmission line as the primary task. It also operates as the backup protection for other relays located at neighboring lines, beyond the remote end of its corresponding line. The relay responsibility for protection of a segment of the power system is defined by a concept of 'protection zone' [8]. A protection zone is a pre-defined setting which is expressed as the percentage of the transmission line length, measured from the relay location. Once a fault is detected inside the zone of a relay, the protection system sends the tripping signal to the circuit breakers to isolate the faulty section of the power system defined by the zone borders. In order to ensure back-up protection for all portions of power grids, overlapping zones of protection is considered in the protective relays coordination.

Figure 3 shows a small segment of a power system. It consists of three transmission lines connecting Buses A, B and C. The protection zones of the relay located at bus A (i.e. R_{ab}) are enclosed by dashed lines.

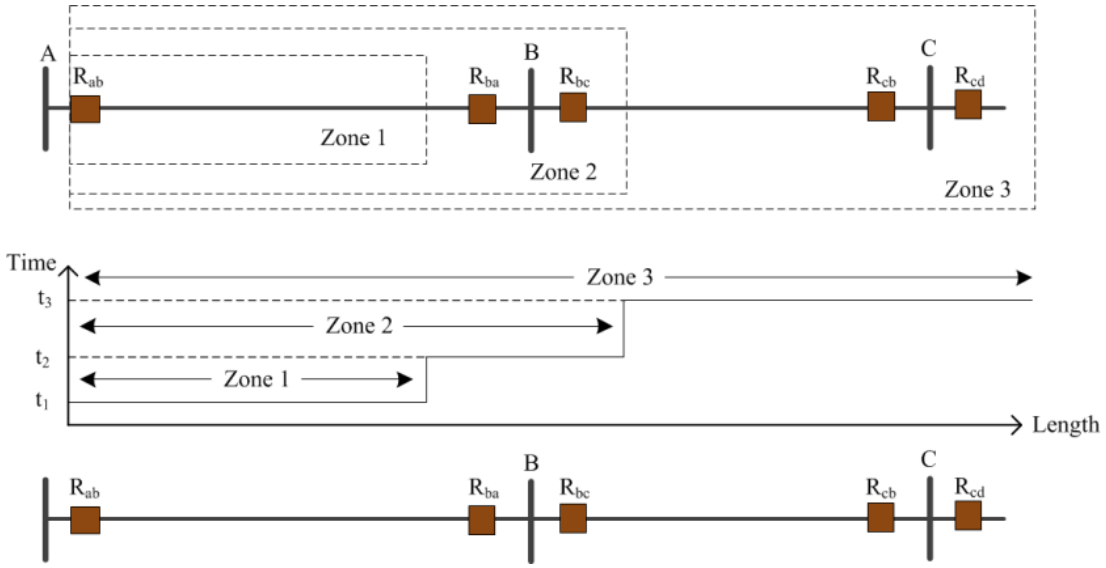

Figure 3. Protective relaying zones of operation for a transmission line [8]

The relay located at bus A has three zones of protection. Zone 1 is the primary zone of protection, while zones 2 and 3 are the backup protections for relays R_{bc} and R_{cd} respectively in case they misoperate for the faults in their primary zone of operation. Coordination of relays are carried out by calculation of settings for each relay to achieve selectivity for faults at different locations. The zone 1 setting of relays trips with no intentional delay, except for the relay and circuit breaker operating time t_1. The zone 1 is set to underreach the remote end of the line, and usually covers around 85-90% of the line length [8]. As the relay is not capable of precisely determining fault location, entire length of the transmission line is not covered by zone 1 of a relay. If the zone 1 covers the entire line length, instant undesired operation may happen for the faults which are located beyond the remote terminal. Therefore, the relay has another zone of operation, which intentionally overreaches beyond the remote terminal of the transmission line. The zone 2 of the relay covers the remote end of the transmission line which is not covered by the zone 1. The zone 2 of a relay is coordinated with zone 1 of the relay at the adjacent line by considering a time delay, t_2 which is usually in the order of 0.3 sec. The zone 2 setting overreaches the remote end of the line and typically is set to 120-150 % of the line length [7], [8]. It needs to be mentioned that zone 2 of relay R_{ab} must not overreach the zone 1 of relay R_{bc},

otherwise some faults may exist simultaneously in the second zones of R_{ab} and R_{bc}, and may lead to unnecessary tripping of both line.

The zone 3 setting provides back up protection for neighboring line and usually extends to 120–180% of the next line length. The zone 3 coordinates in time and distance with the second zone of the adjacent line, and usually operates with the time delay t_3 which is in the order of 1 sec [7].

It needs to be mentioned that it is not always possible to have acceptable settings for the two overreaching zones of relays. For instance, if the length of a downstream adjacent line is less than 20% of the line being protected, its zone 2 certainly overreaches the zone 1 of the shorter line. Similarly, the zone 3 of the first line may overreach the zone 2 of the next line. The general rules for setting the reach of zones mentioned above are considered to be approximate, and need be adjusted to meet each specific power system configuration [7].

Misoperation in protection systems is often a contributing cause to the cascading failures in power system blackouts. The most problematic failure among possible failures of the protection systems, are the 'hidden failures' (HF). HFs in protection systems are defined as "a permanent defect that will cause a relay or a relay system to incorrectly and inappropriately remove a circuit element(s) as a direct consequence of another switching event" [9]. HFs in protection systems have become important in recent years, as power grids are more stressed due to an increase in use of transmission lines capacities. They weaken the security of the protection systems and lead to unnecessary outages.

2.4. Distance Relaying

Distance relays are the most common relays used to protect transmission lines. They respond to the apparent impedance between the relay location and the fault location. It sends the tripping signal when the apparent impedance seen by the relay decreases bellow a pre-set value [8]. Relay settings are determined through extensive short circuit studies using the power system model and simulations of the worst-case fault scenarios. Figure 4 shows a simplified single-phase electrical circuit, with voltage source, load, and pre-fault transmission line. It is noted that shunt

susceptances of the line is neglected. The apparent impedance seen by the relay before the fault is calculated by dividing the measured voltage and current phasors as [8]

$$Z_{line} = R_{line} + jX_{line} \qquad R_{line} \ll X_{line} \tag{2.1}$$

$$Z_{load} = R_{load} + jX_{load} \qquad R_{load} > X_{load} \tag{2.2}$$

$$Z_{pre-fault} = \frac{V_{pre-fault}}{I_{pre-fault}} = Z_{line} + Z_{load} \tag{2.3}$$

It is noted that, condition in (2.1) is due to highly inductive impedance of a transmission line, while condition in (2.2) is due to mostly resistive load characteristic.

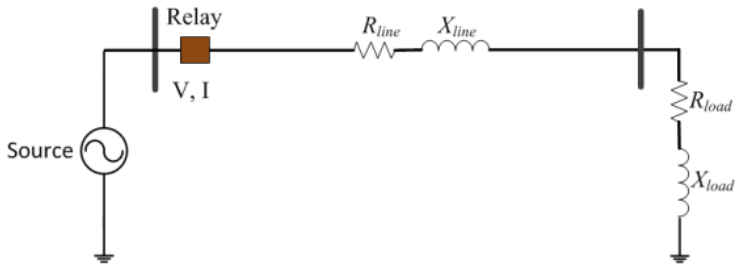

Figure 4. Equivalent circuit of a transmission line during pre-fault condition [8]

Figure 5 shows the faulty transmission line and the apparent impedance seen by the relay during fault is calculated as [8]

$$Z_{fault} = mZ_{line} + \big((1-m)Z_{line} + Z_{load}\big)||R_{fault} \tag{2.4}$$

$$Z_{fault} = mZ_{line} + \frac{\big((1-m)Z_{line} + Z_{load}\big)R_{fault}}{(1-m)Z_{line} + Z_{load} + R_{fault}} \tag{2.5}$$

$$Z_{fault} \simeq mZ_{line} + R_{fault} \text{ when } R_{fault} \ll R_{load} \tag{2.6}$$

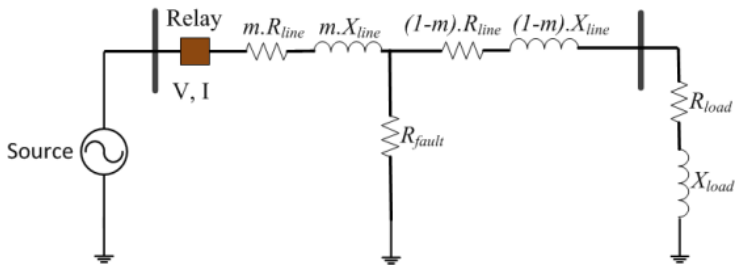

Figure 5. Equivalent circuit of a transmission line during fault condition [8]

The impedance measured by a relay is graphically represented in the complex, resistance-reactance or R–X diagram shown in Figure 6. The origin of the plane denotes the relay location and the beginning of the protected line. It needs to be noted that for phase-to-phase and phase-to-ground faults with fault resistance close to zero, the fault impedance vector (Z_{fault}) lies on the straight line representing the transmission line characteristic impedance

By comparing (2.3) and (2.5), it is noted that the impedance seen by the relay during normal load conditions is significantly higher than the impedance during the fault. The apparent impedance seen by the relay varies with fault impedance, as well as impedance of equivalent sources and loads. It also depends on the type and location of the fault in the transmission line. Thus, apparent impedance detection is not as simple as the single-phase analysis given for simplified network and transmission line. The interconnection of complex transmission line configurations imposes a complex set of relay settings [8].

The impedance seen by the distance relay is compared with its pre-defined settings. Settings are defined as the operating characteristics in the complex R–X plane that enclose all faults with varying resistance along the protected section of the transmission systems. A distance relay operates whenever the estimated impedance remains within the particular zone of protection for the specified time interval.

There are ten different types of possible faults on a three-phase power system: a three-phase fault, three phase-to-phase faults, three different phase-to-ground faults and three combinations of double-phase-to-ground faults. The equations describing the relationship between voltages and currents at the relay location are different for each fault type. Therefore, different pairs of voltage and current inputs are needed to measure the distance to the fault for each specific fault

type. However, it is a fundamental principle of distance relaying that the appropriate relay measures the positive sequence impedance to the fault regardless of the fault type [8].

Distance relays are classified according to the shape of their zones of operation. Traditionally, all zone shapes have been circular, because an electromechanical relay produces a circular boundary for the zones of operation. However, more complex zone shapes are achieved with modern solid-state and computer relays [7].

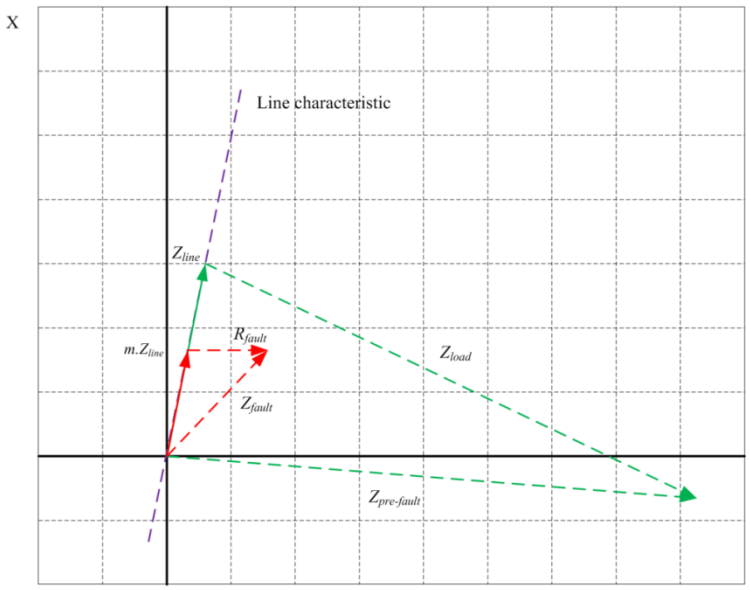

Figure 6. R–X diagram of the apparent impedance seen by the relay during pre-fault & fault conditions [8]

Four general relay types are recognized according to the shapes of their operating zones as impedance relays, admittance or mho relays, reactance relays, and quadrilateral relays [7]. These four relay characteristic shapes are illustrated in Figure 7. The impedance relay has a circular shape centered at the origin of the R–X diagram. The admittance (or mho) relay has a circular shape which passes through the origin. The reactance relay has a zone boundary defined by a line parallel to the R axis. The zone extends to infinity in three directions as shown in Fig. 7. The quadrilateral characteristic, as the name implies, is defined by four straight lines. This last characteristic is only available in solid-state or computer relays. More complex shapes are obtained by using one or more of the above relay types, in a logical combination to provide a complex tripping zone boundary [7].

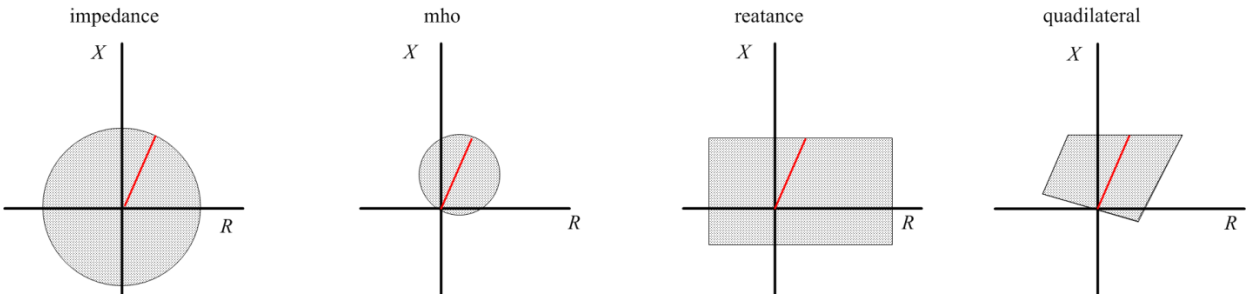

Figure 7. Four types of distance relay characteristics [7]

2.5. Summary

In this chapter, the backgrounds of power system protection systems are reviewed. The concept of protective relaying in power system is first reviewed. Then, concepts of protective relaying in transmission lines and their zones of operation are reviewed. The most common relaying principle, distance protection and the relevant formulations of distance protection are reviewed at the end of this chapter. The next chapter presents the backgrounds on fault location in power transmission lines.

Chapter III: Fault Location in Power Transmission Lines

3.1. Introduction

Faults in transmission and distribution lines occur because of storms, lightning, snow, freezing rain, insulation breakdown and short circuits by birds and other external objects. In many fault events, mechanical damages to the line equipment need to be repaired before restoring the line into service. The rapid growth of electricity demand over the last several decades and the interconnection of renewable energy-based power generation have resulted in a large increase of existing transmission and distribution lines usage and installation of new complex ones. Thus, accurate and fast fault detection and location along power transmission and distribution lines are vital to decrease operation costs, to improve power system reliability and to quickly restore the services for minimum economic losses.

The fault location methods for power transmission lines are generally classified under three main categories [1]:

1. Power frequency-based methods,
2. Traveling wave-based methods, and
3. Artificial Intelligence-based methods.

The power frequency-based and some artificial intelligence-based fault location methods use post-fault steady-state voltage and current measurements, while transient voltages and currents are used by traveling wave-based and some other artificial intelligence-based fault location methods. Post-fault steady-state voltages and currents in power transmission systems are analyzed using steady-state transmission line models. However, the analysis of transient phenomena is performed using transient (distributed) models of transmission lines. Thus, in the following sections, a general review of transmission line models for steady-state and transient analyses are given. Then, a review of existing power frequency-based fault location methods are given followed by a detailed description of traveling wave theory and traveling wave-based fault

location methods. Artificial Intelligence-based methods are briefly reviewed at the end of this chapter.

3.2. A Review of Transmission Line Models

Transmission lines are modeled according to a particular application. For short-circuit and power flow studies, steady-state models of transmission lines are used. Short and medium line models use lumped transmission line parameters for short (<50 *mi*) and medium line (>50 *mi* & <150 *mi*) length. However the short and medium line models will not provide accurate results when analyzing long lines (>150 *mi*). The long line model use distributed line parameters.

For time-domain transient analysis, the steady-state line models are not suitable. The cascaded connection of π circuit was first introduced for time-domain transient analysis. However it soon became apparent that the transmission line models which are derived using the traveling wave equations are more accurate for time-domain transient analysis than cascaded connection of π circuits. Distributed line models were developed to improve the time-domain transient analysis using frequency-independent impedances and lumped resistances to approximate the losses. However, transmission line parameters such as series resistance, *R* and series inductance, *L* are functions of frequency. Therefore, distributed line model with constant parameters may not give accurate results for time-domain transient analysis especially for the types of transients containing considerable zero-sequence voltages and currents (e.g. grounded faults) [11].

In overhead lines, the positive sequence inductance and resistance are constant. However, the later one starts to increase in higher frequencies where the conductors are affected by skin effect. On the other hand, the zero sequence inductance and resistance vary as frequency increases because of skin effects and the earth return [11]. The positive and zero sequence resistances and inductances of a three-phase overhead transmission line are shown in Figure 8. They are shown as a function of the logarithm of the frequency for the range of 1 to 10^8 Hz. The transmission line tower configuration data is given in Appendix A.

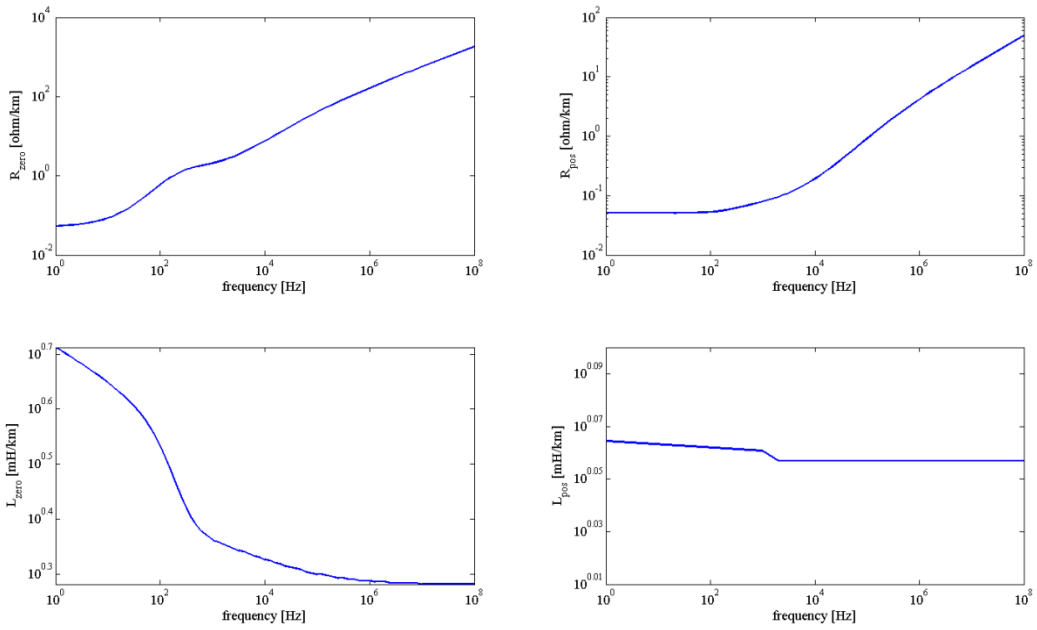

Figure 8. Positive and zero sequence resistance and inductance of a three-phase overhead line created in EMTP-RV [11]

Therefore, the frequency-dependent line model is used in time-domain transient analysis and in some other steady-state applications such as harmonic analysis.

Steady-state and transient model of transmission line are reviewed followed by Lattice diagram and modal transformation concepts in the following sections.

3.2.1. Steady-State Model of Transmission Lines

Three models of transmission lines under normal steady-state operating conditions are briefly explained in this section. A single-phase transmission line model is developed in this section which can easily be replaced by matrix model instead of scalar model in the case of three phase lines.

A) Short line model

The short line model, shown in Figure 9 is generally used for transmission lines with less than 50 mile length. The model uses lumped series resistance and inductance. Shunt admittance ($y = G+j\omega C$) is neglected.

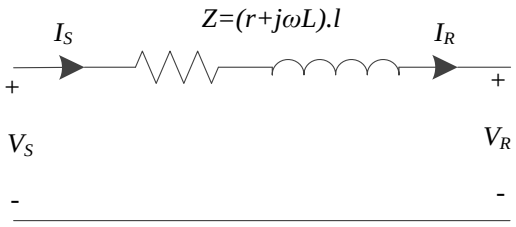

Figure 9. Short line model

The sending end voltage and current of the short line are obtained by writing Kirchhoff's voltage law (KVL) and Kirchhoff's current law (KCL) equations as

$$V_s = V_R + ZI_R \tag{3.1}$$

$$I_S = I_R \tag{3.2}$$

The voltage and current equations are written in the matrix form as

$$\begin{bmatrix} V_S \\ I_S \end{bmatrix} = \begin{bmatrix} A & B \\ C & D \end{bmatrix} \begin{bmatrix} V_R \\ I_R \end{bmatrix}, \tag{3.3}$$

where, the ABCD parameters for a short line model are

$$A = D = 1\ pu \tag{3.4}$$

$$B = Z\ \Omega \tag{3.5}$$

$$C = 0 \tag{3.6}$$

B) Medium line model

In the medium line model ranging from 50 to 150 miles, the shunt capacitance of the line is lumped and half of it is located at each end of the line. This model is also known as π model. The one-line diagram of the π model is shown in Figure 10.

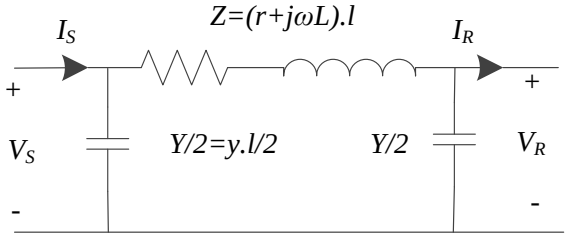

Figure 10. Medium line model

The current through the series impedance is $I_R + \frac{YV_R}{2}$ and the sending ending voltage is $V_S = V_R + Z(I_R + \frac{YV_R}{2})$. Using KCL, the current at the sending end of the line is $I_S = I_R + \frac{YV_R}{2} + \frac{YV_S}{2}$. The ABCD parameters of the medium line model are expressed as [10]

$$A = D = 1 + \frac{ZY}{2}\ pu \tag{3.7}$$

$$B = Z\ \Omega \tag{3.8}$$

$$C = Y\left(1 + \frac{ZY}{4}\right)S \tag{3.9}$$

where Z is the total series impedance of the line [Ω] and Y is the total shunt admittance of the line [S].

C) Long line model

The line parameters, *R*, *L* and *C* are calculated as per-unit length values having units of *Ω/mile*, *H/mile* and *F/mile*. They are not lumped rather than uniformly distributed along the length of the line. In order to derive the voltage and current equations for this exact π model (equivalent π model), an infinitesimal Δx ($\Delta x \to 0$) element of the transmission line given in Figure 11 is considered.

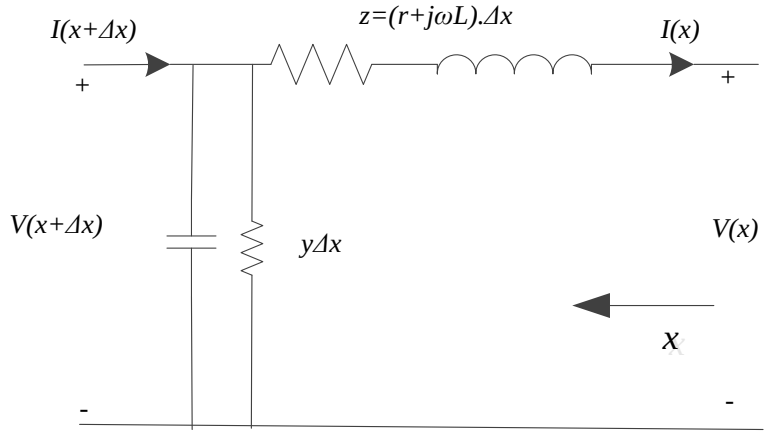

Figure 11. Transmission line section of length Δx

Voltage and current equations of the infinitesimal element of the transmission line are obtained by using KVL and KCL as

$$\frac{dV(x)}{dx} = zI(x) \tag{3.10}$$

$$\frac{dI(x)}{dx} = yV(x) \tag{3.11}$$

where all line parameters are given in per-unit length and shunt admittance $y=G+j\omega C$ is assumed to be lossless (G=0).

Propagation equation is obtained by combining equations (3.10) and (3.11), as

$$\frac{dV^2(x)}{dx^2} = zyV(x) \tag{3.12}$$

The voltage along the transmission line is obtained by solving the above equation as

$$V(x) = A_1 e^{\gamma x} + A_2 e^{-\gamma x} \tag{3.13}$$

The current equation along the transmission line is obtained as

$$I(x) = \frac{A_1 e^{\gamma x} - A_2 e^{-\gamma x}}{Z_c} \tag{3.14}$$

where, $\gamma = \sqrt{zy}$ [mile^{-1}] is the propagation constant and $Z_c = \sqrt{\frac{z}{y}}$ [Ω] is the characteristic impedance.

By solving equations (3.13) and (3.14) using boundary conditions at x=0 (i.e. $V(0) = V_R$ and $I(0) = I_R$), A_1 and A_2 are obtained as

$$A_1 = \frac{V_R + Z_c I_R}{2} \tag{3.15}$$

$$A_1 = \frac{V_R - Z_c I_R}{2} \tag{3.16}$$

The voltage and current equations along the line are then expressed in terms of receiving end voltage and current in the form of hyperbolic functions as

$$V(x) = \cosh(\gamma x)\, V_R + Z_c \sinh(\gamma x)\, I_R \tag{3.17}$$

$$I(x) = \frac{1}{Z_c}\sinh(\gamma x)\, V_R + \cosh(\gamma x)\, I_R \tag{3.18}$$

The ABCD parameters at the sending end of the line $x=l$ are given as

$$A = D = \cosh(\gamma l)\ pu \tag{3.19}$$

$$B = Z_c \sinh(\gamma l)\ \Omega \tag{3.20}$$

$$C = \frac{1}{Z_c}\sinh(\gamma l)\, S \tag{3.21}$$

The single-line diagram of equivalent π model is shown in Figure 12.

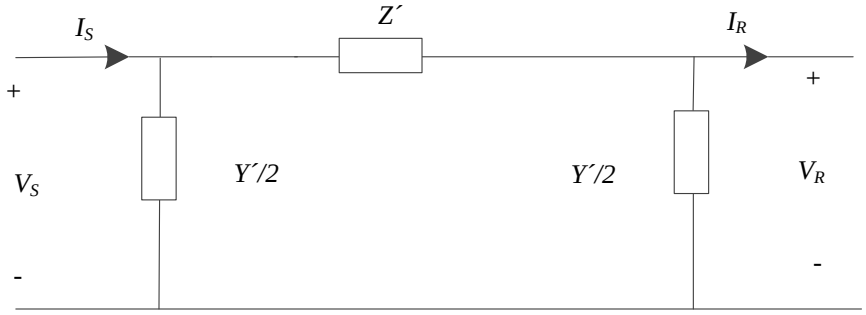

Figure 12. Equivalent π model of long line

The ABCD parameters of the equivalent π model are as

$$A = D = 1 + \frac{Y'Z'}{2}\ pu \tag{3.22}$$

$$B = Z'\ \Omega \tag{3.23}$$

$$C = Y'\left(1 + \frac{Y'Z'}{2}\right) S \tag{3.24}$$

where $Z' = Z_c \sinh(\gamma l)$ and $Y' = \frac{\tanh\left(\frac{\gamma l}{2}\right)}{Z_c}$.

3.2.2. Traveling Wave Theory and Transient Model of a Transmission Line

As it is mentioned in the previous section, parameters of transmission lines, *R*, *L* and *C* are frequency-independent in steady-state operation and short-circuit analysis. However, for some specific steady-state and time-domain power system transient analysis, use of these constant parameters are not appropriate. Detailed frequency dependent line models are used for the following types of analysis [10]:

- Steady-state problems at higher frequencies such as harmonic analysis,
- Time-domain transient analysis such as switching, lightning surge or fault studies.

A) Traveling wave on ideal lossless line

Voltage and current equations along transmission lines, introduced in equations (3.10) to (3.11), are considered for time-domain analysis. The infinitesimal Δx element in Figure 11 is assumed to be lossless where series resistance, R, and shunt conductance, G, are ignored. Transmission line voltage and current equations in time-domain are given as [10]

$$\frac{dV(x,t)}{dx} = -L\frac{dI(x,t)}{dt} \tag{3.25}$$

$$\frac{dI(x,t)}{dx} = -C\frac{dV(x,t)}{dt} \tag{3.26}$$

where the direction of increasing x is selected from the sending end (x=0) toward the receiving end (x=l).

The voltage and current equations in frequency domain is obtained by using Laplace transform as

$$\frac{dV(x,s)}{dx} = -sLI(x,s) \tag{3.27}$$

$$\frac{dI(x,s)}{dx} = -sCV(x,s) \tag{3.28}$$

where $V(x,s)$ and $I(x,s)$ are the Laplace transform of $V(x,t)$ and $I(x,t)$, respectively.

Differentiating equations (3.27) and (3.28) with respect to x and substituting (3.26) and (3.25) in them respectively, is resulted as

$$\frac{dV^2(x,s)}{dx^2} = -s^2LCV(x,s) \tag{3.29}$$

$$\frac{dI^2(x,s)}{dx^2} = -s^2LCI(x,s) \tag{3.30}$$

The solutions of the above second-order differential equations are

$$V(x,s) = V^+(s)e^{-sx/v} + V^-(s)e^{+sx/v} \tag{3.31}$$

$$I(x,s) = I^{+}(s)e^{-sx/\upsilon} + I^{-}(s)e^{+sx/\upsilon} \tag{3.32}$$

where $\upsilon = \frac{1}{\sqrt{LC}}$ is the traveling wave velocity of the lossless line.

The voltage and current equations in time-domain are then obtained as follows

$$V(x,t) = v^{+}\left(t - \frac{x}{\upsilon}\right) + v^{-}\left(t + \frac{x}{\upsilon}\right) \tag{3.33}$$

$$I(x,t) = \frac{1}{Z_c}\left(v^{+}\left(t - \frac{x}{\upsilon}\right) - v^{-}\left(t + \frac{x}{\upsilon}\right)\right) \tag{3.34}$$

where v^{+} and v^{-} are the voltage traveling waves which travel in the positive and negative x direction respectively. Equation (3.34) is multiplied by Z_c and then added to or subtracted from equation (3.33), to obtain the following equations

$$V(x,t) + Z_c i(x,t) = 2v^{+}\left(t - \frac{x}{\upsilon}\right) \tag{3.35}$$

$$V(x,t) - Z_c i(x,t) = 2v^{-}\left(t + \frac{x}{\upsilon}\right) \tag{3.36}$$

It is noted from equation (3.35) that $v+Z_c i$ is constant if $t-x/v$ is constant. Thus, $v+Z_c i$ is constant to an observer which travels in the forward direction in the transmission line with the velocity v. If the traveling time, $\tau=l/v$ is the travel time from sending end to the receiving end of the line, the value of $v+Z_c i$ at time t-τ at the sending end is the same value at time t at the receiving end. Similarly, v-$Z_c i$ in equation (3.36) is constant if $t+ x/v$ is constant. v-$Z_c i$ is also constant to an observer which travels with the velocity v, in the backward direction. Therefore, the value of v -$Z_c i$ at time t-τ at the receiving end is the same value at time t at the sending end. The statements mentioned above can be expressed respectively as

$$V_s(t-\tau) + Z_c i_s(t-\tau) = V_R(t) + Z_c i_R(t) \tag{3.37}$$

$$V_R(t-\tau) - Z_c i_R(t-\tau) = V_s(t) - Z_c i_s(t) \tag{3.38}$$

If equations (3.37) and (3.38) are manipulated, the equations for terminal currents in terms of the equivalent current sources I_S and I_R are obtained as follows [12]

$$i_S(t) = I_S(t-\tau) + \frac{1}{Z_c}V_S(t) \tag{3.39}$$

$$i_R(t) = I_R(t-\tau) - \frac{1}{Z_c}V_R(t) \tag{3.40}$$

where $I_S(t-\tau)$ and $I_R(t-\tau)$ are the past history of the transmission line and expressed as

$$I_S(t-\tau) = i_R(t-\tau) - \frac{1}{Z_c}V_R(t-\tau) \tag{3.41}$$

$$I_R(t-\tau) = i_S(t-\tau) + \frac{1}{Z_c}V_S(t-\tau) \tag{3.42}$$

The discrete time equivalent circuit of a transmission line is shown in Figure 13.

In order to perform time-domain transient simulations, continuous-time circuit parameters, *L* and *C* are converted to discrete-time parameters [12]. A lumped inductance, *L* is expressed by parallel connection of a resistance $R_L=2L/\Delta t$ (Δt is the time step of the simulation) and a history term of current source [12]. The current through the lumped inductance is gives as

$$i(t) = \frac{V(t)}{2L/\Delta t} + I_L(t-\Delta t) \tag{3.43}$$

$$I_L(t-\Delta t) = i(t-\Delta t) + \frac{V(t-\Delta t)}{2L/\Delta t} \tag{3.44}$$

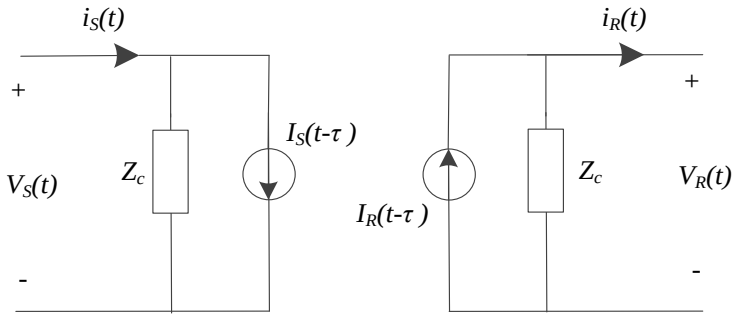

Figure 13. Discrete time circuit of a transmission line [10]

Discrete model of a lumped capacitance, *C* is also expressed by parallel connection of a resistance $R_C=\Delta t/2C$ and a history term of a current source [12]. The current through the lumped capacitance is given as

$$i(t) = \frac{V(t)}{\Delta t/2C} - I_C(t-\Delta t) \tag{3.45}$$

$$I_C(t-\Delta t) = i(t-\Delta t) + \frac{V(t-\Delta t)}{\Delta t/2C} \tag{3.46}$$

Discrete-time model of an ideal lossless transmission line is reviewed in this section. In the next sections, the loss is taken into account under two models. First, the lumped resistance model is given followed by the review of more accurate frequency dependent line model.

B) Lumped resistance line model (distributed line model)

The lumped resistance line model is also known as constant parameter (CP) model or distributed line model. The model is based on the ideal (lossless) line model as well as the lumped resistances at three places: *R/4* at both ends and *R/2* in the middle of the transmission line as shown in Figure 14. Thus, a lossy transmission line with line length "*l"* is simulated in ATP/EMTP, by creating two ideal transmission lines of equal length, *l/2* and the losses are modeled with constant resistances.

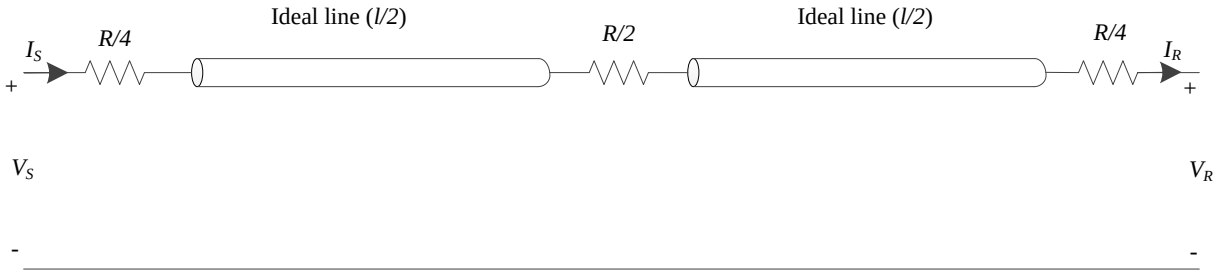

Figure 14. Lumped resistance line model [11]

The transient simulation results obtained from CP line models remain accurate as long as the total resistance of the line (i.e. $R=rl$) is considerably smaller than the characteristic impedance of the line (Z_c), i.e. $R<<Z_c$. In the next section, frequency dependent (FD) line model introduced by J. R. Marti is discussed [13]. All line parameters, *R*, *L*, are considered as functions of frequency which are distributed along the transmission line.

C) Frequency dependent line model

Since the transmission line parameters, R and L vary with frequency, the characteristic impedance (Z_c) and the propagation constant (γ) of the line also change at different frequencies [13],[14]. Thus, characteristic impedance $Z_c(\omega)$ and propagation function $A(\omega) = e^{-\gamma l}$ are approximated as functions of frequency. The FD model of transmission lines is developed by approximating the characteristic impedance as *RC* networks which is shown in Figure 15.

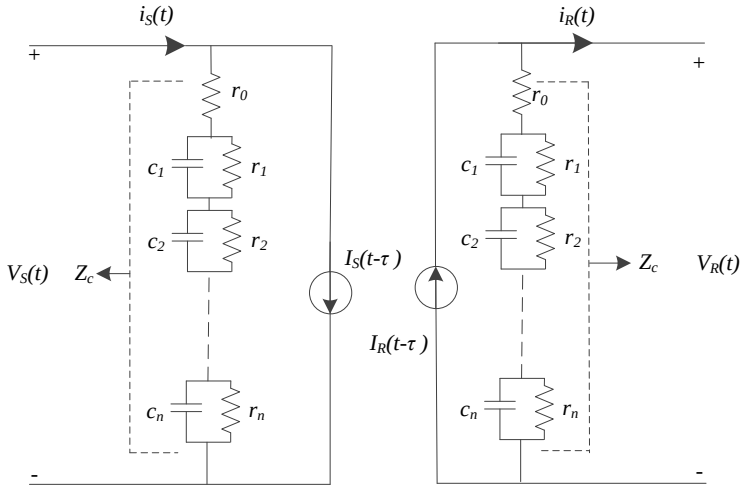

Figure 15. Frequency dependent (FD-J. Marti) transmission line model [11]

The characteristic impedance is approximated by a rational function as [11]

$$Z_c(S) = k\frac{(s+z_1)(s+z_2)\dots(s+z_n)}{(s+p_1)(s+p_2)\dots(s+p_n)} \tag{3.47}$$

where $s=j\omega$. All poles and zeros are real and negative and the number of poles is equal to the number of zeros. It is then expressed as

$$Z_c(S) = k_0 + \frac{k_1}{s+p_1} + \frac{k_2}{s+p_2} + \cdots + \frac{k_n}{s+p_n} \tag{3.48}$$

(3.49)

The expressed $Z_c(S)$ corresponds to the *RC* network in Figure 15 with the following values

$$r_0 = k_0 \tag{3.50}$$

$$r_i = \frac{k_i}{p_i} \text{ and } c_i = \frac{1}{k_i}, \quad for\ \ i = 1 \dots n \tag{3.51}$$

The rational function which approximates propagation function, $A(\omega)$, has also similar form rather than the number of zeros (n) is smaller than the number of poles (m). An exponential term, $e^{-j\omega\tau_{min}}$ is also included to take care of the fact that *a(t)* is zero up to time $\tau = \tau_{min}$ as

$$A(S) = e^{-s\tau_{min}} k \frac{(s+z_1)(s+z_2)\dots(s+z_n)}{(s+p_1)(s+p_2)\dots(s+p_m)} \tag{3.52}$$

With n<m, the above rational function is written as the following partial functions

$$A(S) = \frac{k_1}{s+p_1} + \frac{k_2}{s+p_2} + \cdots + \frac{k_m}{s+p_m} \tag{3.53}$$

The weighting function *a(t)* which is the inverse Laplace transform of *A(ω)* is used to calculate the history terms, $I_s(t-\tau)$ and $I_R(t-\tau)$.

In order to successfully create the FD model of a transmission line, rational function approximation for *A(ω)* and $Z_c(\omega)$ needs to be carried out precisely. The magnitudes of the functions are approximated using Bode's diagram. To illustrate the Bode's procedure, the magnitude of the positive sequence characteristic impedance of the transmission line is shown in Figure 16.

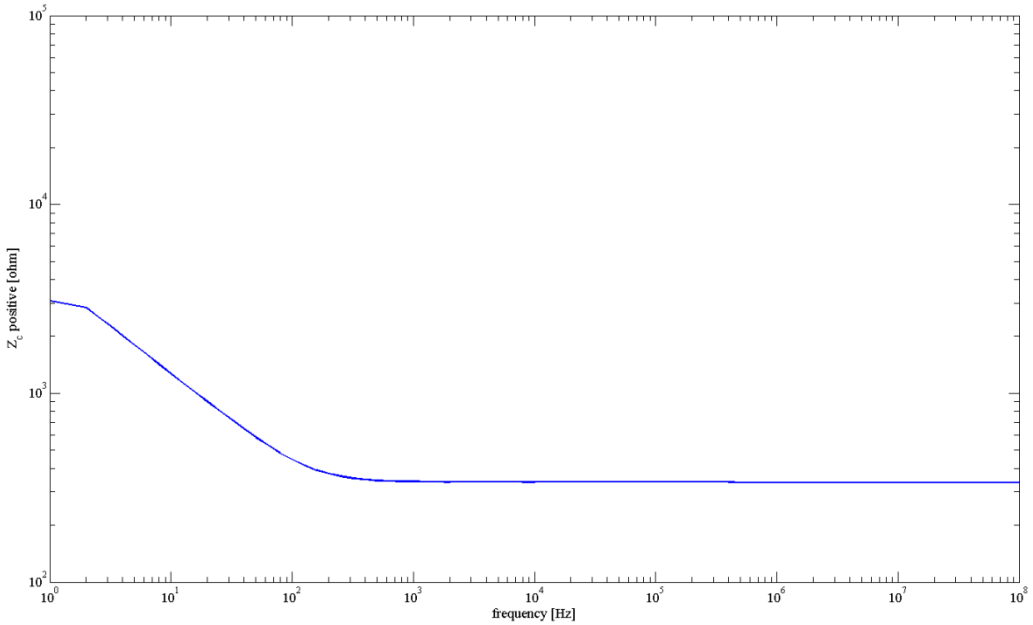

Figure 16. Positive sequence characteristic impedance magnitude of a three-phase overhead line created in EMTP-RV [11]

The basic principle of the procedure is to approximate the given curve by straight-line segments which are either horizontal or have a slope which is a multiple of 20 dB/decade. The poles and zeros of the rational function are defined at the points where the slopes change. By taking the logarithm of equation (3.47) and multiplying it by 20, the following expression is obtained [11]:

$$20\log z_c(s) = 20\log k + 20\log|s+z_1| + \cdots + 20\log|s+z_n| \\ -20\log|s+p_1| - \cdots - 20\log|s+p_n| \tag{3.54}$$

where $s=j\omega$ and each term in the above expression has a straight-line behavior with respect to ω. For instance, $20\log|j\omega+z_1|$ becomes $20\log z_1$ for $\omega<<z_1$ and $20\log\omega$ for $\omega>>z_1$ which is a straight-line with slope of 20 dB/decade. Each time a zero corner is added at $\omega=z_i$, the slope of the curve is increase by 20 dB and if a pole is added at $\omega=p_i$, it decreases by 20 dB. The number of zeros and poles are not known a-priory and the curve is approximated step by step. The curve is traced from DC to the highest frequency at which the characteristic impedance becomes constant [11].

D) Lattice diagram

Traveling waves initiate in power grids as a results of a switching action or a fault. The initiated waves travel in forward and backward directions along transmission lines and reflect or refract at discontinuities along their paths such as: fault points, line junctions, receiving or ending terminals. Traveling waves continue to reflect and refract at the discontinuities until their energy dissipates and steady-state conditions are reached in less than one-cycle (i.e. 16 *msec*). Traveling wave behavior is studied by using the Lattice diagram proposed by Bewley [15]. Figure 17 shows an example where a single-phase lossless line is considered for a fault at location *F*. The Lattice diagram shows multiple reflections and refractions initiated by the fault. τ is the travel time associated with the total length of the line.

The arrival times of the backward and forward traveling waves are indicated in Figure 17. If the fault is *x* miles away from bus A, the arrival time of the forward traveling wave at bus B is $t_1 = \frac{l-x}{v}$, and the arrival time of the backward traveling wave at bus A is $t_2 = \frac{x}{v}$, where *l* is the total length of the line and ν is the traveling wave velocity. This information is utilized to locate the fault.

In three-phase transmission lines, there are three modes of propagation. Therefore, the traveling wave calculations have to be done in the modal domain for each mode separately. The modal transformation for three-phase transmission lines is reviewed in the next section.

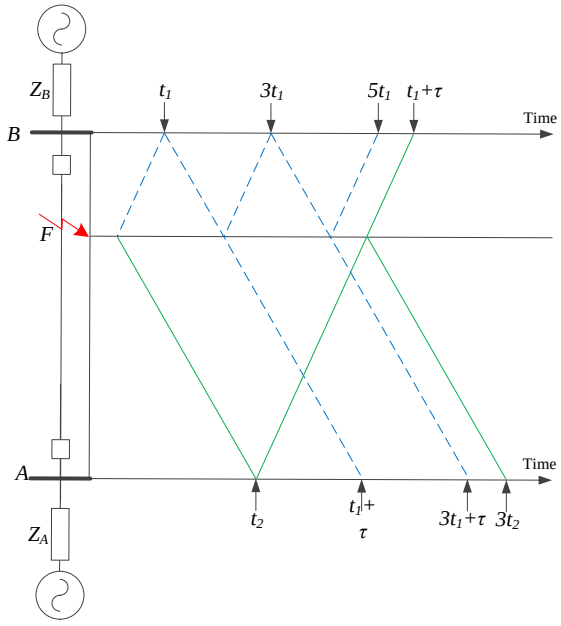

Figure 17. Lattice diagram for a fault at point F [12]

E) Modal transformation for three-phase transmission lines

AC power transmission lines are three-phase systems where each phase is composed of one or more conductors that are bundled to decrease the skin effects. There are induced voltages on each phase as the result of mutual electromagnetic interaction with other phases. These induced voltages are represented by mutually coupled impedances between the conductors. In order to make the solution of a three-phase power transmission line simpler, the three coupled transmission line equations are decoupled into three independent equations using a transformation called "Modal transformation" [12]. It was initially developed by Wedepohl to reduce the three-phase power transmission problem to three single-phase problems [16]. As there are three independent voltage and current equations corresponding to three-phase power transmission lines, each equation reveals its own mode of propagation, meaning each having its own characteristic impedance, Z_c and time delay, τ. Thus, traveling wave velocity in each mode is different from other modes, if the corresponding time delay is different.

Clarke's transformation is one of the most commonly used transformations used to decouple three-phase problems into three-single phase problems [12]. It is used when the power transmission lines are fully transposed. Transposing the conductors at phase *a*, *b* and *c* along the line in three sections through a specific tower makes the long three-phase transmission lines balanced, Figure 18 shows a diagram of a three-phase transmission line transposed at three locations.

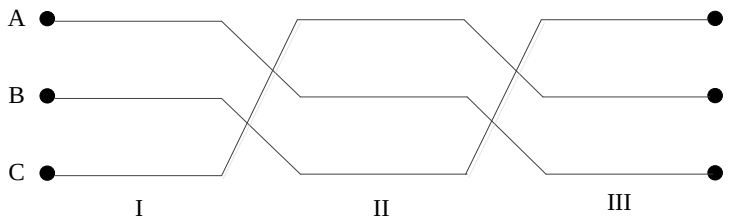

Figure 18. Transposition scheme for single three-phase transmission line [11]

The main advantage of Clarke's transformation over the symmetrical component transformation is that, the Clarke's transformation matrix elements are real. It is given as [11]

$$T_{clark} = \frac{1}{\sqrt{3}} \begin{bmatrix} 1 & 1 & 1 \\ \sqrt{2} & \frac{-1}{\sqrt{2}} & \frac{-1}{\sqrt{2}} \\ 0 & \frac{\sqrt{3}}{\sqrt{2}} & \frac{-\sqrt{3}}{\sqrt{2}} \end{bmatrix} \tag{3.55}$$

$$V_{mode} = T_{clark} V_{phase} \text{ and } I_{mode} = T_{clark} I_{phase} \tag{3.56}$$

The three decoupled modal systems are represented by using the constant parameter line model or FD line model for each separate mode. The schematic diagram of transformation between phase and modal domain on a three-phase transmission line is shown in Figure 19.

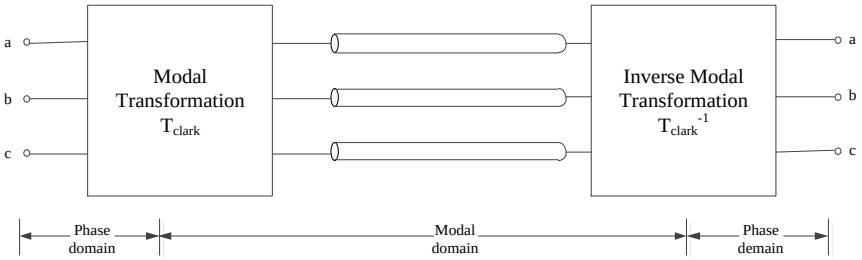

Figure 19. Transformation between phase and modal domain on a three-phase transmission line [11]

The three modal domain line equations are solved independently. The inverse modal transformation is then used to express the voltages and currents in phase domain.

The impedance matrix of a three-phase transmission line is as

$$z_{ph} = \begin{bmatrix} Z_{aa} & Z_{ab} & Z_{ac} \\ Z_{ba} & Z_{bb} & Z_{bc} \\ Z_{ca} & Z_{cb} & Z_{cc} \end{bmatrix} \tag{3.57}$$

where Z_{ii} is the self-impedance of the line and Z_{ij} is the mutual impedance between the phases i and j (in transposed lines, Z_{ij}=Z_{ji}). The phase voltages and currents are related to each other through the following equation

$$V_{ph} = Z_{ph} I_{ph} \tag{3.58}$$

The above equation is represented in the modal domain by using the modal transformation as

$$T_{clark}^{-1} V_{mode} = Z_{ph} T_{clark}^{-1} I_{mode} \tag{3.59}$$

$$V_{mode} = T_{clark} Z_{ph} T_{clark}^{-1} I_{mode} \tag{3.60}$$

$$Z_{mode} = T_{clark} Z_{ph} T_{clark}^{-1} \tag{3.61}$$

where Z_{mode} has the form as

$$z_{mode} = \begin{bmatrix} Z_s + 2Z_m & 0 & 0 \\ 0 & Z_s - Z_m & 0 \\ 0 & 0 & Z_s - Z_m \end{bmatrix} \tag{3.62}$$

where Z_s is the self-impedance of the transmission line (assuming that Z_{aa}=Z_{bb}=Z_{cc}) and Z_m is the mutual impedance between phases (assuming that Z_{ab}=Z_{bc}=Z_{ac}).

The modal transformation of untransposed transmission line is derived from the eigenvalue/eigenvector theory by using [Z_{ph}] and [Y_{ph}] matrices [11]. The voltage and current equations along the transmission lines are as

$$\frac{dV_{ph}}{dx} = -Z_{ph} I_{ph} \tag{3.63}$$

$$\frac{dI_{ph}}{dx} = -Y_{ph} V_{ph} \tag{3.64}$$

where Z_{ph} and Y_{ph} are the phase impedance and admittance matrices of the transmission line per unit of length. The second-order differential equations for voltages and currents are obtained as

$$\frac{d^2V_{ph}}{dx^2} = Z_{ph}Y_{ph}V_{ph} \tag{3.65}$$

$$\frac{d^2I_{ph}}{dx^2} = Y_{ph}Z_{ph}I_{ph} \tag{3.66}$$

The above coupled phase equations are transformed into decoupled modal equations using the eigenvalue/eigenvector theory as

$$\frac{d^2V_{mode}}{dx^2} = \Lambda V_{mode} \tag{3.67}$$

where $V_{mode} = T_v V_{ph}$ and $\Lambda = T_v^{-1} Z_{ph} Y_{ph} T_v$.

T_v, the voltage modal transformation is the matrix of the eigenvectors of the matrix, $Z_{ph}Y_{ph}$. As the current modal transformation T_i is obtained using eigenvectors of the matrix, $Y_{ph}Z_{ph}$, it is related to T_v as, $T_i = T_v^{t^{-1}}$.

3.3. A Review of Fault Location Methods

Fault location methods use single-ended, double-ended or multi-ended information (i.e. voltage and current) for each phase to accurately locate the fault in transmission lines. As it is mentioned before, the fault location techniques are divided into three main categories as:

1. Power frequency based methods,
2. Traveling wave based methods, and
3. Artificial Intelligence based methods.

The most common fault location methods proposed in the literature are briefly reviewed in the following sections. As it is explained previously, the power frequency-based and some of the artificial intelligence-based fault location methods use steady-state voltages and currents and perform the analyses using steady-state model of transmission lines. Traveling wave-based and some other artificial intelligence-based methods rely on transient voltage and current measurements and the methods are implemented using transient model of transmission lines.

3.3.1. Power Frequency-Based Methods

The power frequency-based methods, known also as impedance-based methods are the most common fault location methods used in protection schemes. The main idea of these methods is to

calculate the apparent impedance by looking into the line from one end [17]. These methods are developed using single-ended, two-ended or multi-ended voltage and current measurements. Accurate fault location using impedance-based methods, requires successful extraction of the voltage and current phasor quantities.

A) Single-ended impedance-based technique

Single-ended impedance-based fault location technique locates the fault by calculating the apparent impedance seen from one end of the line. To locate all fault types, the phase-to-ground voltages and currents in each phase must be measured.

If the fault resistance is assumed to be zero, the equations given in Table 1 are used to calculate the fault location [17].

Table 1. Simple impedance equations

Fault Type	Positive Sequence Impedance Equations (mZ_{1L})
a-g	$V_a/(I_a+3kI_0)$
a-b or a-b-g	V_{ab}/I_{ab}
a-b-c	V_{ab}/I_{ab}, V_{ac}/I_{ac} *or* V_{bc}/I_{bc}

where

k is $(Z_{0L}-Z_{1L})/3Z_{1L}$,

Z_{0L} is the zero sequence line impedance,

Z_{1L} is the positive sequence line impedance,

m is the per unit distance to fault (e.g. distance to fault divided by the total line length),

I_0 is the zero sequence current.

The distance to the fault from the sending end is determined by knowing the line impedance per unit. The single-ended fault location accuracy is affected by factors not represented by equations mentioned in Table 1. The challenges are summarized as [17]:

- The combined effect of the load current and fault resistance,
- Inaccurate fault type (faulty phases) identification,
- Influence of zero-sequence mutual effects on the components,
- Uncertainty about the line parameters, particularly zero-sequence impedance
- Insufficient accuracy of the line model (e.g. untransposed lines are represented as being transposed, and charging capacitance is not considered),
- Presence of shunt reactors and series capacitors,
- Load flow unbalance.

To address the above mentioned challenges and to improve the fault location accuracy, more complex and accurate fault location techniques have been developed in the literature, and they are reviewed in the following sections.

A.1. Simple reactance method

The single line diagram of a transmission line is shown in Figure 20.

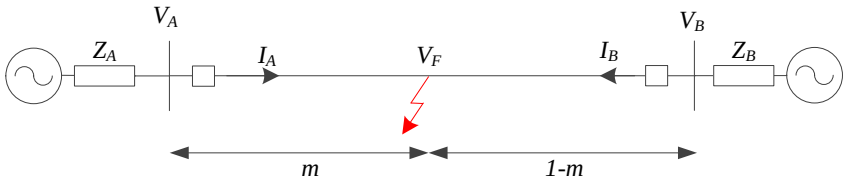

Figure 20. One-line diagram of a transmission line with a fault

In the simple reactance method, the apparent impedance seen from the sending end is calculated. The method assumes that the current through the fault resistance is in phase with the current at the measurement point, and there is no load prior to the fault. The ratio of the measured reactance to the reactance of the entire line gives the per-unit distance to the fault (m). The fault location for phase-phase, phase-phase-ground and 3ϕ fault is calculated as

$$m = \frac{Im\left(\frac{V_A}{I_A}\right)}{Im(Z_L)} \tag{3.68}$$

where V_A and I_A are the fault phase-phase voltage and current at bus A. (e.g. for *a-b* fault, V_A=V_a-V_b and I_A=I_a-I_b).

For single-line-to-ground (SLG) faults, the fault distance to the measurement bus (bus A) is calculated using the following equation

$$m = \frac{Im\left(\frac{V_A}{I_A + 3kI_{0A}}\right)}{Im(Z_{1L})} \tag{3.69}$$

where V_A and I_A are the fault phase-ground voltage and current at bus A. I_{0A} is the zero sequence current at bus A.

The method's error is small, if the fault resistance is negligible or if I_A and I_F are in phase. For high impedance faults (HIF), the algorithm introduces considerable reactance error which results in an error in the fault location. The algorithms, described in the next sections, have been developed to compensate for the reactance effect.

A.2. Fault location methods without using source impedance

In order to improve the fault location accuracy, elimination of load current by determining the change in current after the occurrence of a fault is used. Takagi et al. [18], Erikson et al. [19], and Novosel et al. [20] proposed the improved fault location equation as

$$m = \frac{Im(V_A \Delta I_A^*)}{Im(Z_L I_A \Delta I_A^*)} \tag{3.70}$$

where ΔI_A is the change of the sending end current from pre-fault to post-fault condition.

In the above fault location equation, the current distribution factor (d_s=$\Delta I_A/I_F$) is assumed to have zero angle (β=0). In an improved single-ended fault location (i.e. modified Takagi), the zero sequence current is used instead of ΔI_S. The proposed equation is given as

$$m = \frac{Im\left(3V_A I_0^* e^{-j\beta}\right)}{Im(3Z_{1L} I_A I_0^* e^{-j\beta})} \tag{3.71}$$

where β is the correction angle which is calculated by using the source impedance data. Z_{1L} is the positive sequence impedance of the line.

A.3. Fault location methods using source impedance

The fault location technique using source impedances was proposed by Erikson et al. [19]. Fault location (m) is calculated using a quadratic function as

$$m^2 - k_1 m + k_2 + k_3 R_f = 0 \tag{3.72}$$

where

$$k_1 = \frac{V_A}{I_A Z_L} + 1 + \frac{Z_B}{Z_L}$$

$$k_2 = \frac{V_A}{I_A Z_L}\left(1 + \frac{Z_B}{Z_L}\right)$$

$$k_3 = \frac{I_{FA}}{I_A Z_L}\left(1 + \frac{Z_A + Z_B}{Z_L}\right)$$

k_1, k_2 and k_3 are complex indexes which are function of local voltages, currents and source impedances. The voltages and currents needed to calculate the indexes, are determined according to the fault type by using the quantities given in Table 2.

Table 2. Voltage and current quantities needed for different fault types

Fault Type	V_A	I_A	I_{FA}
a-g	V_a	I_a+3kI_0	$3/2(\Delta I_a-I_{0A})$
a-b or a-b-g	V_{ab}	I_{ab}	ΔI_{ab}
a-b-c	V_{ab}, V_{ac} or V_{bc}	I_{ab}, I_{ac} or I_{bc}	ΔI_{ab}, ΔI_{ac} or ΔI_{bc}

The complex expression of equation (3.71) is separated into two equations: one real and one imaginary equation. By eliminating R_F, a single expression is obtained with the single unknown m.

The fault location method using source impedance is not sensitive to the reactance effect but requires the source impedances as the input parameters, which are not always provided.

Another fault location method for transmission lines using single-ended measurements is proposed in [21]. Due to the current transformer saturation, the pre-fault and post-fault voltages

and the pre-fault current phasors are utilized. The remote terminal pre-fault voltages and currents are calculated using the local terminal pre-fault voltages and currents and the steady-state transmission line model. The fault injection currents at local and remote buses are calculated using the pre-fault voltages. The post-fault three-phase voltages at local and remote buses are calculated according to the classified fault type using the calculated fault injection currents and line parameters. The method is performed iteratively for the discrete fault points along the transmission line. The point which minimizes the difference between calculated and measured post-fault voltage at the local bus for all three phases is selected as the fault point.

In [22], two algorithms are developed for fault location in transmission lines by utilizing only current phasors. In the first algorithm, the three phase current phasors and zero sequence impedance of the line are used. Zero sequence current at the fault location is not measurable, but it can be expressed in terms of the input zero sequence current and parameters from the zero sequence equivalent circuit of the transmission line. The negative sequence current at fault location is also calculated by using the input zero sequence current and zero sequence equivalent circuit. For a phase to ground fault, the sequence currents at the fault point are equal to each other. By equalizing the obtained zero and negative sequence current, the fault location is calculated. In the second proposed method, to avoid the use of zero sequence diagram of the transmission line, the pre-fault load current phasor as well as positive sequence current are utilized to derive the fault location formula.

In [23], application of adaptive Kalman filtering in fault classification, distance protection and fault location using single-ended voltage and currents data is developed. The Kalman filter is used for fault classification. The method mentioned in section A.1 is used for fault location.

The small ground current in non-direct-ground neutral transmission lines is a challenge for fault location. Single-ended fault location for transmission lines with the non-direct-ground neutral system is proposed in [24]-[26]. The π equivalent model of the transmission line with lumped parameters is used to derive the fault location equation. Consecutive samples of faulty phases and ground mode voltage and current are used to calculate the derived equation indexes. The equation is solved using iterative Newton-Raphson method.

B) Two-ended impedance-based method

Two-ended fault location methods are more accurate than single-ended methods and are able to minimize the effects of fault resistance, loading, and charging current. Fault type does not need to be known. Therefore, positive-sequence components are used rather than zero-sequence, which eliminates adverse effects of zero-sequence components. Two-ended methods are performed using synchronized or unsynchronized measurements which are reviewed in the following sections.

B.1. Synchronized two-ended fault location

Synchronized two-ended fault location methods are well reviewed and described in [1], [17] and [27]-[32]. As it is shown in Figure 20, the fault is at location *m* of the line from Bus A and (1–*m*) from Bus B. The voltage at the fault point, V_F calculated from bus A and B is expressed as

$$V_F^A = \cosh(\gamma m l)\, V_A + Z_c \sinh(\gamma m l)\, I_A \tag{3.73}$$

$$V_F^B = \cosh(\gamma (1-m) l)\, V_A + Z_c \sinh(\gamma (1-m) l)\, I_A \tag{3.74}$$

where $V_F{}^A$ and $V_F{}^B$ are the calculated voltage at the fault location from bus A and bus B respectively.

As $V_F{}^A$ and $V_F{}^B$ are the same, equations (3.72) and (3.73) are rearranged and the fault location (m) is calculated using the following equation

$$m = \frac{1}{\gamma_{pos} l} \tanh^{-1}\left(\frac{\cosh(\gamma_{pos} l)\, V_B^{pos} - Z_c^{pos} \sinh(\gamma_{pos} l) I_B^{pos} - V_A^{pos}}{\sinh(\gamma_{pos} l)\, V_B^{pos} - Z_c^{pos} \cosh(\gamma_{pos} l) I_B^{pos} - Z_c^{pos} I_A^{pos}}\right) \tag{3.75}$$

where $V_A{}^{pos}$, $V_B{}^{pos}$, $I_A{}^{pos}$ and $I_B{}^{pos}$ are the positive-sequence voltage and current phasors obtained at bus A and B. γ_{pos} and $Z_c{}^{pos}$ are the positive-sequence propagation constant and characteristic impedance, respectively.

B.2. Unsynchronized two-ended fault location

Unsynchronized two–ended fault location technique for transmission line is proposed in [33]-[35]. Considering the fault in Figure 20, the voltage at the fault point, V_F is determined as

$$V_F^A = V_A - mZI_A \tag{3.76}$$

$$V_F^B = V_B - (1-m)ZI_B \tag{3.77}$$

where Z is the impedance of the line.

Measurements at bus A and B are not synchronized and the synchronization angle between bus A and B is δ. The voltage at bus A and B is written as

$$V_A = |V_A| \angle \alpha_m + \delta \tag{3.78}$$

$$V_B = |V_B| \angle \beta_m \tag{3.79}$$

where α_m and β_m are the measured angles and δ is the angle needed to synchronize the phasors at Bus A to those at Bus B. Similar equations can be written for the currents. Combining equation (3.75) and (3.76), the following equation is obtained

$$V_A e^{j\delta} - V_B + ZI_B = mZ(I_A e^{j\delta} + I_B) \tag{3.80}$$

where m and $e^{j\delta}$ are the unknowns.

If equation (3.79) is separated into real and imaginary terms and manipulated, the following one unknown equation is obtained

$$a \sin(\delta) + b \cos(\delta) + c = 0 \tag{3.81}$$

where

$$a = -C_3 Re\{V_A\} - C_4 Im\{V_A\} - C_1 Re\{V_B\} - C_2 Im\{V_B\} + C_1 C_3 + C_2 C_4$$

$$b = C_4 Re\{V_A\} - C_3 Im\{V_A\} - C_2 Re\{V_B\} + C_2 Im\{V_B\} + C_2 C_3 - C_1 C_4$$

$$c = C_3 Re\{V_A\} - C_1 Im\{V_A\} - C_4 Re\{V_B\} + C_3 Im\{V_B\}$$

The coefficients C_1, C_2, C_3 and C_4 in the above equations are defined as

$$C_1 = RRe\{I_A\} - XIm\{I_A\}$$

$$C_2 = RRe\{I_A\} + XIm\{I_A\}$$

$$C_3 = RRe\{I_B\} - XIm\{I_B\}$$

$$C_4 = RRe\{I_B\} + XIm\{I_B\}$$

Equation (3.80) is solved using an iterative Newton-Raphson method. Once the synchronization angle (δ) is obtained, fault location is calculated using the following equation

$$\mathrm{m} = \frac{Re\{V_A\} sin\delta + Im\{V_A\} \cos(\delta) - Im\{V_B\} + C_4}{C_1 sin\delta + C_2 cos\delta + C_4} \tag{3.82}$$

In all above equations, if the positive-sequence voltages and currents are used, the fault type is not needed to be known.

A fault location method for transmission line based on synchronized sampling of the voltage and current from the two ends of the line is proposed in [36]. The partial differential equations of the long line steady-state model are solved in time-domain using voltage and current samples from both ends of the line over a period of around one cycle after the fault. The fault location is determined as the point along the line where the voltages computed using the sending end data and the receiving end data are the same, or closest to each other, when compared to other points in the line.

[37] presents a two-ended fault location algorithm for power system transmission lines. The pre-fault and during-fault unsynchronized voltages and currents from both ends of a line are taken as the inputs. The proposed method uses the equivalent π line model to develop the fault location equations. The iterative least square approach is used to estimate the fault location. In absence of pre-fault data, negative-sequence voltage and currents are utilized for fault location. However the methods fail to give satisfactory results in 3ϕ and *LLG* faults. The impacts of measurement error on the same fault location method are considered in [38]. In [37] the synchronization error between two buses is considered to be unknown and it is estimated using the iterative least square approach. However, the synchronization error in [38] is assumed to be known.

A fault location method in a parallel transmission line using two-ended synchronized/unsynchronized currents is presented in [39]. The coupled differential equations of parallel transmission lines are decoupled into common component nets and differential component nets. Since the voltages at the two ending buses of the differential component net of a parallel transmission line are zero, only two terminal currents are needed to locate faults on the differential component net. The time-domain voltage equations in differential component net using two-ended synchronized currents are solved. The fault location is the point along the line which gives the minimum error between calculated voltages using the two ending buses current independently. The effect of unsynchronized data is also considered when the error between two calculated voltages is minimized.

A fault location method in transmission lines considering current transformers saturation is proposed in [40]. The basic idea of the algorithm is to find the fault point which can minimize the difference between the calculated phasor voltages at that point, using local and remote buses voltages and currents. However due to the saturation of CTs, the calculated fault resistance as well as the calculated time-domain voltage difference need to be minimized. Thus, the algorithm gives results of the fault distance and the phasors of the unknown saturated current. Due to lack of information from both ends, the fault type is needed to be known to derive the method.

C) Other fault location applications

C.1. Three terminal transmission system

Three-terminal transmission systems with tapped transmission lines are occasionally used to decrease the cost of transmission line installation. The one-line diagram of a three-terminal (teed) transmission system is shown in Figure 21.

Fault location in three-terminal transmission systems represents a problem due to the infeed currents from three terminals and presence of fault resistance. There are various types of fault location methods proposed for teed transmission systems using impedance-based method.

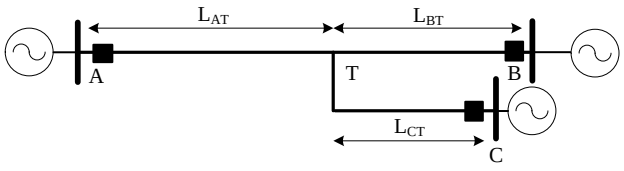

Figure 21. Three-terminal power transmission system

In [41], three terminal synchronized and unsynchronized voltage and current phasors are used for fault location. The two-ended fault location using two terminal voltages and currents phasors for sections, A-B and A-C is solved independently. The faulty line is identified according to the two calculated fault distance using a simple if-rule condition. In the case of unsynchronized data, the two fault distances are obtained by using iterative least square methods developed in section B.2

In [42] a method based on synchronized voltage and current measurements from three buses is developed. Faulty line identification is the first step in the developed algorithm. Three buses voltages and currents are used to estimate the voltage at the tee-point and identify the faulty line based on the calculated voltage. For instance if the fault is in the line A-T, then the voltage estimated at the tee-point using phasors at ends B and C would be identical whereas that estimated from end A would be very different, indicating that the faulty line is A-T. The other faulty lines are similarly identified. The fault location is then calculated by using two-ended synchronized fault location method.

A method of fault location for three-terminal two parallel transmission lines is proposed in [43]. The method uses only the magnitude of the differential currents at each terminal between two parallel lines. The distance is calculated for all three sections using the derived formulas. If there is a fault point between a certain terminal and the tee-point, the result derived from the corresponding formula of that terminal is less than the line length, or if there is no fault between the terminal and the tee-point, the result derived from the formula of that terminal is greater than line length.

A method for accurate fault location in three-terminal transmission systems using phasor measurement unit (PMU) is developed in [44]. The data (voltage and current) measured at two terminals of the teed transmission system is used for accurate fault location. The fault distance using synchronized voltage and currents from two buses is calculated first. The calculated distance is then compared to the length of the line from sending end to the tee-point to identify the faulty line. For the faults in the lines which have one measurement, the two ended fault location is utilized using one-end measurements and estimated voltages and currents at the tee point. Once the fault is identified in the line with no measurements at its local bus, the voltage at that bus is first estimated using pre-fault voltages and current from the other buses according to the classified fault type. The estimated post-fault voltage and current at the tee-point as well as the estimated voltage of the bus are used to calculate the fault location.

[45] presents another method for fault location in three-terminal transmission systems. Fault location and faulty line identification is performed using synchronized three-phase currents from all three terminals as well as three-phase voltages from one terminal which the fault locator is

installed. The proposed fault location consists of three subroutines. For the first subroutine, the voltages and currents at the local bus and fault current contribution from the other two buses are used to calculate the fault distance and resistance. For the other two subroutines, the voltage and current at the tee-point are first estimated using the voltage and current from the main bus. The equivalent π model of the transmission line is considered for estimation of the voltages and currents at the tee-point. The estimated voltages and currents are then used to derive the equations for fault distance and resistance calculation.

C.2. Series compensated transmission line

The series capacitor (SC) compensation in transmission lines is used to increase the power-transfer capability, to improve the power system stability and to decrease transmission losses.

The series capacitor is protected against high voltage transients during faults using Metal Oxide Varistor (MOV). The one-line diagram of a MOV-protected series compensated transmission line is shown in Figure 22.

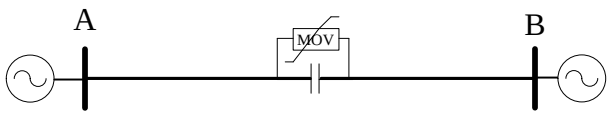

Figure 22. MOV-protected series compensated transmission line

The MOV is installed directly across the series capacitor and has nonlinear *i-v* characteristics approximated as

$$i = I\left(\frac{V}{V_{ref}}\right)^{q} \tag{3.83}$$

The voltage waveforms recorded at the sending end change due to the nonlinear characteristics of MOV during the fault by limiting the overvoltage across the series capacitor. This phenomenon affects the accuracy of impedance-based fault location techniques.

A single-ended fault location method for series compensated lines is presented in [46]. The algorithm uses single-ended phase measurements (*abc*) instead of symmetrical components (012). The voltage drop of series capacitor is computed by the device model for different

currents level. The fault location calculation is performed through two independent subroutines; one for faults behind the SCs, and the other one for faults in front of the SCs. For the second subroutine as the current through the SC is unknown, an iterative method is used to calculate the fault location. The correct fault side is then selected based on a simple if-rule.

A fault location method using PMU data is presented in [47] and [48]. Two independent subroutines for faults behind the SC and the ones in front of SCs are used to calculate the fault location. The fault location for each subroutine is composed of two steps. First the initial fault location is calculated using the two-ended synchronized voltage and current measurements according to the classified fault. Then the voltage drop across the SC is calculated using the line parameters and the calculated voltage at the fault point. The calculated voltage after the series capacitor as well as the remote end voltages and currents are used to correct the fault location. Once the fault location is obtained in each subroutine, a simple if-rule developed in [46] is used to determine the side of the fault.

In [49], a method for fault location in series compensated transmission lines is presented. The time-domain voltage across the SC is estimated using a non-linear equation. The estimated voltage drop, two-ended synchronized voltages and currents are used to calculate the fault distance for the fault behind and in front of SC independently. Since the SC is installed in the middle of the line, just one of the calculated distances is within its corresponding range.

3.3.2. Traveling Wave-Based Methods

Traveling waves on power transmission lines arise from a number of causes such as faults, switching operations, and lightning. Traveling waves on overhead lines travel at the speed of light, approximately 3×10^8 m/sec [1.8×10^5 mile/sec]. They consist of a voltage wave and a current wave which is related to the voltage wave through the characteristic impedance of the line, Z_c. This relationship between the voltage and current waves exists at all points along the line except at discontinuities such as line terminations and fault locations. At all discontinuities, traveling wave is divided into two portions; reflected and refracted waves.

Traveling wave-based methods utilize the very fast transients initiated by a fault. Fast transients are composed of very high frequencies varying from kHz to MHz comparing to steady state frequency, 60 Hz. These transients are evolved according to the forward and backward

traveling waves propagating along the transmission lines with a velocity near the speed of light. Traveling wave based fault location methods are fast and accurate, however they need an appropriate measurement which is able to detect the voltage or current transients with very high sampling frequency (e.g. 200 kHz).

A brief overview of traveling wave based fault location methods can be found in [50]. In [51], traveling wave-based distance protection for a transmission line is presented. Any disturbance (e.g. fault, lightning, switching) on a transmission line results in the initiation of traveling waves. These waves propagate along the line being continually attenuated and distorted until they die out. At a discontinuity, a part of the wave is reflected back along the line and a part may pass to other sections of the system. The operating principle of the method relies on the fault being a low impedance discontinuity as compared with the characteristic impedance of the line. This will reflect a similar voltage wave of opposite polarity and a similar current wave of like polarity to the incident voltage and current wave respectively. The Bewley diagram corresponding to the wave propagation initiated by a fault in a transmission line with the polarity changes is given in Figure 23. The proposed fault location method is summarized as the following steps:

1. The voltages and currents at the relay location are measured with the sampling frequency of f_s (the time interval of Δt).
2. The measured voltages and currents are separated into two components as the pre-fault steady-state and the transient components.
3. The transient voltages and currents are obtained by subtracting the post-fault signals from the steady state pre-fault component.
4. Modal transformation is applied to the obtained transient voltages and currents as

$$V_m = \frac{1}{3}\begin{bmatrix} 1 & 1 & 1 \\ \frac{3}{2} & 0 & -\frac{3}{2} \\ \frac{1}{2} & -1 & \frac{1}{2} \end{bmatrix} V_{abc} \tag{3.84}$$

$$i_m = \frac{1}{3}\begin{bmatrix} 1 & 1 & 1 \\ \frac{3}{2} & 0 & -\frac{3}{2} \\ \frac{1}{2} & -1 & \frac{1}{2} \end{bmatrix} i_{abc} \tag{3.85}$$

5. The transient components corresponding to the aerial mode (mode 2) of voltages and currents are considered to calculate the relaying signals S_1 and S_2 as follows

$$S_1 = Z_c i_m - V_m \tag{3.86}$$

$$S_2 = Z_c i_m + V_m \tag{3.87}$$

where Z_c is the characteristic impedance of the line, i_m and V_m are the modal transient currents and voltages respectively.

6. The mean values of S_1 and S_2 over the sampling period ($n=1:N$) are removed from the relaying signals S_1 and S_2 as

$$\widetilde{S_1}(n\Delta t + m\Delta t) = S_1(k\Delta t + m\Delta t) - \frac{1}{N}\sum_{k=1}^{N}[S_1(k\Delta t + m\Delta t) \quad n = 1{:}N \;\&\; m = 0{:}M$$

$$\widetilde{S_2}(n\Delta t) = S_2(k\Delta t) - \frac{1}{N}\sum_{k=1}^{N}[S_2(k\Delta t) \quad n = 1{:}N$$

7. The cross-correlation between $\widetilde{S_1}$ and $\widetilde{S_2}$ is calculated as

$$\phi(m\Delta t) = \frac{1}{N}\sum_{k=1}^{N}\left[\widetilde{S_1}(k\Delta t + m\Delta t)\right]\left[\widetilde{S_2}(k\Delta t)\right] \tag{3.88}$$

8. The cross correlation is calculated for different m, changing from 0 to large numbers.
9. The cross-correlation shows the similarity between the two waveforms. The maximum output of the correlation function indicates the best match between the two waveforms. The corresponding time delay ($m\Delta t$) when this occurs is used to determine the distance to the fault as

$$x = \frac{v \times m\Delta t}{2} \tag{3.89}$$

where v is the traveling wave velocity for the considered mode.

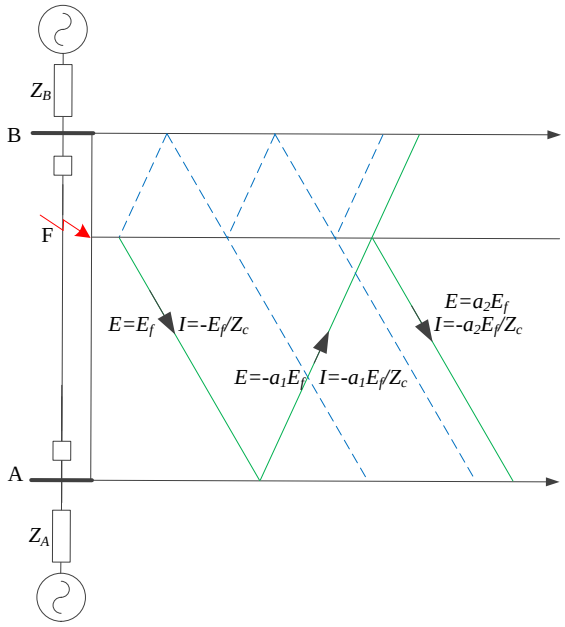

Figure 23. Traveling wave propagation initiated by a fault

The indexes a_1 and a_2 in Figure 23 are the reflected wave coefficients. The values of a_1 and a_2 are dependent on the line characteristic impedance and the source impedance behind the buses A and B.

In [52] a single-ended traveling wave-based fault location method for two and three terminal transmission systems is presented. Voltages and currents at discrete points along the transmission line are estimated by solving the traveling wave equation iteratively. Then, three functions calculated using the estimated voltages and currents at all discrete points along the line are used to determine the fault location. The voltages $V(x_i,t_j)$ and currents $I(x_i,t_j)$ at discretized locations along the transmission line for each sampling interval Δt is estimated as

$$V(\mathrm{x_i},\mathrm{t_j}) = \frac{1}{2}\left(V(\mathrm{x_{i-1}},\mathrm{t_{j+1}}) + V(\mathrm{x_{i-1}},\mathrm{t_{j-1}})\right) + \frac{2\gamma+\eta\Delta x}{4} I(\mathrm{x_{i-1}},\mathrm{t_{j+1}}) - \frac{2\gamma-\eta\Delta x}{4} I(\mathrm{x_{i-1}},\mathrm{t_{j-1}}) + \frac{\eta\Delta x}{2} I(\mathrm{x_i},\mathrm{t_j}) \quad (3.90)$$

$$V(\mathrm{x_i},\mathrm{t_j}) = \frac{1}{2}\left(V(\mathrm{x_{i-1}},\mathrm{t_{j+1}}) - V(\mathrm{x_{i-1}},\mathrm{t_{j-1}})\right) + \frac{2\gamma+\eta\Delta x}{4\gamma} I(\mathrm{x_{i-1}},\mathrm{t_{j+1}}) - \frac{2\gamma-\eta\Delta x}{4\gamma} I(\mathrm{x_{i-1}},\mathrm{t_{j-1}}) \quad (3.91)$$

where $\eta = rc$ and $\gamma = \sqrt{lc}$.

From the above equations, $V(x_i,t_j)$ and $I(x_i,t_j)$ are computed recursively from the initial data ($V(0,t_j)$ and $I(0,t_j)$) at each discrete point x_i at intervals of Δx.

The fault location is derived using the following basic functions

$$F_1(x) = \frac{1}{T-2\gamma x}\int_{\gamma x}^{T-\gamma x} V^2(x,t)dt \qquad \text{for } x < \frac{T}{2\gamma} \tag{3.92}$$

$$F_2(x) = \frac{1}{T-2\gamma}\int_{\gamma x}^{T-\gamma x} I^2(x,t)dt \qquad \text{for } x < \frac{T}{2\gamma} \tag{3.93}$$

$$F_3(x) = \frac{1}{T-2\gamma x}\int_{\gamma x}^{T-\gamma x} [V^2(x,t) \times I^2(x,t)]dt \quad \text{for } x < \frac{T}{2\gamma} \tag{3.94}$$

Fault location is determined based on the second derivative of the above equations as

$$G_1(x) = \frac{d^2F_1(x)}{dx^2} \tag{3.95}$$

$$G_2(x) = \frac{d^2F_2(x)}{dx^2} \tag{3.96}$$

$$G_3(x) = \frac{d^2F_3(x)}{dx^2} \tag{3.97}$$

The x which has the maximum values of $G_1(x)$, $G_2(x)$ and $G_3(x)$ is the fault location.

More recently, in [53], the use of the discrete wavelet transform (DWT) of the modal voltages is proposed to estimate the location of the fault in a transmission line. Traveling wave theory is utilized to capture the travel time of the transient voltage along the line between the fault point and the relay. Wavelet transform is used to obtain the time resolution of high frequency components of the fault transients. The paper proposed two algorithms for fault location as:

- Two-ended synchronized measurements,
- Single-ended measurement

A) Two-ended synchronized measurements

Phase voltages are measured simultaneously at both ends of the transmission line using the same time reference synchronized using Global Positioning Satellite (GPS) receivers. The measured voltages are transformed into modal components. DWT is applied to the aerial mode (mode 1) voltages at both ends. As it is shown in Figure 24, t_a and t_b correspond to the first traveling waves at bus A and B respectively. The initial peaks in aerial mode voltage wavelet transformation coefficients (WTC) in scale-1 are used to extract the arrival times.

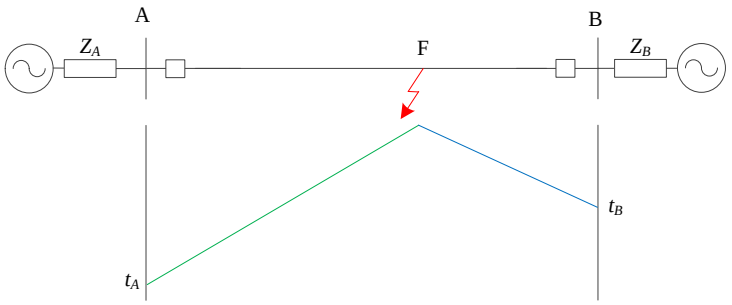

Figure 24. Lattice diagram for two-ended synchronized measurements

The delay between the fault detection time at two ends ($\Delta t = t_A - t_B$) is used to calculate the fault location as

$$x = \frac{l - v\Delta t}{2} \tag{3.98}$$

where l is the length of the line and v is the propagation velocity at aerial mode along the transmission line calculated at the frequency corresponding to the middle value of scale-1.

B) Single-ended measurement

Another method that does not require remote end synchronization is single-ended measurements. In this method, due to the lack of any other time reference, all time measurements are with respect to the instant when the first traveling wave is detected. Therefore, the fault location calculation is based on the reflection times of the traveling waves from the fault point or the remote end. Lattice diagram illustrating the reflection and refraction of traveling waves initiated by the fault transients due to faults in the first and the second half of the line is shown in Figure 25.

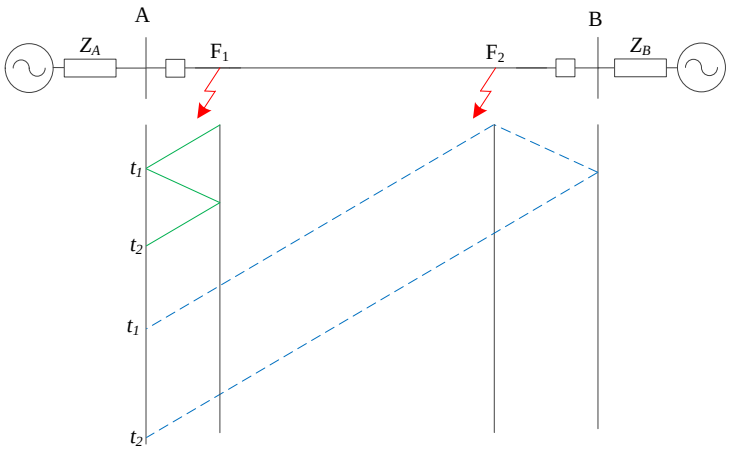

Figure 25. Lattice diagram of the fault in the first and the second half of the line

As it is observed from Figure 25, for a fault in the first half of the line, the first two traveling waves are those reflected from the fault point. Thus, by measuring the delay between the first two peaks (Δt) in the wavelet transform coefficient, the fault location is calculated as

$$x = \frac{v\Delta t}{2} \tag{3.99}$$

If the fault is in the second half of the line, the second traveling wave is the one from the remote end. Therefore, the fault location is calculated by using

$$x = l - \frac{v.\Delta t}{2} \tag{3.100}$$

As propagation velocities along the transmission line at aerial mode and ground mode are different, the faulty half of the line is determined by comparing the delay between arrival time of traveling waves in the aerial mode and ground mode.

C) Other traveling wave-based fault location applications

In [54], a single-ended traveling wave-based fault location is proposed for teed transmission systems. DWT is applied to the aerial mode voltages at three buses to identify the faulty line. Fault initiated lattice diagram is then utilized for fault location.

A transient-based technique for high speed protection of the transmission line is proposed in [55]. Comparison of traveling times of the fault generated high frequency transient current signals at the local buses is used to determine the fault section.

In [56], a wavelet based high speed directional protection in transmission lines is proposed. Comparison of voltage and current traveling wave polarities at the designated bus is used to detect the fault direction. DWT is applied to the measured voltages and currents to extract transient information (polarities and arrival instants). If a forward fault occurs, forward direction being from the designated bus to the transmission line, the arriving voltage and current traveling waves are of opposite signs. On the other hand, for a backward fault, the arriving voltage and current traveling waves have the same signs.

[57] presents a transient-based protection of transmission lines. Fault initiated high frequency transient information extracted from the modal voltages is used for fault section identification. Complex wavelet transformation is applied to the modal voltages. Voltage traveling wave polarities at the transmission buses are compared to detect the faulty line.

A traveling wave-based fault location method for cable transmission system is proposed in [58]. DWT is applied to the synchronized voltage measurement at both ends of the cable. Two-ended traveling wave-based method is used for fault location.

The traveling wave approach is the fastest and the most accurate approach among the fault location techniques. However, the traveling wave-based fault location techniques are sensitive to close-up faults where the fault is located very close to terminals. In [59] the use of principle component analysis (PCA) is proposed to overcome the problem of close-up faults. The PCA is used to detect the arriving times of traveling wave based on of voltage and current DWT coefficients.

In [60] a single-ended traveling wave-based fault location algorithm is proposed for a transmission system including an overhead line combined with an underground cable. The method uses pre-calculated indices, which are obtained from the modal voltage DWT coefficients, for section identification. Fault initiated lattice diagram is then used for exact fault location.

3.3.3. Artificial Intelligence-Based Methods

In modern smart grid environment, the complexity of fault location problem increases with the proliferation of unusual topologies such as transmission lines combined with underground

cables, series capacitor compensated transmission lines and three-terminal transmission systems. The use of Artificial Intelligence (AI) to improve the fault location accuracy has been attracting many researchers.

In [61], a fault location method in transmission lines using Artificial Neural Network (ANN) is proposed. The proposed method is implemented for two sets of inputs: first with a voltage input signal and second with a current input signal. The four most dominant harmonic components of voltage or current signals are used as the ANN input.

In [62], the use of ANN for fault location in single and double-circuit transmission line is proposed. During the fault, steady-state three phase voltages and currents, measured at the designated bus, are expressed in per unit with respect to their pre-fault magnitudes as (V_{df}/V_{pf}) and (I_{df}/I_{pf}). The calculated ratios are the input to the ANN fault locator.

A fault classification and location method for transmission lines using NN is presented in [63]. DC, fundamental and three harmonic components of each phase voltage and current are used as the input to the fault type classifier. Once the fault type is classified, the corresponding fault location NN with the same input is utilized to locate the fault.

[64] presents a method for fault classification and location in transmission lines based on Fuzzy and Neural Network approach (FNN). The normalized peaks of steady-state three phase voltages and currents are used as the input to fault classifier. Once the fault type is determined, the mentioned inputs as well as the DC components of three phase voltages and currents are used for the corresponding fault location FNN.

In [65], ANN-based fault location is presented for MOV-protected SC compensated lines. The ANN is used to estimate the time-domain voltage across the SC. Single-ended steady-state voltages and currents are used as the input to the ANN. The voltage after the SC is then calculated using the estimated voltage and the measured voltage the main substation. The single-ended frequency-based fault location method is then utilized.

In [66], an adaptive neural network-fuzzy approach is used to locate the fault in a transmission system including an overhead line combined with an underground cable. Fundamental frequency components of post-fault voltages and currents are used in the proposed

method. The algorithm first classifies the fault type using the trained NN. Another NN determines the faulty section using the same input set. The corresponding NN to the classified fault type and identified section is utilized for fault location.

Support vector machine (SVM) is a statistical data classification method which can find the maximum marginal boundary between different classes of a given data set. As a result it provides the global optimal solution. This property is the main advantage over ANN-based classification methods. In addition the model complexity of SVMs is automatically determined during the training; however, the model complexity of the ANNs (i.e. the number of layers and nodes) needs to be determined by the users. Due to its advantages, the use of SVM in power system research increased in recent years. [67] presents a method of fault location in the power transmission lines. The method uses a hybrid approach, composed of two steps. In the first step, the SVM classifier estimates the initial distance to the place of the fault using the information contained in the fundamental harmonics of the faulty phase voltages and currents. In the second step, the initial estimation of fault location is corrected by using the high-frequency information of faulty phase voltage and current. There is a visible peak in the high-frequency characteristic of the faulty signal which is the function of fault type and fault location. The proposed procedure is dependent on the fault type.

A combined wavelet-SVM technique for fault zone identification in a series compensated transmission line is proposed in [68] and [69]. DWT is applied to the current and voltage measurements to extract the transient information. Subsequently, the transient features are applied as the inputs to the SVM classifier to detect the faulty section of the fault.

A method for fault classification and section identification of the SC-compensated transmission line using SVM is presented in [70]. The half-cycle current measurements at one end are used as the input to the SVM classifiers. Fault type classification is performed using four binary support vectors, SVM_i ($i=1... 4$). The SVMs are trained to identify the faulty phase. SVM_1 is trained to detect the fault at phase *a* while SVM_2 is trained to detect the fault at phase *b* and SVM_3 is trained to detect the fault at phase *c*. SVM_4 is trained to detect whether the fault is grounded or not. The output of each SVM_i ($i=1,..,4$) is either +1 or -1. For example if SVM_1 and SVM_4 are +1 while the other SVMs are -1, this implies a grounded-fault in phase *a*.

In [71] and [72], a hybrid method which is able to detect and locate a fault in power transmission lines is presented. DWT, principal component analysis (PCA), SVM and ANN are incorporated into the method to identify the fault type and location at the same time. Voltage and current measurements during the fault are used as the input to the method. Once DWT is applied to the transient voltage and current measurements, PCA is utilized to extract the dominant wavelet transformation coefficients. The SVM classifiers are used for fault classification. The corresponding NN fault location classifier is used for the determined fault type. The fault location method is dependent on the fault type classification.

3.4. Summary

In this chapter, transmission line models for steady-state and transient analyses are reviewed. Then, existing power frequency-based fault location methods are reviewed followed by a detailed review of traveling wave theory and traveling wave-based fault location methods. Artificial Intelligence-based methods are briefly reviewed at the end of this chapter. Review of Discrete Wavelet Transformation and Support Vector Machine is presented in the next chapter.

Chapter IV: Review of Discrete Wavelet Transformation and Support Vector Machine

4.1. Introduction

The wavelet theory was first developed in the early 20th century and it had become widely used in many scientific and engineering research areas. Wavelet transformation provides frequency analysis of a signal like Fourier analysis. However, unlike the Fourier analysis, which gives frequency spectrum of a signal, wavelet analysis provides a representation in both time and frequency. Thus, wavelet analysis can identify the occurrence time and the frequency of a transient disturbance on a signal.

The fundamental problem of finding a pattern in a given data set was initially introduced in the 16^{th} century. Pattern recognition is concerned with finding some regularity in data through the use of mathematical algorithms. These regularities are then used to perform further actions such as classifying the data. Support vector machine (SVM) is a pattern recognition algorithm which can be used for data classification.

In this chapter, a brief review of Fourier analysis and the relevant limitation is given first. Then a brief overview of wavelet transformation (WT) fundamentals is provided followed by its applications to power system analysis. A brief review of SVM and its applications in power system are presented at the end of this section.

4.2. Fundamentals of Fourier Transformation and its Limitations

In signal procesing, analog signals are defined in the time-domain, and the spectral information of these signals is given in the frequency-domain. The Fourier transformation (FT) is a very powerful mathematical tool to represent spectral information of a given signal and it has very significant physical interpretations in applications. FT is quite inadequate for many applications. First, to extract the spectral information from the analog signal, it takes an infinite amount of time, using both past and future information of the signal to evaluate the spectrum at a single frequency. Moreover, FT does not reflect frequencies that evolve with time. Furthermore,

as the frequency of a signal is directly proportional to the length of its cycle, the time-interval needs to be relatively small to give better accuracy for high-frequency spectral information. The time-interval needs to be relatively wide to give complete information for low-frequency spectral information [73].

FT is not adequate for time-frequency analysis as it does not reveal how the signal's frequency contents vary with time. This deficiency was observed by D. Gabor in 1946. He introduced a time-localization "window function", where the window was shifted in time to cover the whole time-domain, for extracting local information of the FT of the signal. The method is called "short-time Fourier transform (STFT)". For each specific window, a time-localized FT is performed on the signal. Then, the window is moved along the time line, and another FT is performed. FT of the entire signal is performed through such consecutive operations. The segment of the signal within the window function is assumed to be approximately stationary. Thus, the STFT decomposes a time-domain signal into time-frequency representation, and variations of the frequency content of the signal are revealed within the window function. Various types of window functions are developed in the past and each of them is appropriate for a specific type of application. For instance, the Gaussian window is designed to analyze transient signals, and the Hamming and Hann windows are applicable for narrowband, random signals analysis, and the Kaiser-Bessel window is suited for separating two signal components with frequencies very close to each other but with widely different amplitudes [74].

The major disadvantage of the STFT is the resolution tradeoff between time and frequency. Resolutions in time and frequency are determined by the width of moving window. A large window width provides good resolution in the frequency domain, but poor resolution in the time-domain. On the other hand, a small window width provides good resolution in the time-domain and poor resolution in the frequency domain, following the Heisenberg principle. This limitation of the STFT is arising as the result of using a single window for all frequencies and therefore, the resolution of analysis is the same at all locations in the time-frequency.

The wavelet transformation (WT) is another time-frequency analysis tool, similar to the STFT but with more flexibility in time and frequency resolution. The basic difference between WT and STFT is that the wavelet uses a size-adjustable window which is more advantageous

than the fixed window used by STFT. For the local area of the signal with high frequency contents, the window is shorter, while for the local area with low frequency contents, the window is longer.

There are two types of WT as continuous and discrete, which is briefly reviewed in the following section.

4.3. Fundamentals of Wavelet Transformation

Continues wavelet transform (CWT) is one of the most important and powerful tool of signal representation which has been used in different applications such as time-frequency signal processing. The wavelet transform decomposes signals using dilated (i.e. scaled in size) and translated (i.e. shifted in time) functions called mother wavelets, which transform a continuous function into a highly redundant function. A mother wavelet has a mean of zero and sharply decays in an oscillatory way, i.e. it rapidly falls to zero at either side of its central path. CWT of a given signal, *x(t)* with respect to a mother wavelet, *g(t)* is defined as

$$CWT(a,b) = \frac{1}{\sqrt{a}} \int_{-\infty}^{+\infty} x(t) g(\frac{t-b}{a})\, dt \qquad (4.1)$$

where *a* is the dilation or scale factor and *b* is the translation factor or time shift factor, and both variables are continuous.

The original one-dimensional time-domain signal, *x(t)* is mapped to a new two-dimensional function space across scale *a* and translation *b* by the wavelet transform (WT). A WT coefficient *CWT(a,b)* at a particular scale and translation represents how well the original signal, *x(t)* and scaled and translated mother wavelet match. Thus, the set of all wavelet coefficients *CWT(a,b)* associated with a particular signal are the wavelet representation of the original signal, *x(t)* with respect to the mother wavelet, *g(t).*

Discrete wavelet transformation (DWT) is a time-frequency signal analysis tool which has been used in many scientific and engineering fields. DWT uses the wavelet function (φ) and scaling function (ϕ) to perform simultaneously the multi-resolution analysis (MRA) decomposition and reconstruction of the signal. The wavelet function generates the detail information (high-frequency components) of the decomposed signal and the scaling function

generates the approximation information (low-frequency components) of the decomposed signal. Thus, DWT is a well-suited tool for analyzing high-frequency transients in the presence of low-frequency components such as non-stationary and non-periodic wideband signals.

As the main characteristic of DWT is the MRA, it can decompose the original signal into several other signals with different levels (scales) of resolution. From these decomposed signals, the original time-domain signal can be recovered without losing any information. The recursive mathematical representation of the MRA is as [75]

$$V_j = V_{j+1} + W_{j+1} = W_{j+1} + W_{j+2} + \cdots + W_{j+n} + V_n \tag{4.2}$$

where V_{j+1} is the approximation version of the given signal at scale *j+1*. W_{j+1} is the detailed version that displays all transient phenomena of the given signal at scale *j+1* and n is the decomposition level.

As it is noted before, WT function ($\varphi(t)$) serving as a high-pass filter can generate the detail information of the signal, while the scaling function ($\phi(t)$) can generate the approximation information of the distorted signal. In general, the discrete $\varphi(t)$ and $\phi(t)$ are defined as

$$\varphi_{j,n}[t] = 2^{\frac{j}{2}} \sum_n d_{j,n}\, \varphi_{j,n}\left[2^j t - n\right] \tag{4.3}$$

$$\phi_{j,n}[t] = 2^{\frac{j}{2}} \sum_n c_{j,n}\, \phi_{j,n}\left[2^j t - n\right] \tag{4.4}$$

where d_j is the wavelet coefficient at scale j, and c_j is the scaling coefficient at scale j.

The original signal $x_j[t]$ at scale j is sampled at constant time intervals, thus $x_j[t] = (V_0, V_1, \ldots, V_{N-1})$, the sampling number is $N = 2^j$. J is an integer number. DWT mathematical recursive equation (as $V_j = V_{j+1} + W_{j+1}$) is presented as

$$DWT\left(x_j[t]\right) =$$

$$\sum_k x_j[t]\phi_{j,k}[t] = 2^{\frac{j+1}{2}}\left(\sum_n u_{j+1,n}\phi\left[2^{j+1}t - n\right] + \sum_n w_{j+1,n}\varphi\left[2^{j+1}t - n\right]\right), \tag{4.5}$$

$$0 \le n \le \frac{N}{2^j} - 1$$

where

$$u_{j+1,n}[t] = \sum_k c_{j,k}\, u_{j,k+2n}, \text{ for } \quad 0 \le k \le \frac{N}{2^j} - 1 \tag{4.6}$$

$$w_{j+1,n}[t] = \sum_k d_{j,k}\, u_{j,k+2n}, \text{ for } \quad 0 \le k \le \frac{N}{2^j} - 1 \tag{4.7}$$

$$d_k = (-1)^k c_{2p-1-k} \quad p = \frac{N}{2^j} \tag{4.8}$$

where $u_{j+1,\,n}$ is the approximation information at scale $j+1$, $w_{j+1,\,n}$ is the detail information at scale $j+1$. The main idea of DWT analysis is to apply low-pass and high-pass filter sets to the signal at each level of decomposition. The low-pass output (i.e. approximation) becomes the input to the second filter sets while the high-pass output corresponds to the signal details, i.e. the high-frequency information of the signal. Figure 26 illustrates the three levels DWT decomposition algorithm. At each decomposition level, the length of the decomposed signals (e.g. u_1 and w_1) is half of the signals (x_0) in the previous stage.

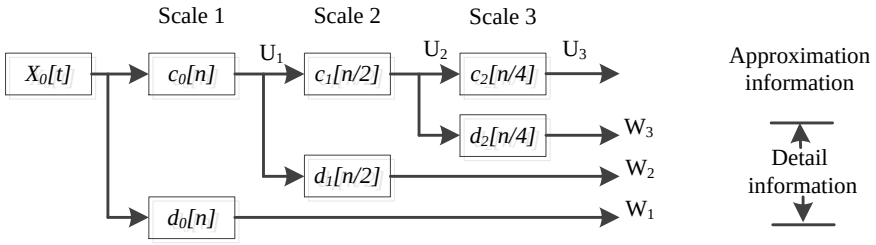

Figure 26. Three levels of DWT decomposition

There are many types of mother wavelets that can be employed in practice. The commonly used mother wavelets are Haar, Symmlet, Daubechies, Morlet as shown in Figure 27. The most widely applied mother wavelets suitable for a wide range of power system applications is the Daubechies wavelet, which is ideally suited for detecting low amplitude, short duration, fast decaying and oscillating type of signals, typical of those encountered in power systems [74].

Figure 28 shows 3-level DWT decomposition with Daubechies-4 (db4) mother wavelet of the measured faulty phase voltage for a fault in a power transmission line. The voltage signal is measured with a sampling frequency of 200 kHz. Thus, the depicted DWT coefficients in details 1, 2 and 3 contain frequency information of [50-100 kHz], [25-50 kHz] and [12.5-25 kHz], respectively. The approximation at level 3 contains fundamental frequency as well as transient information with the frequencies of less than 12.5 kHz.

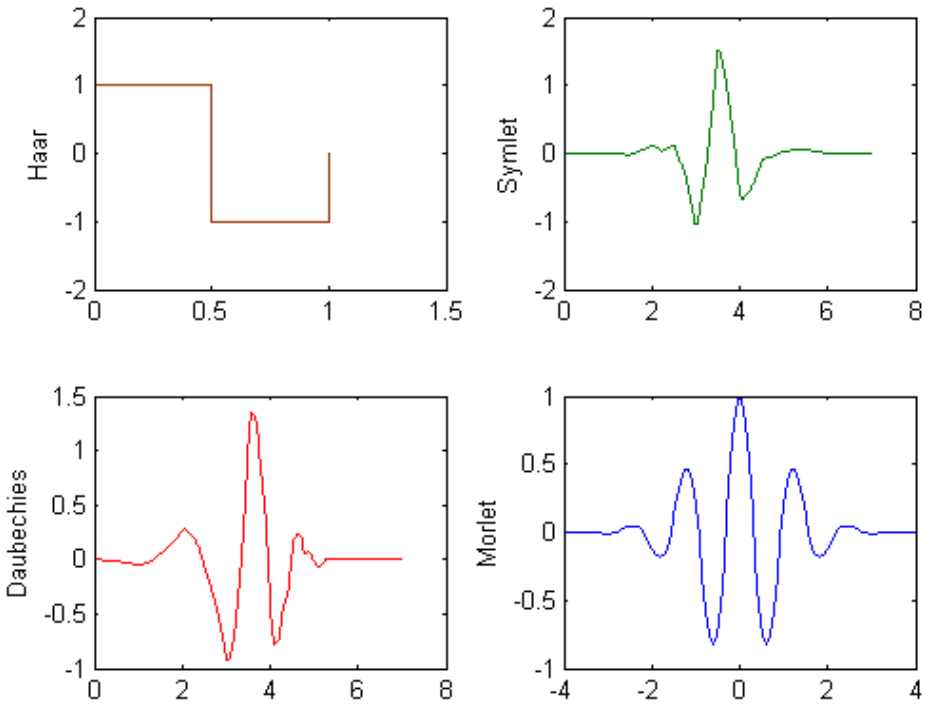

Figure 27. Approximations of commonly used mother wavelets

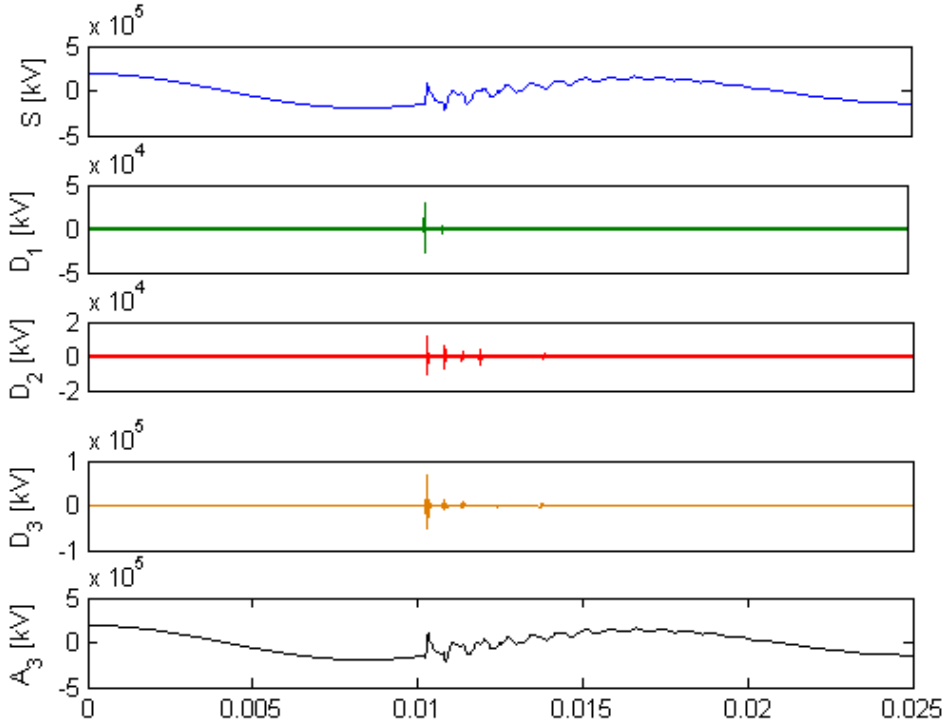

Figure 28. Three-level DWT decomposition of a faulty phase voltage

In the following, the main power system applications of WT will be reviewed briefly.

4.4. Power System Applications of WT

DWT has been utilized in different power system applications in the literature which are categorized as:

- Power quality analysis such as: harmonic analysis, power quality event classification etc.
- Power system protection,
- Power system market analysis: energy price forecasting,
- Fault classification and fault location.

In recent years, concerns over the power quality (PQ) has been increased rapidly, since poor electric power quality causes many problems for the affected loads, such as malfunctions, instabilities and short life time of equipment. In order to improve electric power quality, the sources and causes of such disturbances need to be known before appropriate action can be taken. In 1996, a new approach aims at detecting, localizing, and classifying various types of power quality disturbances is presented in [76]. The approach is based on wavelet transform analysis and the key idea of the approach is to decompose a given disturbance signal into other signals which represent a smoothed version and a detailed version of the original signal. [77] presents a wavelet transform approach using Morlet mother wavelet to supervise power system disturbances. The method is tested to detect various disturbances including voltage sag, voltage swell, momentary interruption and oscillatory transients. It is also tested on the harmonic analysis of the arc furnace from the field test data. [78] presents a method to estimate the harmonic contents of measured voltage and current signals using the wavelet transform. The results are verified by comparing the results with the method proposed in the exiting International Electrotechnical Commission (IEC) standards. [79] deals with the problem of real-time detection and evaluation of different kinds of waveform distortions such as harmonics, interharmonics, as well as transients and notching. The proposed method is a hybrid method

including: Fourier transform and wavelet transform. The proposed method is verified by using the real voltages measurements obtained from a ship and an electric power system.

The performance of digital filters for transmission line distance protection significantly influences the effectiveness of the relaying operation. [80] proposes a wavelet-based algorithm, which can be implemented in microprocessor-based protective relays. Simulation results illustrate the effectiveness of this new algorithm for transmission line distance protection. A novel wavelet-based directional protection scheme is presented in [81]. The initial arrival of the traveling wave and its sign is identified reliably by using wavelet transform. The wavelet-based directional protection scheme solves several problems existing in existing protective relays and is suitable for use as an ultra-high speed UHV/EHV transmission line protective relay. [82] presents a new method for the boundary protection of series-compensated transmission lines, as well as fault classification. The boundary protection is based on detecting distinct frequency bands contained in the transient fault current wave. Discrete wavelet transform is used to capture two bands of frequencies in the transient current signal. Fault classification is done using the discrete wavelet transform. The wavelet coefficients of the three phase and ground currents are obtained and the average coefficient of each current is then utilized to classify the faulty phases. A novel hybrid protection algorithm, based on traveling wave protection principle and boundary protection principle for a monopolar HVDC line is proposed in [83]. Wavelet transform (WT) is used in the traveling wave protection to analyze the dc signal. The boundary protection principle based on WT is used with traveling wave protection to distinguish the internal faults from the external ones.

In a competitive electricity market, accurate energy price forecasting is an important issue for all the market participants either for developing bidding strategies or for making investment decisions. [84] proposes a novel method to forecast day-ahead electricity prices based on the wavelet transform and Autoregressive integrated moving average (ARIMA) models. The historical and price series is decomposed using WT in a set of constitutive series. Then, the future values of these constitutive series are forecasted using fitted ARIMA models. An adaptive wavelet neural network (AWNN) is proposed in [85] for short-term price forecasting (STPF) in electricity markets. A commonly used Mexican hat wavelet is chosen as the mother wavelet for hidden-layer neurons of feed-forward neural network (FFNN). The effectiveness of the proposed

approach is demonstrated for day-ahead forecasting of market clearing price (MCP) in Spain electricity market and locational marginal price (LMP) forecasting in PJM regional transmission organization (RTO) electricity market. [86] presents a novel hybrid intelligent algorithm to forecast day-ahead electricity price in the Ontario electricity market. The method utilizes a data filtering technique based on WT, an optimization technique based on firefly (FF) algorithm, and a soft computing model based on fuzzy ARTMAP (FA) network.

In late 90's, the use of the discrete wavelet transform (DWT) is first proposed to estimate the location of the fault in transmission lines [53]. Traveling wave theory is utilized to capture the travel time of the transient voltage along the line between the fault point and the relay. Wavelet transform is used to obtain the time resolution of high frequency components of the fault voltage transients. The paper proposed two algorithms for fault location: synchronized measurements at both ends of the transmission line, and measurements at one end.

4.5. Overview of Machine Learning Methods for Classification

FT, STFT and WT signal decomposition are used to extract signal characteristics (frequency content or time-frequency information) and are reviewed in the previous sections. The obtained information can be utilized as input to a classification system which would give, for example, the underlying causes of the disturbances, or type of the fault or faulty section in a power grid as output. There are numerous methodologies of machine learning that are potentially very useful for power system disturbance identification and classification. These methods include: learning machines using linear discriminants, probability distribution–based Bayesian classifiers and Neyman–Pearson hypothesis tests, neural networks, support vector machines, and rule-based expert systems [87].

In machine learning algorithms, minimizing the generalization error, which is the error on the test data-set rather than on the training data-set, needs to be considered. Support vector machine (SVM) is an approximate implementation of structural risk minimization such that the generalization error is bounded by the sum of training error and a term that is dependent on the Vapnik–Chervonenkis (VC) dimension [87]. It needs to be noted that neural networks (NN), frequently used in the classification of power system disturbances, are inferior to SVMs. Neural networks are associated with a poor generalization performance for the test data. Since SVM is

designed to minimize the error on the test set with an upper error bound, it is a more advanced algorithm [87].

The fundamentals of support vector machine classifiers are presented briefly in the next section.

4.6. Fundamentals of Support Vector Machine

Support vector machine (SVM) was first introduced by Vapnik as a binary linear classifier [88]. The SVM classification finds an optimal hyperplane to separate data sets with two different classes ($\{+1, -1\}$). The linear hyperplane is defined by a weight vector W and a bias term b as

$$W^T x + b = \begin{cases} \geq 1, & class + 1 \\ \leq -1, & class - 1 \end{cases} \tag{4.9}$$

Figure 29 shows the separating hyperplane in a 2-dimensional space. The separation margin (m) between two classes is given as [88]

$$m = \frac{2}{||W||} \tag{4.10}$$

In order to maximize m, $||W||$ is minimized. Thus the maximum margin, m can be found by solving the following quadratic optimization problem

$$min \frac{1}{2} ||W||^2 \tag{4.11}$$

$$subject\ to \quad y_i(W^T x_i + b) \geq 1 \tag{4.12}$$

where $y_i \in \{+1, -1\}$ is the corresponding label for each x_i.

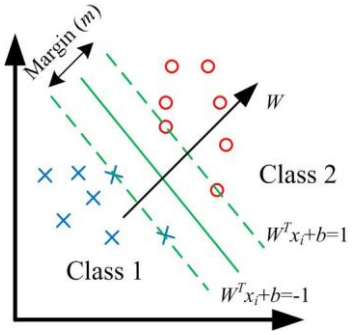

Figure 29. 2-dimensional feature space with the optimal separating hyperplane

The solution to the problem provides the values of W and b such that the separation between the classes is maximum. The SVMs are obtained by solving the dual optimization problem as

$$max\, L(\alpha) = \sum_{i=1}^{N} \alpha_i - 2^{-1} \sum_{i=1}^{N} \sum_{j=1}^{N} \alpha_i \alpha_j y_i y_j x_i x_j \tag{4.13}$$

$$subject\ to \quad \sum_{i=1}^{N} \alpha_i y_i = 0 \tag{4.14}$$

$$\alpha_i \geq 0 \tag{4.15}$$

where α_i is the Lagrangian multiplier and N is the number of training data.

Once the dual optimization problem is solved, the training points with $\alpha_i^* > 0$ are the support vectors (SVs), and then W^* and b^* are calculated as

$$W^* = \sum_{i=1}^{N_{SV}} \alpha_i^* y_i x_i \tag{4.16}$$

$$b^* = \frac{1}{N_{SV}} \left(\sum_{i=1}^{N_{SV}} y_i - W^* x_i \right) \tag{4.17}$$

where N_{SV} is the number of SVs.

However, if the original data in the input space is not linearly separable, it can be mapped into a higher dimensional feature space using non-linear functions Φ to obtain a linearly separable data set. As calculation of inner product of Φ in higher dimensional feature space is computationally complex, kernel function k; is utilized to calculate the inner product directly as a function of the original data in the input space. Thus, the SVMs are obtained by solving the optimization problem as

$$max\, L(\alpha) = \sum_{i=1}^{N} \alpha_i - 2^{-1} \sum_{i=1}^{N} \sum_{j=1}^{N} \alpha_i \alpha_j y_i y_j k(x_i, x_j) \tag{4.18}$$

$$subject\ to \quad \sum_{i=1}^{N} \alpha_i y_i = 0 \tag{4.19}$$

where $k(x_i, x_j)$ is the kernel function.

Thus, the optimization problem is solved and the training points with $\alpha_i^* > 0$ are the SVs. The optimal decision function is then expressed as

$$sign\left(\sum_{i\in SV}\alpha_i^* y_i k(x,x_i)+b^*\right)=\begin{cases}>0, & class+1\\ <0, & class-1\end{cases} \tag{4.20}$$

$$b^*=\frac{1}{N_{SV}}\left(\sum_{i=1}^{N_{SV}} y_i-\sum_{j=1}^{N_{SV}}\alpha_j^* y_j k(x_i,x_j)\right) \tag{4.21}$$

The most commonly used kernel functions such as linear, sigmoidal and Gaussian radial basis function (RBF) are tested for training and evaluating the SVM classifiers in this dissertation and the Gaussian RBF is chosen due to its better performance. The Gaussian RBF kernel function is given as

$$k(x_i,x_j)=\exp(-(\left|\left|x_i-x_j\right|\right|^2)/\gamma) \tag{4.22}$$

where x_i and x_j are n-dimension input vectors. $\gamma=2\sigma^2$, σ is the standard deviation of the Gaussian. The kernel function parameter (γ) is tuned only once in order to achieve sufficient accuracy.

4.7. Power System Applications of SVM

The use of SVM in power system applications has been presented in the literature applying it to different areas, which are categorized as:

- Power quality analysis such as: Disturbance classification,
- Power system protection,
- Voltage and rotor angle stability prediction,
- Energy price forecasting and load forecasting,
- Fault classification and fault location.

Power Quality (PQ) study has become an important issue in recent years due to large applications of power electronic devices. Harmonics, voltage swell, voltage sag, and the power interruption can downgrade the power supply quality. The detection of power disturbances is important to ensure the PQ of supply and to detect the location and the type of disturbances. The authors in [89] propose a new method of PQ classification using SVM and NN. Space phasor is used for feature extraction from three-phase signals to create suitable patterns for classifiers. The

trained classifier is utilized for different disturbance classification including: voltage sags, voltage fluctuations and voltage transients. [90] presents an integrated model for recognizing PQ disturbances using a novel wavelet multiclass support vector machine (WMSVM). The paper combines linear SVMs and the disturbances-versus-normal approach to form the multiclass SVM which is capable of processing multiple classification problems.

Protective relays may mal-operate or the required information may be missed for a proper relay action. Supportive protection systems are required to aid the conventional protection by providing selective and secure coordination. SVMs have considerable potential as zone classifiers for distance relay coordination. This typically requires a multiclass SVM classifier to effectively analyze and to build the underlying concept between reach of different zones and the apparent impedance trajectory during fault. Several methods have been proposed for multiclass classification where typically several binary SVM classifiers are combined together. In [91], one-step multiclass classification, one-against-all, and one-against-one multiclass methods are compared for their performance with respect to accuracy, training, and testing time. [92] proposes a new machine learning approach for protective relays based on binary SVMs, and communications between the protective relays and the supervisory control and data acquisition (SCADA), which is called smart protective relays. The goal of smart relays is to classify and discriminate the normal conditions from fault conditions using local measurements. It is shown that the proposed SVM-based smart relays can detect the location of an initial fault using local current, voltage, real power, and reactive power measurements. Smart relays can make a correct decision even when the state of the system changes after some equipment failure.

Real-time monitoring of power system stability is an essential task to prevent blackouts. In case of a disturbance leading to transient instability, fast recognition of the instability conditions is crucial for allowing sufficient time to take emergency control actions. In [93], a new method for rotor angle stability prediction in a power system immediately after a large disturbance is presented. The proposed two-stage method first estimates the similarity of post-fault voltage trajectories of the generator buses after the disturbance to some pre-identified templates. The stability status prediction is then carried out using SVM classifier which takes the similarity values calculated at the different generator buses as the inputs. In [94], a method based on SVM classifier is presented for rotor angle stability prediction. Generator voltages, frequencies,

measured by phasor measurements units (PMU) immediately after the fault clearance, are used as the inputs for the SVM classifier.

Electricity price forecasting is a difficult and essential task for market participants in a deregulated electricity market. Market participants are sometimes more interested in forecasting the prediction interval of the electricity price, rather than forecasting the value [95]. The prediction interval forecasting is essential to estimate the uncertainty involved in the price. Thus, it is useful to make generation bidding strategies and investment decisions. In [95], a novel data mining-based algorithm is proposed to achieve two major objectives: to accurately forecast the value of the electricity price series, which is widely accepted as a nonlinear time series, and to accurately estimate the prediction interval of the electricity price series. In the proposed method, SVM is used to forecast the value of the price.

Short-term load forecasting (STLF) is the basis for power system planning and operation. Many power system operations such as unit commitment, economic dispatch, maintenance scheduling and planning, is performed effectively with accurate STLF results. The use of SVM for STLF was initially introduced in [96]. Another STFT method, based on an adaptive two-stage hybrid network with self-organized map (SOM) and SVM is presented in [97]. In the first stage, the SOM network is applied to cluster the input data set into several subsets in an unsupervised manner. Then, groups SVMs for the next day's load profile are used to fit the training data of each subset in the second stage.

4.8. Summary

This chapter presents a brief review of Fourier analysis and the relevant limitation. Then an overview of WT fundamentals is given followed by its applications to power system analysis. A brief review of SVM and its applications in power system are presented at the end of this chapter. The next three chapters present the proposed fault location methods for three complex transmission lines which are introduced in chapter I.

*Chapter V: Fault Classification and Location for Three-Terminal Transmission Lines**

5.1. Introduction

Three-terminal transmission lines present challenges for fault location due to lack of synchronized measurements at three buses. The fault location methods for three-terminal circuits are either phasor- or traveling wave-based. When compared to phasor-based methods, traveling wave-based fault locators are more accurate and more reliable especially when MOV-protected series capacitors or mutually coupled line sections exist in the circuits. The proliferation of high-frequency signal recorders without using conventional CTs or CVTs also provides a venue for the implementation of traveling wave-based methods. However, the main challenge in traveling wave-based fault location for three-terminal circuits is due to the superimposed reflections of the fault signal from the T-node and the fault point. This chapter reviews the existing solutions for fault location in three-terminal transmission lines and presents a traveling wave-based method for fault classification and location for three-terminal power transmission systems. In the proposed method, DWT is utilized to extract transient information from the recorded voltages. SVM classifiers are then used to classify the fault type and faulty line/half in the transmission networks. Bewley diagrams are observed for the traveling wave patterns and the wavelet coefficients of the aerial mode voltage are used to locate the fault. ATP software is used for transients simulations. The performance of the method is tested for different fault inception angles (FIA), different fault resistances with satisfactory results. The main contributions of the proposed implemented method are as follows: 1) The proposed method uses SVM for faulty line identification based on the classified fault type and the method does not require synchronized measurements at all terminals. This way the algorithm has the advantageous of using unsynchronized transient voltage measurements from only two terminals. 2) The proposed method uses SVM for faulty half identification. Since the existing traveling wave-based fault location methods use the time delay between the arrival time of the initial traveling waves in

ground mode and aerial mode for faulty half identification, the SVM-based approach makes the algorithm insensitive to the possible errors resulting from calculation of the time delay, especially for the faults close to the middle of the lines. 3) The proposed methodology uses a smaller set of inputs to the SVM classifiers.

5.2. Existing Solutions

A recently proposed phasor-based fault location method for three-terminal systems is presented in [45], where estimation of a distance to fault and indication of a faulty section are performed using three-phase current from all three terminals and additionally three-phase voltage from the terminal at which a fault locator is installed. Authors assume that synchronized measurements are available. Traveling wave- based fault location for three-terminal transmission systems is first proposed in [98]. The cross-correlation between the forward and backward traveling waves and a polarity change criterion is considered to determine the faulty line prior to fault location. The traveling wave-based fault location technique using post-fault currents at three terminals is proposed in [52]. Use of DWT for fault location in transmission systems is first proposed in [53] followed by a single ended traveling wave-based procedure for three-terminal systems developed in [54]. The wavelet transformation is applied to the modal voltages at all three terminals to determine the faulty line. In [99] a wavelet-based fault location for three-terminal transmission system is proposed. Wavelet transform is applied to the synchronized transient voltages from all three buses to detect the arrival time of the first traveling waves. The traveling arrival times are then used for faulty line identification and fault location. In [100], combined impedance- and traveling wave-based fault location method is proposed for multi-terminal transmission systems. The impedance-based fault location is first utilized to identify the faulty line and the faulty half of the line. The arrival times of traveling waves are then detected using DWT which are used for fault location. [101] and [102] propose the use of DWT and SVM for fault classification and fault location in the three-terminal transmission lines for the first time.

5.3. Proposed Method for Fault Classification

In this section, the traveling wave-based fault type classification method in three-terminal transmission systems using DWT and SVM is presented.

Fault type classification is performed using four binary support vector machines, SVM_i (i = 1,...,4). The SVMs are trained to identify the faulty phase. SVM_1 is trained to detect the fault at phase *a* while SVM_2 is trained to detect the fault at phase *b* and SVM_3 is trained to detect the fault at phase *c*. SVM_4 is trained to detect whether the fault is grounded or not. The output of each SVM_i (i = 1,..,4) is either +1 or -1. For example if SVM_1 and SVM_4 are +1 while the other SVMs are -1, it is implied that the fault is grounded at phase *a* .

First, the SVM classifiers need to be trained using different fault scenarios in a given topology. Then, the performance of the SVM classifiers is evaluated using other fault scenarios. Normalized wavelet energies of post-fault three-phase and ground mode transient voltages are used as the input to the binary SVM classifiers. The SVM classification is tested using three different wavelets: Daubechies-4 (db-4), db-8 and Meyer. The classification accuracy for three wavelets remains the same and db-4 is utilized as the mother wavelet as it is one of the widely adopted wavelets in the literature. The algorithm to obtain the input features of the SVMs is provided as follows:

1. Clarke's modal transformation for transposed lines is applied to three-phase voltages to obtain aerial and ground mode voltages. In the case of untransposed lines, the modal transformation matrix obtained by ATP software can be used.
2. DWT is applied once to the recorded three-phase voltages (V_a, V_b, V_c) and ground-mode voltage (V_0) for 40 *ms* to obtain the wavelet transformation coefficients (*WTC*s) in scale-2. The selection of scale-2 over scale-1 is due to better performance for the investigated systems in this study. *WTCs* are then squared to clearly identify the arrival instants and denoted as WTC^2s.
3. The wavelet energies of voltages, E_{Vk} ($k \in \{a,b,c \text{ and } 0\}$) are calculated by summation of WTC^2s over one cycle after the fault is detected

$$E_{Vk} = \sum_{m=0}^{M-1} WTC_k^2(m), \text{ for } k \in \{a,b,c \text{ and } 0\} \quad (5.1)$$

where *M* is the number of samples in one cycle.

4. The voltage wavelet energies are normalized

$$E_{N_{Vk}} = \frac{E_{Vk}}{E_{Va}+E_{Vb}+E_{Vc}+E_{V0}}, \text{ for } k \in \{a,b,c \text{ and } 0\} \quad (5.2)$$

The training step for the classifiers is carried out to obtain the optimum decision functions. The input features, $E_{N_{Vk}}$ are calculated by using transient voltages from two buses. Thus, the processed values are stored in an $N\times 8$ training matrix where each column represents one feature and each row represents one training sample. N is the total number of different fault scenarios with different locations, types, FIAs, loadings and fault resistances. The flowchart of the algorithm is provided in Figure 30.

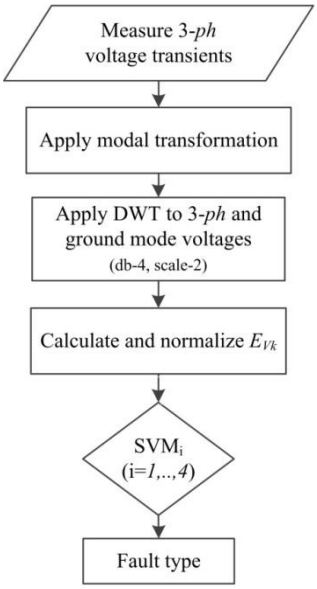

Figure 30. Fault classification flowchart

SVM classifiers are trained using the training matrix corresponding to an 8-dimensional feature space. Once the training process is completed and the optimal decision function for the two-class separation is known for each phase, the SVMs are ready to classify new incoming data set.

5.4. Proposed Method for Fault Location

This section describes the proposed method for fault location using SVM classifiers and DWT for a three-terminal transmission system in Figure 31. Once, the fault type is classified,

the faulty line is identified using two SVM classifiers. Then, corresponding SVM faulty half identifier is used to identify the faulty half. Aerial mode WTC^2s in scale-2 are finally observed based on the Bewley diagram of the fault initiated traveling waves to identify the traveling wave arrival instants which corresponds to the peaks of WTC^2s. The arrival time differences between consecutive waves are used in fault location procedure. The fault location is developed based on the following assumptions:

- Only two terminal measurements are available,
- The measurements are not synchronized, and
- The measurements are obtained through transient voltage recorders instead of conventional CVTs.

The proposed fault location procedure consists of two steps. First, two different SVMs are used for faulty line identification. In order to detect the faulty line, two binary SVMs (SVM_n, n = 1, 2) are trained. SVM_1 is trained to detect the fault in line A-T and SVM_2 is trained to detect the fault in line B-T. The algorithm identifies the fault in line C-T, if the outputs of two SVMs are -1 at the same time.

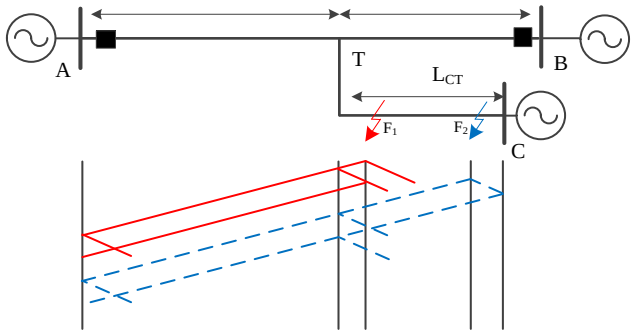

Figure 31. Three-terminal (teed) transmission system

Different SVMs are developed for different fault types. E_{NVk} of voltages at buses A and B are used as the inputs to both SVM faulty line classifiers. Once the faulty line is identified, faulty half is determined by using another SVM which is trained by using E_{NVk} at bus A for a fault in line A-T, at bus B for a fault in line B-T and at buses A and B for a fault in line C-T.

For the faults in line A-T or B-T, the faulty half is first identified using the corresponding SVMs and fault location equations developed in are then used. In the case of a fault in line C-T,

if the fault is in the first half of the line (F_1 in Figure 31), the distance of the fault to bus A is calculated as

$$x = L_{AT} + \frac{v_1^{line}\Delta t}{2} \tag{5.3}$$

where Δt [s] is the time difference between the first and the second peaks of WTC^2s at bus A corresponding to the backward traveling wave and the reflected backward traveling wave from the fault point, respectively v_1^{line} [mi/s] is the traveling wave velocity on line C-T calculated at the frequency corresponding to the middle value of scale-2 (i.e 37.5 kHz). If the fault is in the second half (F_2), the following equation is used to determine the fault location with respect to bus A

$$x = L_{AT} + L_{CT} - \frac{v_1^{line}\Delta t}{2} \tag{5.4}$$

where Δt [s] is the time difference between the first and the second peaks of WTC^2s at bus A corresponding to the backward traveling wave and the reflected forward traveling wave from the bus C, respectively. The steps of fault location in three-terminal circuit are summarized as follows:

1. Fault type is determined by using fault-classifier SVMs.
2. The corresponding line-identifier SVMs (for specific fault type) are used to determine the faulty line.
3. The corresponding half-identifier SVM is used to determine the faulty half in the line.
4. Fault location is performed using Bewley diagram.

The simulation results of the fault classification and location algorithms are presented in the next section.

5.5. Simulation Results

The performance of the proposed fault classification and location method is evaluated on a 230-kV, 60-Hz three-terminal transmission system. Line lengths are assumed to be $L_{A\text{-}T}$ = 200 miles, $L_{B\text{-}T}$ = 180 miles and $L_{C\text{-}T}$ = 170 miles. Transient simulations are carried out using ATP

software. Overhead lines are modeled as frequency-dependent using the data provided in Appendix A. The sampling time interval of voltage measurement is 5 μs (sampling frequency, f_s = 200 *kHz*). The traveling wave velocities calculated using ATP software at 37.5 kHz in aerial and ground mode are 1.85×10^5 and 1.78×10^5 *mi/s*, respectively. MATLAB Wavelet Toolbox and SVM Toolbox are used to implement the proposed method.

Gaussian RBF is considered for training and testing the SVM classifiers. The kernel function parameter (γ) is tuned to achieve sufficient accuracy for each SVM. The tuning is carried out by changing the values of γ from 0.1 to 10 in steps of 0.1. The tuned parameters for different classifiers are provided accordingly. The results for transposed lines are provided; however the proposed method is also tested on untransposed lines with satisfactory results which are not provided due to space limitations. Gaussian noise is added to the measured voltages in all simulations in order to take the impacts of random error into account. The noise is selected to have a zero mean and a standard deviation (σ) equal to 1% of the sampled measurements. Different fault scenarios under various system conditions (δ – loading, *FIA*, R_f and location of the fault) are simulated to evaluate the performance of the proposed method. The simulations are carried out for the following cases:

1) δ_B = 5˚, 7° and 10˚, δ_C = 7˚, 10° and 13˚,
2) *FIA* = 10˚, 45˚, 80˚ and 120˚,
3) R_f = 0.1 Ω, 1 Ω and 100 Ω,
4) L_f = 10%,…, 90% of the lines length.

The simulations are carried out for the above listed conditions and 13,824 different cases are generated. The data sets corresponding to all fault conditions at load angles δ_B = 5° and δ_C = 7° are used for training the SVM classifiers. The classifiers are then tested using the data sets corresponding to all fault conditions at load angles δ_B = 7°, 10° and δ_C = 10°, 13°. Subsequently, other fault scenarios with different fault conditions (R_f and *FIA*) corresponding to the intermediate fault locations in the training set (e.g. Fault occurring at δ_B = 7°, δ_C = 10°, *FIA* = 120˚, R_f = 1 Ω, L_f = 35%) are also tested. The accuracy of the fault classification algorithm is calculated as

$$\eta = \frac{\#\ of\ accurately\ classified\ fault\ types}{\#\ of\ test\ cases} 100 \tag{5.5}$$

According to the fault classification results, a 96.3% accuracy is obtained for classifying the faults including phase *a* using $SVM_1(\gamma = 0.9)$ while a 96.2% accuracy is achieved for classifying the faults including phase *b* using $SVM_2(\gamma = 1.1)$ and 97.5% accuracy is achieved for the faults including phase *c* using $SVM_3(\gamma = 1.1)$. The grounded faults are identified with a 100% accuracy using $SVM_4(\gamma = 1.5)$. The classification accuracy deteriorates during extreme cases when a high-resistance fault (i.e. $10\ \Omega \leq R_f \leq 100\ \Omega$) occurs at small fault inception angles (i.e. $\leq 10°$). This rare phenomenon results in in small wavelet coefficients subsequently resulting in low signal energies making it difficult for SVMs to classify the faults. Note that the final accuracy of the fault type classification is 90.3%, which is obtained by multiplying the accuracies of four SVMs.

Once the fault type is classified, the faulty line is identified. For each fault type, different trained SVMs are utilized to identify the faulty line. Two SVMs are used to identify the faulty line. The accuracies of faulty line identification for different fault types are given in Table 3. The tuned parameters for the two SVM faulty line identifiers are provided for each fault type as γ_1 and γ_2, corresponding to line A-T and B-T, respectively.

Once the faulty line is identified, then the faulty half of the line is determined using the SVM corresponding to the line. A 98.8% accuracy is achieved for the faulty half identifier SVM ($\gamma = 1.3$) for faults in line C-T, while a 99.1% accuracy is achieved for the SVM ($\gamma = 1.1$) for faults in line A-T and 98.2% accuracy for the SVM ($\gamma = 1.5$) for faults in line B-T. The possible conflicts of two line-identifier SVMs for A-T and B-T are handled by comparing the value of the decision functions obtained by (10). For example, if both SVMs for A-T and B-T give +1 as the output, the one which has the largest value for decision function, $f(x)$ is superior to the other one and the corresponding line is identified as the faulty one.

Following, the results of two scenarios are provided. First scenario assumes that a phase *a*-to-ground fault occurs in line C-T at 235 miles from bus A (i.e. 35 miles from the T-point), The fault conditions are $\delta_B = 3°$, $\delta_C = 8°$, $FIA = 310^{\circ}$, $R_f = 0.2\ \Omega$. The fault type is classified accurately since SVM_1 (corresponding to phase *a*) and SVM_4 (corresponding to *ground*) outputs are +1 while the other SVMs are -1. The two faulty line identifier SVMs (for phase *a* to ground

fault) are -1, and thus the faulty line is identified as C-T. The SVM for faulty half identification gives the output as +1 implying that the fault is in the first half. Once the faulty half is identified, DWT is applied to the aerial mode (mode 1) voltage at scale-2 at bus A. Figure 32 shows the voltage WTC^2s. The time difference between the first and the second traveling waves peaks in WTC^2s, Δt is observed as 380 μs. The fault location is then calculated

$$x = 200 + \frac{38 \times 10^{-5} \times 1.85 \times 10^5}{2} = 235.15\ mi$$

Second scenario assumes that an *a*-*b*-to-ground fault occurs in line C-T at 347 miles from bus A with the conditions as $\delta_B = 5°$, $\delta_C = 9°$, $FIA = 30^{\circ}$, $R_f = 0.3\ \Omega$. The SVM classifiers accurately determine the type of the fault, since SVM_1, SVM_2 and SVM_4 outputs are +1 while the SVM_3 is -1. The two faulty line identifier SVMs (for *a*-*b*-to-ground fault) are -1, and thus the faulty line is identified as C-T. The SVM for faulty half identification gives the output as -1 implying that the fault is in the second half. Voltage WTC^2s in aerial mode at scale-2 at bus A is shown in Figure 33. Δt is observed as 250 μs. The fault location is then calculated

$$x = 200 + 170 - \frac{25 \times 10^{-5} \times 1.85 \times 10^5}{2} = 346.88\ mi$$

As the common practice, the absolute error is calculated as a percentage of the total section length in order to evaluate the performance of the proposed fault location method

$$Error\ (\%) = \frac{AFD - CFD}{Total\ Section\ Length} 100 \qquad (5.6)$$

where *AFD* is the actual fault distance and *CFD* is the calculated fault distance.

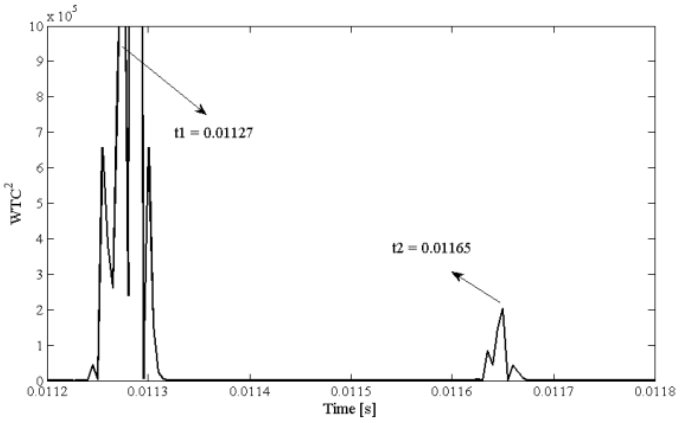

Figure 32. Voltage WTC^2s in aerial mode in scale-2 for a single-phase-to-ground fault in line C-T at 235 miles from bus A

Table 3. Faulty line identification accuracy for different fault types

Fault Type	Accuracy (%)
AG (γ_1=0.9, γ_2=1.2)	95.2
BG (γ_1=0.8, γ_2=1.1)	95.4
CG (γ_1=0.9, γ_2=1)	95.3
AB (γ_1=1.1, γ_2=1)	99.3
AC (γ_1=0.9, γ_2=0.9)	99.3
BC (γ_1=0.9, γ_2=1.1)	99.3
ABG (γ_1=1, γ_2=1.1)	96.3
ACG (γ_1=0.9, γ_2=0.9)	96.1
BCG (γ_1=1, γ_2=0.9)	98.1
ABC/ABCG (γ_1=1, γ_2=1.1)	99.7

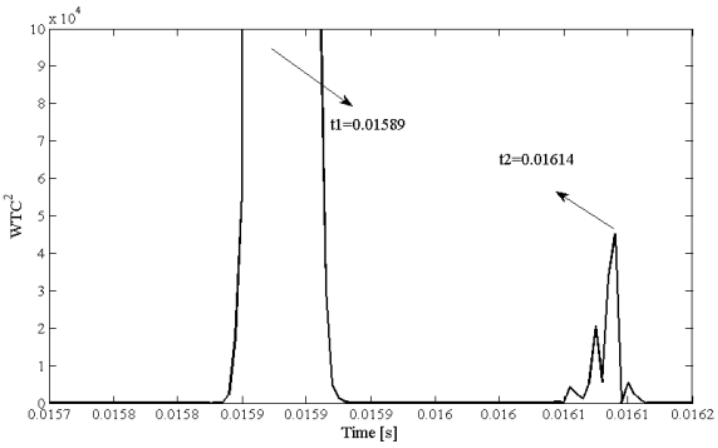

Figure 33. Voltage WTC^2s in aerial mode in scale-2 for a single-phase-to-ground fault in line C-T at 347 miles from bus A

Different cases of single phase-to-ground faults with 0.5 Ω fault resistance are considered. The results are presented in Table 4.

For the faults in line C-T, the fault locations are calculated using the aerial mode voltage WTC^2s at bus A and the distances are represented with respect to T-point. The calculated fault locations show good correlation with the actual fault locations.

5.6. The Effect of Fault Inception Angle

The impact of the fault inception angle on the proposed method is evaluated in this section. Although different fault inception angles affect the severity of the fault initiated traveling waves, the proposed method uses the normalized wavelet energies, $E_{N_{Vk}}$ as the input to the SVM classifiers. The results for four different faults with respect to the changes in *FIA* are shown in Table 5 and 6. As expected, the results show that the fault classification and faulty line identification methods give accurate results for a wide range of fault inception angles varying between 5º and 350º. The method has satisfactory performance for locating the faults occurring under different fault inception angles as demonstrated in Table 6.

The sensitivities of faulty line/half identification procedures to small fault inception angles and high-resistance faults are further investigated. Our investigations show that the misclassification zone around the middle point of the line CT is 3 miles for extreme cases such

as high-resistance (i.e. $R_f \geq 10\ \Omega$) faults or faults occurring at small fault inception angles (i.e. $FIA \leq 5^{\circ}$). The misclassification zone around the tap point is 2 miles for such cases.

5.7. The Effect of Fault Resistance

Simulations are carried out for a wide range of fault resistances to evaluate the performance of the proposed method. In high impedance faults (HIFs), the phases and ground mode WTC^2s peaks are smaller than low impedance faults which result in smaller wavelet energies. However, as mentioned before the use of $E_{N_{Vk}}$ for fault type classification and faulty line/section identification makes the method robust to different fault resistances. The performance of the algorithm for fault classification and faulty line identification is tested for a range of fault resistance values from 0.01 to 90 Ω.

The fault type classification and faulty line identification results for three fault resistances are shown in Table 7 and 8 for three fault locations. As expected, the calculated fault distances and the corresponding errors do not change with the fault resistance. The results show that the performance of the proposed method is insensitive to the fault resistance.

Table 4. Fault location error analysis for different case

Fault Section	Actual fault distance,	Calculated fault distance, CFD	Error, *e*(%)
$L_{A\text{-}T}$	4	3.70	0.15
	17	16.65	0.17
	91	90.65	0.17
	193	192.61	0.20
$L_{B\text{-}T}$	7	7.41	0.22
	18	18.51	0.27
	85	85.11	0.05
	177	176.30	0.38
$L_{C\text{-}T}$	8	8.33	0.19
	27	26.83	0.11
	82	81.60	0.35
	161	160.75	0.14

Table 5. Fault type classification output for different *FIA*

Fault	FIA (°)	a	b	c	g
AG at 35th mi of L_{A-T}, δ_B= 8°, δ_C = 11°, R_f = 0.5 Ω	30	**1**	-1	-1	**1**
	150	**1**	-1	-1	**1**
	330	**1**	-1	-1	**1**
BC at 67th mi of L_{B-T}, δ_B = 8°, δ_C = 11°, R_f = 0.5 Ω	45	-1	**1**	**1**	-1
	170	-1	**1**	**1**	-1
	350	-1	**1**	**1**	-1
CG at 153rd mi of L_{C-T}, δ_B= 8°, δ_C = 11°, R_f = 0.5 Ω	55	-1	-1	**1**	**1**
	110	-1	-1	**1**	**1**
	300	-1	-1	**1**	**1**
ACG at 4th mi of L_{A-T}, δ_B = 8°, δ_C = 11°, R_f = 0.5 Ω	5	**1**	-1	**1**	**1**
	60	**1**	-1	**1**	**1**
	250	**1**	-1	**1**	**1**

Table 6. Faulty line identification and fault location for different *FIA*

Fault	FIA (°)	L_{A-T}	L_{B-T}	L_{C-T}	CFD (mi)	*e* (%)
AG at 35th mi of L_{A-T}, δ_B = 8°, δ_C = 11°, R_f = 0.5 Ω	30	**1**	-1	-1	35.15	0.07
	150	**1**	-1	-1		
	330	**1**	-1	-1		
BC at 67th mi of L_{B-T}, δ_B = 8°, δ_C = 11°, R_f = 0.5 Ω	45	-1	**1**	-1	66.61	0.20
	170	-1	**1**	-1		
	350	-1	**1**	-1		
CG at 153rd mi of L_{C-T}, δ_B = 8°, δ_C = 11°, R_f = 0.5 Ω	55	-1	-1	**1**	153.35	0.38
	110	-1	-1	**1**		
	300	-1	-1	**1**		
ACG at 4th mi of L_{A-T}, δ_B = 8°, δ_C = 11°, R_f = 0.5 Ω	5	**1**	-1	-1	4.44	0.22
	60	**1**	-1	-1		
	250	**1**	-1	-1		

Table 7. Fault type classification output with different resistance

Fault	R_f (Ω)	a	b	c	g
BG at 185th mi of L_{A-T}, δ_B = 6°, δ_C = 12°, FIA = 35°	0.01	-1	**1**	-1	**1**
	5	-1	**1**	-1	**1**
	70	-1	**1**	-1	**1**
ACG at 125th mi of L_{B-T}, δ_B = 6°, δ_C = 12°, FIA = 35°	0.05	**1**	-1	**1**	**1**
	10	**1**	-1	**1**	**1**
	90	**1**	-1	**1**	**1**
AB at 147th mi of L_{C-T}, δ_B = 6°, δ_C = 12°, FIA = 35°	0.5	**1**	**1**	-1	-1
	1.5	**1**	**1**	-1	-1
	25	**1**	**1**	-1	-1

Table 8. Faulty line identification and fault location for different fault resistance

Fault	R_f (Ω)	$L_{A\text{-}T}$	$L_{B\text{-}T}$	$L_{C\text{-}T}$	CFD (mi)	*e* (%)
BG at 185th mi of $L_{A\text{-}T}$, $\delta_B = 6°$, $\delta_C = 12°$, FIA = 35°	0.01	**1**	-1	-1	185.21	0.11
	5	**1**	-1	-1		
	70	**1**	-1	-1		
ACG at 125th mi of $L_{B\text{-}T}$, $\delta_B = 6°$, $\delta_C = 12°$, FIA = 35°	0.05	-1	**1**	-1	125.65	0.19
	10	-1	**1**	-1		
	90	-1	**1**	-1		
AB at 147th mi of $L_{C\text{-}T}$, $\delta_B = 6°$, $\delta_C = 12°$, FIA = 35°	0.5	-1	-1	**1**	146.87	0.07
	1.5	-1	-1	**1**		
	25	-1	-1	**1**		

5.8. The Effect of Non-Linear High Impedance Fault

A dynamic time-varying resistance model is used to evaluate the performance of the proposed method with non-linear high impedance fault (NLHIF) [103]

$$R_{arc} = \frac{1}{g} \tag{5.7}$$

$$\frac{dg}{dt} = \frac{1}{\tau}(G - g) \tag{5.8}$$

$$G = \frac{|i_{arc}|}{V_{st}} \tag{5.9}$$

where R_{arc} [Ω] is the arc resistance which varies with time, g is the time varying arc conductance, i_{arc} [kA] is the arc current, G is the stationary arc conductance, V_{st} [kV] is the stationary arc voltage and τ is the arc time constant. The stationary arc voltage is estimated as

$$V_{st} = (u_0 + r|i_{arc}|)l \tag{5.10}$$

where u_0 [V/cm] is the constant voltage parameter per arc length, r [mΩ/cm] is the resistive component per arc length and l [cm] is the arc length. The following parameters are used to simulate the fault [103] ; $u_0 = 9.6$, $r = 1.6$, $l = 350$ and $\tau = 1$ ms.

A single-phase-to-ground NLHIF is assumed to be located at 10 mile in line C-T from the T-point (i.e. 210 miles from bus A). The method classifies the fault type according to the outputs of 4 SVM fault type classifiers. The faulty line SVMs identifies the faulty line as the line C-T according to the outputs of SVM classifiers. The SVM for half side identifier in line C-T gives the output as +1. Thus the fault section is determined in the first half of the line. Voltage WTC^2s at bus A in aerial mode at scale-2 are finally used to calculate the fault location by using (5.3)

$$x = 200 + \frac{11 \times 10^{-5} \times 1.85 \times 10^{5}}{2} = 210.18\, mi$$

NLHIF has impact on the magnitude of the traveling waves and it delays the arrival of the traveling waves due to its impact on reflection and refraction coefficients. However, the time difference between the first and the second traveling wave arrivals are not affected. The delay for the simulated fault is observed to be 320 μs with respect to a resistive fault. Thus, the calculated fault location has a good correlation with the actual fault location.

5.9. The Effect of Non-Typical Fault

Finally, the performance of the proposed fault location method is evaluated for a non-typical short-circuit fault. The 0.1 Ω resistance is connected through a 1-Ω inductance to the ground. A Single-phase-to-ground fault is located at 140 miles in line C-T from the T-point (i.e. 340 miles from bus A). The method first classifies the fault type as phase-*a*-to-ground fault according to the output of the SVMs fault type classifiers. The faulty line identification is then performed according to the classified fault. The SVM for half side identifier in line C-T gives the output -1. Thus the fault section is estimated in the second half of the line. The voltage WTC^2s at bus A in aerial mode at scale-2 are used and Δt is observed as 330 μs. Thus, the fault location is calculated using (5.4)

$$x = 200 + 170 - \frac{33 \times 10^{-5} \times 1.85 \times 10^{5}}{2} = 339.47\, mi$$

Even though the magnitudes of the traveling waves decrease as in the case of high-impedance faults, the time difference between the first two arriving waves remain unchanged. It can be concluded that the proposed method is insensitive to non-typical faults.

5.10. Discussion

In this section, the performance of the proposed method for faulty half identification is compared with an existing traveling wave-based method. The existing wavelet-based traveling wave methods use the time delay between the first traveling wave arrival in the ground and aerial mode WTC^2s, Δt_0, for faulty half identification. The fault is identified in the first half, if the Δt_0 is less than the pre-calculated time delay for a fault located in the middle, Δt_m.

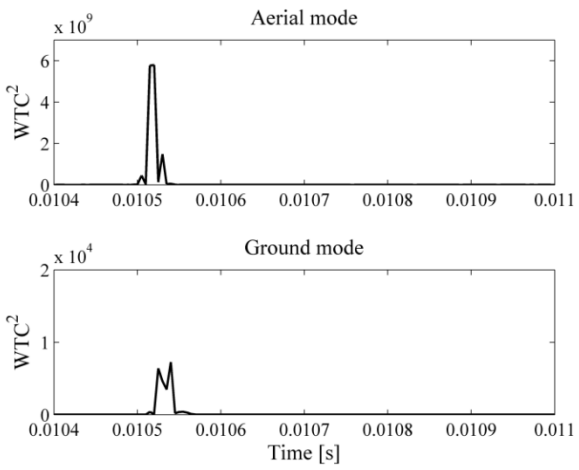

Figure 34. Voltage WTC^2s at bus A in aerial and ground mode in scale-2 for a phase-*a*-*c*-ground fault at 95 miles away from bus A in line A-T

For comparison, a phase *a*-*c*-to-ground fault is considered in line A-T located at 95 miles from bus A. Figure 34 shows the voltage WTC^2s at bus A in aerial and ground mode at scale-2. The time delay for a fault in the middle of line A-T (i.e. 100 mi) calculated using the traveling wave velocities in aerial and ground mode is Δt_m = 21.3 μs. In this example Δt_0 is calculated as 20 μs, identifying the faulty half accurately; however, very high precision is needed for comparison of Δt_m and Δt_0. It is also a challenging task to accurately calculate Δt_0 as Figure 34 demonstrates the proximity of the peak instants.

The proposed method in this dissertation calculates the normalized wavelet energies, $E_{N_{Vk}}$ and uses them as the input to the fault type classifier SVMs resulting in +1 output for SVM_1, SVM_3 and SVM_4 while the output of SVM_2 is -1. Thus, the faulty line identifier SVMs corresponding to fault *a*-*c*-to-ground are used. The SVMs outputs for faulty line identification gives +1 for line A-T and -1 for line B-T and the half-identifier SVM for line A-T corresponding to the classified fault type is further utilized to determine the faulty half. Finally the faulty half is identified as first-half of line A-T since the output of the SVM corresponding to this line is +1 indicating the first half. The proposed method overcomes the precision problem pertinent to existing traveling wave methods using wavelet transform.

5.11. Summary

In this chapter, a traveling wave-based fault classification and location method for three-terminal transmission systems is proposed. DWT is applied to the three-phase and ground mode voltages at two terminals to obtain the normalized wavelet energies. These are later used as the input to the SVM classifiers for fault classification and faulty line/half identification. Once the fault is classified, faulty line and faulty half are identified, the wavelet coefficients of aerial mode voltages are used to locate the fault. The performance of the proposed method is tested for various fault scenarios including different fault resistances, fault inception angles, fault locations, loading levels, non-linear high-impedance and non-typical faults with satisfactory results.

*Chapter VI: Fault Location for Hybrid HVAC Transmission Lines**

6.1. Introduction

The proliferation of underground cables combined with overhead transmission lines (hybrid transmission) in medium- and high-voltage will increase in the future grid. "Hybrid transmission" systems are preferred when right-of-way related issues arise and they offer better reliability. In addition, underground cables are also used to connect off-shore wind farms to the existing grid through overhead lines. However, the complexity of fault location problem increases with the proliferation of such an unusual topology. This chapter first reviews the existing methods for fault location in underground cable and hybrid transmission lines. Then a single-ended traveling wave-based fault location method for a hybrid transmission line is presented. DWT is used to extract transient information from the measured voltages. SVM classifiers are utilized to identify the faulty section and faulty half. Bewley diagrams are observed for the traveling wave patterns and the wavelet coefficients of the aerial mode voltage are used to locate the fault. The transient simulation for different fault types and locations are obtained by ATP using frequency-dependent line and cable models. MATLAB is used to process the simulated transients and apply the proposed method. The main contributions of this section are as follows:

- The proposed method uses SVM for faulty section identification, which is independent of fault type.
- The faulty half identification is improved by utilization of SVM instead of the time-delay between the arrival time of the initial traveling waves in ground mode and aerial mode.
- The SVM classifiers use a smaller set of inputs for decision making.

* Reprinted with permission from "A machine learning and wavelet-based fault location method for hybrid transmission lines," by H. Livani and C. Y. Evrenosoglu, 2014. *IEEE Trans. Smart Grid*, vol. 5. no. 1, pp. 51-59, Copyright 2014 IEEE.

6.2. Existing Solutions

The single-ended fault location in underground cable using steady-state post-fault phasor voltage and current measurements are proposed in [104] and [105]. The faulted underground cable is modeled using the distributed line model. Offline traveling wave-based fault location methods for underground cables are proposed in [106] and [107] where the traveling waves are generated by applying an external excitation voltage. A real-time single-ended traveling wave-based fault location for underground cable is proposed and implemented in [108]. Voltage and current transients are recorded by 200-MHz optic measurements. In [109] a two-ended traveling wave-based fault location using current transients recorded by optic CTs is implemented. In [58] and [110], two-ended traveling wave-based fault locations are proposed for underground cables. The time delay between arrivals of traveling waves at both ends is used to calculate the fault location. In [111] and [112] phasor-based fault location methods for hybrid transmission line consisting of an overhead line and an underground cable is proposed. The proposed methods utilize the synchronized voltage and current measurements from both ends of the transmission line. In [66] an adaptive neural network-fuzzy approach is used to locate the fault accurately in a combined transmission line using fundamental components of post-fault measured voltages. In [113] a single-ended traveling wave fault location method using discrete and continuous wavelet transformation is implemented. The current transients are recorded by using 1.25 MHz optical current transducers. [114] presents a wavelet-fuzzy fault location method for transmission lines. DWT is applied to the current transients and the current wavelet energies are used as the input to the fuzzy fault location algorithm. In [115], a two-ended fault location method using the DWT coefficients at 97 – 195 Hz frequency band of three-phase current transients is proposed. The algorithm is dependent on the fault type. Cubical interpolation is finally utilized to determine the exact fault location. [116] presents a wavelet and neuro-fuzzy based fault location method. Voltage and current DWT coefficients are used as the input for faulty section identification. The impedance-based fault location method is then utilized which is dependent on fault type. In [117], a single-ended traveling wave-based fault location method for combined transmission lines is proposed. The voltage traveling wave's polarity change is used to identify the faulty section. The time delay between traveling waves is then used to calculate fault location. [118] presents a traveling wave-based fault location methods for underground cables using DWT. DWT is used to cancel the noise and detect the arrival instant of waves observing the correlation

between wavelet scales. In [119], a combined wavelet-neural network based fault classification and location is proposed. The authors use scale-3 wavelet coefficients of voltages and fast Fourier transform of reconstructed voltage signal at the same scale to train the neural network. [60] proposes a single-ended traveling wave-based fault location for the hybrid transmission lines for the first time. [120] and [121] extends the primary algorithm to include SVM for faulty section identification.

6.3. Proposed Method for Fault Location

This section describes the proposed single-ended traveling wave-based fault location method for a hybrid transmission line including an overhead line combined with an underground cable. The one-line diagram of the transmission line is shown in Figure 35, where L_L is the length of the overhead line, L_C is the length of the underground cable and M is the measurement location.

The fault location is developed based on the following assumptions:

- Measurements at the sending end of overhead line are available.
- The measurements are obtained through optic voltage and current recorders instead of conventional CVTs and CTs.
- Measurement devices are not available at the joint point.
- Generation and load are not present at the joint point.

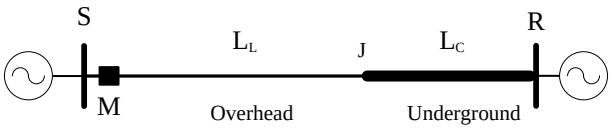

Figure 35. A 230-kV transmission line including an overhead line combined with an underground cable

The proposed fault location method is summarized as follows:

1. The faulty section (i.e. line or cable) is identified using a binary SVM classier.
2. The faulty half is identified by using another binary SVM corresponding to the faulty section.
3. The Bewley diagram of the fault-initiated traveling waves is used for fault location.

Note that each topology (different tower configuration, different phase configuration, different conductor, different line/cable length etc.) requires a different training of support vector machines. The three steps outlined above are described in the following subsections.

6.3.1. SVM Faulty Section Identification

Faulty section identification is performed using a binary support vector machine, SVM_1. The SVM_1 output implies whether the fault is in the overhead line (+1) or in the underground cable (-1). The SVM_1 classifier needs to be trained using different fault scenarios in a given topology. The performance of the SVM_1 classifier is then evaluated using other fault scenarios.

The magnitude of voltage and current transients change with respect to fault location, fault inception angle (*FIA*) and fault resistances subsequently affecting the calculated voltage wavelet energies and current energies. Normalized wavelet energies of three-phase and ground mode transient voltages and normalized energies of three-phase and ground mode transients currents are used as input to the binary SVM classifiers. Normalization prevents having large weight vectors and over-fitting for the SVMs. The classification is tested using three different wavelets: Daubechies-4 (db-4), db-8 and Meyer. The classification accuracy for three wavelets remains the same and db-4 is utilized as the mother wavelet. The input feature extraction steps for the SVM classifiers are provided as follows:

1. Clarke's modal transformation for transposed lines is applied to three-phase voltages to obtain aerial and ground mode voltages. In the case of untransposed lines, the modal transformation matrix obtained by ATP software can be used.
2. DWT is applied to three-phase voltages (V_a, V_b, V_c) and ground-mode voltage (V_0) to obtain the wavelet transformation coefficients (*WTC*s) in scale-2. The selection of scale-2 over scale-1 is due to better performance for the investigated circuits in this study. *WTC*s are then squared to identify the arrival instants and hereafter denoted as WTC^2s.
3. The energies of voltage wavelet coefficients, E_{Vk} and currents, E_{Ik} ($k \in \{a,b,c \text{ and } 0\}$) are calculated over one cycle after the fault is detected

$$E_{Vk} = \sum_{m=0}^{M-1} WTC_k^2(m) \quad \text{for } k \in \{a,b,c \text{ and } 0\} \tag{6.1}$$

$$E_{Ik} = \sum_{m=0}^{M-1} I_k^2(m) \quad \text{for } k \in \{a,b,c \text{ and } 0\} \tag{6.2}$$

where E_{Vk} is the voltage wavelet energy, E_{Ik} is the current energy and M is the number of samples in one cycle.

4. The voltage wavelet energies and current energies are normalized as

$$E_{N_{Vk}} = \frac{E_{Vk}}{E_{Va}+E_{Vb}+E_{Vc}+E_{V0}} \text{ for } k\in\{a,b,c \text{ and } 0\} \quad (6.3)$$

$$E_{N_{Ik}} = \frac{E_{Ik}}{E_{Ia}+E_{Ib}+E_{Ic}+E_{I0}} \text{ for } k\in\{a,b,c \text{ and } 0\} \quad (6.4)$$

where $E_{N_{Vk}}$ is the normalized voltage wavelet energy and $E_{N_{Ik}}$ is the normalized current energy.

The training is carried out to obtain the optimum decision function for the binary SVM. The input features, $E_{N_{Vk}}$ and $E_{N_{Ik}}$ are stored in an $N\times 8$ training matrix where each column represents one feature and each row represents one training sample. N is the total number of different fault scenarios with different locations, types, FIAs, loadings and fault resistances. The flowchart of the algorithm is provided in Figure 36. SVM_1 is trained using the training matrix corresponding to an 8-dimensional feature space. Once the training process is completed and the optimal decision function for the two-class separation is known, the SVM_1 is ready to identify the faulty section.

6.3.2. SVM Faulty half Identification

The existing traveling wave-based fault location methods use the time delay between the arrival time of the initial traveling waves in ground mode and aerial mode for faulty half identification. SVM is utilized for faulty half identification, which makes the algorithm insensitive to the possible errors resulting from calculation of the time delay, especially for the faults close to the middle of the lines. The faulty half SVM identifiers are trained by using $E_{N_{Vk}}$ and $E_{N_{Ik}}$ described in the previous section. The SVM based decision tree (DT-SVM) for faulty half identification is shown in Figure 37, where SVM_2 and SVM_3 are utilized for faulty half identification in the overhead line and underground cable, respectively. Using a trained SVM for each section (i.e. line or cable) for all fault types is another advantage of the proposed method.

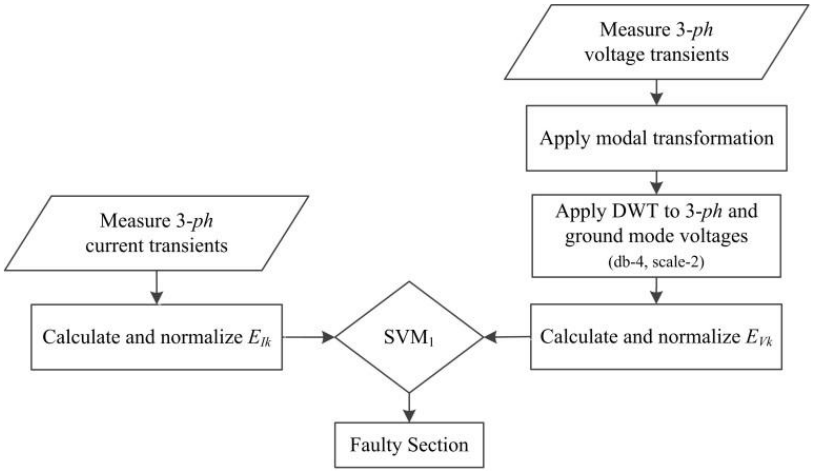

Figure 36. Faulty section identification flowchart

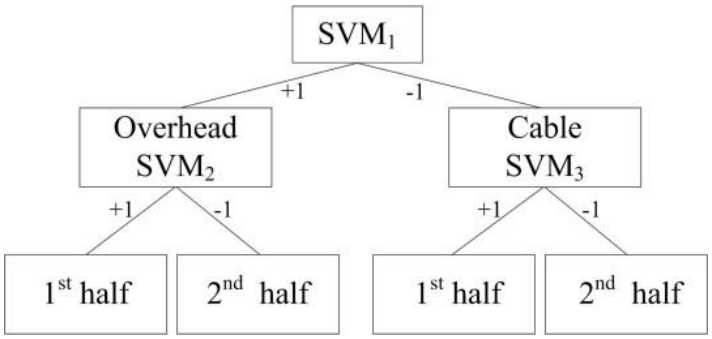

Figure 37. Faulty half identification DT-SVM diagram

6.3.3. Fault Location

Once the faulty section and half are identified, the single-ended traveling wave-based is utilized for fault location. For the faults located in the underground cable (F_A and F_B in Figure 38), the first peak of the traveling wave arrives at bus *S* at time t_{A1}. The first reflected backward traveling wave from the joint point arrives at bus S after t_{A1} with a time delay, 2τ where τ is the time required for a traveling wave to travel the full length of the line. Since the overhead line traveling wave velocity (v^{line}) and the line length (L_L) are known, 2τ is calculated

$$2\tau = \frac{2L_L}{v^{line}} \tag{6.5}$$

The traveling waves arriving at time instants $n\tau$ ($n=2, 4, 6,\ldots$) after the first observed traveling

wave are *not* used for fault location. For a fault in the first half of the cable, the fault location from bus S is calculated as

$$x = L_L + \frac{v^{cable}\Delta t}{2} \tag{6.6}$$

where v^{cable} is the propagation velocity along the underground cable calculated at the frequency corresponding to the middle value of scale-2 and Δt [s] is the time delay between the first (t_{A1}) and the second peak (t_{A2}) aerial mode voltage WTC^2s in scale-2 at bus S corresponding to backward traveling wave and the reflected backward traveling wave from the fault point, respectively. For a fault in the second half of the underground cable, the fault location is calculated as

$$x = L_L + L_C - \frac{v^{cable}\Delta t}{2} \tag{6.7}$$

where L_C [mi] is the length of the underground cable and Δt [s] is the time difference between the first (t_{B1}) and the second peak (t_{B2}) of WTC^2s at bus S corresponding to the backward traveling wave and the reflected forward traveling wave from bus R, respectively.

The single-ended traveling wave-based method developed in is utilized to locate the faults identified by SVMs in overhead line. For a fault in the first half of the overhead line, the time delay between the first and the second traveling waves, Δt [s] is used to calculate the fault location. The time delay is determined by observing aerial mode voltage WTC^2s in scale-2. Fault location is calculated as

$$x = \frac{v^{line}\Delta t}{2} \tag{6.8}$$

where v^{line} [mi/s] is the propagation velocity in the overhead line calculated at the frequency corresponding to the middle value of scale-2. For the faults identified in the second half of the overhead line, the first and the second traveling waves are used to calculate the fault location as

$$x = L_L - \frac{v^{line}\Delta t}{2} \tag{6.9}$$

where Δt [s] is the time delay between the first and the second peak of scale-2 aerial mode

voltage WTC^2s at bus S.

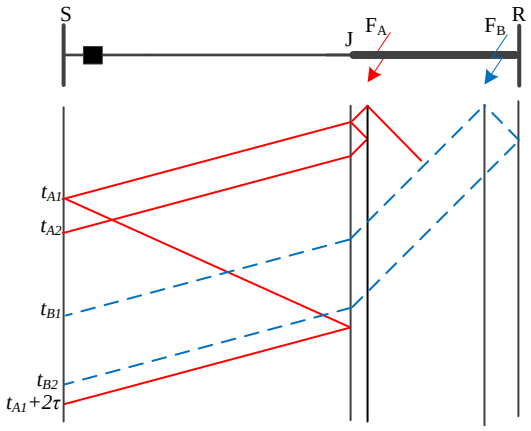

Figure 38. Bewley diagram of faults in underground cable

6.4. Simulation Results

The performance of the proposed fault location method is tested on a 230-kV, 60-Hz transmission line. Line lengths are assumed to be L_L=100 *mi* and L_C =20 *mi*. Transient simulations are carried out using ATP. Overhead line and underground cable are modeled as frequency-dependent. The overhead line tower structure and underground cable layout and the data are provided in Appendix A and B. The sampling time interval of voltage measurement is 5 *μs* (sampling frequency, f_s=200 *kHz*). The aerial mode traveling wave velocities are calculated using ATP software at 37.5 *kHz*, which corresponds to the middle value in scale-2 (25 *kHz* – 50 *kHz*). The velocities are 1.85×10^5 *mi/s* in overhead line and 0.98×10^5 *mi/s* in cable. MATLAB Wavelet Toolbox and SVM Toolbox are used to implement the proposed method. Gaussian noise is introduced to the measured transient voltages and currents to account for measurement noise. The noise is assumed to have zero mean and standard deviation equal to 1% of the sampled voltage or current signal.

Different fault scenarios under various system conditions (δ – loading, *FIA*, R_f and location of the fault) are simulated to evaluate the performance of the proposed method. The simulations are carried out for the following cases:

1) δ = 10˚ and 30˚
2) *FIA* =10˚, 45˚, 80˚ and 120˚

3) R_f=0.1 Ω, 100 Ω

4) L_f =10%, 20%, 30%,...,90% of the line and cable

A total of 2448 different cases that include all the conditions listed above are simulated. The feature extraction steps are performed on all obtained simulation results. The obtained input features and their corresponding outputs (i.e. +1 for the faults in the line and -1 for the faults in the cable) in the first loading level (δ = 10˚) are used to train the SVM faulty section/half identifiers.

The trained SVMs are then tested using the data set corresponding to all fault conditions at the second loading level. Other fault scenarios with different fault conditions (R_f and *FIA*) corresponding to the intermediate fault locations in the training set (e.g. fault occurring at δ = 20˚, R_f=1.5 Ω, L_f = 35.5%) are also tested. The faulty section identification accuracy is calculated as

$$\eta = \frac{\#\ of\ accurately\ identified\ faulty\ sections}{\#\ of\ test\ cases} 100 \qquad (6.10)$$

The accuracies for SVM faulty section/half identification with three different kernel functions are provided in Table 9. Note that the Gaussian RBF has better accuracy than the other kernel functions. The kernel function parameter (γ) is tuned to achieve sufficient accuracy. The identification accuracy deteriorates during extreme cases when a high-resistance fault (i.e. 50 Ω ≤ R_f ≤ 100 Ω) occurs at small fault inception angles (i.e. ≤ 5°). This combination produces smaller wavelet coefficients leading to low signal energies which makes it difficult for SVMs to identify the faulty section.

First scenario assumes that a phase *a*-to-ground fault occurs in overhead line at 87 miles from bus S. The fault conditions are assumed as follows: δ= 20°, *FIA*=35˚, R_f=0.5 Ω. The output of faulty section identifier SVM_1 is +1 identifying the faulty section as the overhead line. SVM_2 for faulty half identification in the line gives the output as -1 implying that the aerial mode (mode 1) voltage WTC^2s at scale-2, shown in Figure 39 is used for fault location. The time difference between the first and the second traveling waves peaks in WTC^2s, Δt is observed as 140 μs. The fault location is then calculated as

$$x = 100 - \frac{14 \times 10^{-5} \times 1.85 \times 10^{5}}{2} = 87.05\ mi$$

Second scenario assumes that a *b*-to-ground fault occurs in underground cable at 103 miles from bus S (i.e. 3 miles from J-point) with the conditions as δ=15°, *FIA*=275°, R_f=10 Ω. The faulty section identification is performed using SVM_1 resulting in -1 which implies an underground cable fault. The faulty half of the cable is then identified using SVM_3. The SVM_3 gives the output as +1 implying that the fault is in the second half. Voltage WTC^2s in aerial mode at scale-2 at bus S is shown in Figure 40. Δt is observed as 60 μs. The fault location is then calculated as

$$x = 100 + \frac{6 \times 10^{-5} \times 0.98 \times 10^{5}}{2} = 102.94\ mi$$

As the common practice, the absolute error is calculated as a percentage of the total section length in order to evaluate the effectiveness of the proposed fault location method using (5.6). Different cases of phase *a*-to-ground faults with 0.5 Ω fault resistance are considered. The results are presented in Table 10. The calculated fault locations show good correlation with the actual fault locations. The fault locations in the underground cable are calculated with respect to bus S.

Table 9. SVM faulty section/half identification accuracy with different kernel functions

		η (%)
SVM_1	Gaussian RBF	98.8
	Polynomial	96.7
	Linear	82.9
SVM_2	Gaussian RBF	98.2
	Polynomial	94.2
	Linear	81.6
SVM_3	Gaussian RBF	95.6
	Polynomial	92.3
	Linear	80.8

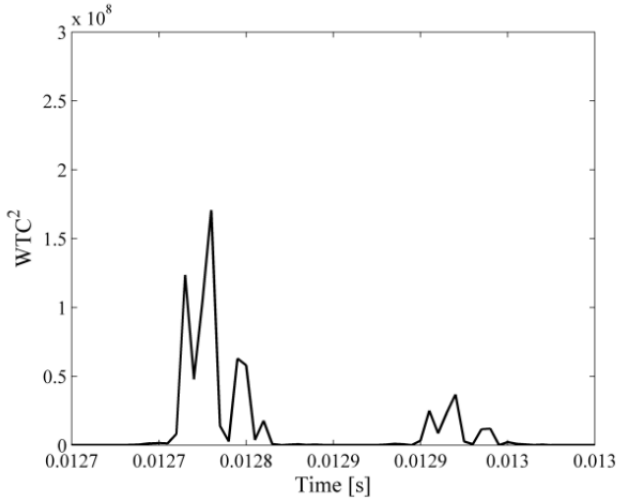

Figure 39. Voltage WTC^2s in aerial mode in scale-2 for a single-phase-to-ground fault in overhead line at 87 miles from bus S

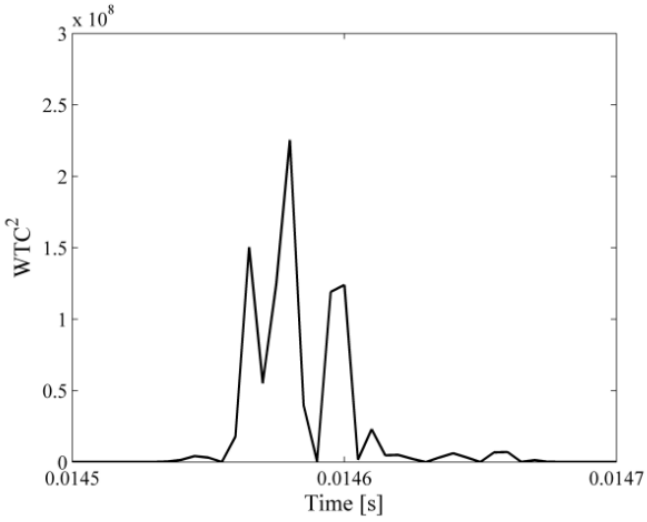

Figure 40. Voltage WTC^2s in aerial mode in scale-2 for a single-phase-to-ground fault in underground cable at 103 miles from bus S

Table 10. Fault location error analysis for different cases

Fault Section	Actual fault distance, AFD (mi)	Calculated fault distance, CFD (mi)	Error, e (%)
Line	5	5.55	0.55
	17	16.65	0.45
	23	23.12	0.12
	46	46.25	0.75
	84	83.35	0.65
	93	92.60	0.40
Cable	103	102.94	0.30
	105	104.41	2.95
	109	109.31	1.55
	115	115.10	0.50
	117	116.60	2.00
	118	118.04	0.20

6.5. The Effect of Fault Inception Angle

The severity of the fault initiated transients is affected by different fault inception angles; however, the use of normalized wavelet energies, $E_{N_{Vk}}$ and $E_{N_{Ik}}$ as input to the SVMs in the proposed method reduces these impacts. The results for four different locations with respect to the changes in *FIA* are shown in Table 11. The results show that the faulty section/half identification methods give reasonably accurate results for a wide range of fault inception angles varying between 6º and 354º. The method has satisfactory performance for locating the faults occurring under different fault inception angles as demonstrated in Table 11. Our investigations show that the misclassification zone around the middle point of the line or cable is 2 miles for extreme cases such as high-resistance (i.e. $R_f \geq 50\ \Omega$) faults or faults occurring at small fault inception angles (i.e. $FIA \leq 5^{\circ}$). The misclassification zone around the joint point is 3 miles for such cases.

6.6. The Effect of Fault Resistance

The performance of the proposed method is evaluated for a wide range of fault resistances. As in the case of small fault inception angles, high impedance faults (HIFs) affects the severity of the traveling waves, resulting in smaller signal energies. As mentioned in the previous subsection the use of $E_{N_{Vk}}$ and $E_{N_{Ik}}$ for faulty line/section identification, reduces the impacts of

high-impedances faults. The performance of the method is tested for fault resistances varying from 0.1 to 70 Ω.

The faulty section/half identification results for various fault resistances are demonstrated in Table 12 for different fault locations. The calculated fault distances and the corresponding errors do not change with fault resistance.

6.7. The Effect of Fault Type

The effects of fault type on the proposed method for faulty line and faulty half identification procedures as well as on fault location are evaluated in this section. The fault location results for two different locations in the overhead line and underground cable with respect to the fault type are shown in Table 13. Although different fault types affect the severity of the fault initiated traveling waves, the proposed method uses the normalized wavelet energies, $E_{N_{Vk}}$ and $E_{N_{Ik}}$as the input to the SVMs. As the results show, the faulty section/half identification methods give accurate results for four different fault types. Even though the arrival times of the traveling waves can vary slightly for different types of faults at a specific location, the time delay between consecutive traveling waves remains unchanged. As the time delay between the traveling waves is used to determine the fault location, the method gives satisfactory accuracy for locating the faults occurring under different types as demonstrated in Table 13.

6.8. The Effect of Non-Linear High Impedance Fault

The performance of the proposed method is evaluated for a non-linear high impedance fault (NLHIF). The model of the dynamic time-varying resistance and the utilized parameters are provided in chapter V in (5.7)-(5.10).

A single-phase-to-ground NLHIF is assumed to be located at 66 miles away from bus S on the overhead line. The fault conditions are assumed as follows: δ = 15° and *FIA*=310˚. The method first identifies the faulty section according to the output of SVM_1 which is +1. The SVM_2 for half side detection in the overhead line gives the output as -1. Thus the faulty half is determined in the second half of the line. Voltage WTC^2s at bus S in aerial mode at scale-2 are

finally observed to detect the time delay between the first two peaks, which is 360 μs. The fault location is calculated by using (6.9)

$$x = 100 - \frac{36 \times 10^{-5} \times 1.85 \times 10^{5}}{2} = 66.70\ mi$$

Similar to the cases of small fault inception angles and high-resistance faults, a NLHIF also affects the magnitude of the traveling waves. The arrival times of the traveling waves are delayed due to the impact of non-linear impedance on reflection and refraction coefficients. However, the time difference between the first and the second traveling wave arrivals remains unaffected. The delay for the simulated fault is observed to be in the order of 300 μs when compared with a resistive fault.

6.9. The Effect of Non-Ideal Fault

The performance of the proposed fault location method is evaluated for a non-ideal short-circuit fault. The 0.5 Ω resistance is connected through a 2 Ω inductance to the ground. A *b*-to-ground fault is located at 26 miles in the overhead line. The faulty section identification is first performed using SVM_1 which gives output as +1. The SVM_2 for half side identifier in the overhead line then gives the output -1. Thus the fault section is identified in the first half of the line. The aerial mode voltage WTC^2s at bus S at scale-2 are used and Δt is observed as 290 μs. Thus, the fault location is calculated using (6.8)

$$x = \frac{29 \times 10^{-5} \times 1.85 \times 10^{5}}{2} = 26.83\ mi$$

Even though the magnitudes of the traveling waves decrease as in the case of high-impedance faults and it also delays the arrival of the traveling waves for 20 μs, the time difference between the first two arriving waves remain unchanged. The proposed method gives satisfactory results in presence of non-ideal faults.

6.10. Discussions

6.10.1. Faulty Half Identification

In this section, the performance of the proposed method for faulty half identification is compared with that of an existing method. The time delay between the first traveling wave arrival in the ground and aerial mode WTC^2s, Δt_0 are used for faulty half identification in single-ended wavelet-based methods. In these methods, faulty half is identified by comparing Δt_0 with a pre-calculated time-delay for a fault located in the middle, Δt_m. For illustrative purposes, a phase *b*-to-ground fault is assumed to have occurred in the underground cable located at 5 miles from the joint (i.e. 105 miles from bus S). Figure 41 shows the voltage WTC^2s at bus S in aerial and ground mode at scale-2. The time delay for a fault in the middle of the underground cable (i.e. 10 *mi*) obtained using ATP simulation is Δt_m=50 μs. In this example the observed Δt_0 is 40 μs, identifying the faulty half accurately; however, very high precision is needed to compare Δt_m and Δt_0. It is also difficult to accurately calculate Δt_0 as Figure 41 demonstrates the proximity of the instants of initial peaks.

The proposed method in this dissertation uses SVMs for faulty half/section identification using the normalized wavelet energies, $E_{N_{Vk}}$ and normalized transient current energies, $E_{N_{Ik}}$ as input. The SVM_1 output for faulty section identification gives -1 and the half-identifier SVM_2 for the cable is utilized to determine the faulty half. The faulty half is identified as first half of the cable since the output of the SVM_2 is +1. The proposed method overcomes the precision problem pertinent to existing single-ended traveling wave methods using wavelet transform and Bewley diagram.

6.10.2. Cable Aging

The traveling wave velocity in cables decreases with aging due to the increase in cable inductance (L). The accuracy of single-ended traveling wave-based fault location degrades as the electromagnetic traveling wave velocity in the cable changes during the years.

As an example, a phase *a*-to-ground fault is simulated in the aged underground cable located at 13 miles from the joint (i.e. 113 miles from bus S). The aged underground is simulated by increasing the relative permeability (μ_r) of each phase from 1 to 1.5. The fault conditions are δ =

25°, R_f = 1 Ω and *FIA*=70°. The observed Δt in the voltage WTC^2s at bus S is 180 μs. The traveling wave velocity calculated using ATP software at 37.5 *kHz* in the aged underground cable is 0.8×10^5 *mi/s*. However, the fault location calculated by using the traveling wave velocity in the original cable (i.e. 0.98×10^5 *mi/s*) is

$$x = 100 + 20 - \frac{18 \times 10^{-5} \times 0.98 \times 10^5}{2} = 111.18\, mi$$

Note that the fault location error is 9.1%. As expected; the change in inductance due to aging affects the traveling wave- velocity, subsequently deteriorating the performance of the algorithm. This shortcoming can be addressed by introducing a correction factor, which translates the change in cable parameters to a change in velocity. Correction factor can be determined by carrying out site tests in certain time intervals or by employing a parameter estimation tool.

Table 11. Faulty line identification and fault location for different *FIA*

Fault	*FIA* (°)	SVM_1	SVM_2	SVM_3	CFD (mi)	*e* (%)
AG at 35th mi of line, δ= 20°, R_f=0.5 Ω	7	1	1	n/a	35.15	0.15
	30	1	1	n/a		
	150	1	1	n/a		
	330	1	1	n/a		
BC at 67th mi of line, δ = 25°	45	1	-1	n/a	66.61	0.39
	170	1	-1	n/a		
	350	1	-1	n/a		
	352	1	-1	n/a		
CG at 7th mi of cable, δ = 20°, R_f=1.5 Ω	55	-1	n/a	1	6.60	2.00
	110	-1	n/a	1		
	300	-1	n/a	1		
	354	-1	n/a	1		
AG at 13rd mi of cable, δ = 20°, R_f=0.5 Ω	6	-1	n/a	-1	13.14	0.70
	25	-1	n/a	-1		
	100	-1	n/a	-1		
	340	-1	n/a	-1		

Table 12. Faulty line identification and fault location for different R_f

Fault	R_f (Ω)	SVM_1	SVM_2	SVM_3	CFD (mi)	*e* (%)
AG at 35th mi of line, δ= 20°	0.1	1	1	n/a	35.15	0.15
	2	1	1	n/a		
	70	1	1	n/a		
BC at 74th mi of line, δ = 25°	0.5	1	1	n/a	74.10	0.90
	1.5	1	-1	n/a		
	10	1	-1	n/a		
CG at 7th mi of cable, δ = 20°	0.01	-1	n/a	1	6.86	0.70
	5	-1	n/a	1		
	15	-1	n/a	1		
BG at 15th mi of cable, δ = 20°	1	-1	n/a	-1	14.60	2.00
	10	-1	n/a	-1		
	20	-1	n/a	-1		

Table 13. Faulty line identification and fault location for different fault type

Fault	Type	SVM_1	SVM_2	SVM_3	CFD (mi)	*e* (%)
8th mi of line, δ= 20°, R_f=0.5 Ω, *FIA=15°*	*AG*	1	1	n/a	7.6	0.40
	BCG	1	1	n/a		
	AC	1	1	n/a		
	ABCG	1	1	n/a		
18th mi of cable, δ = 25°, R_f=1 Ω, *FIA=160°*	*CG*	-1	n/a	-1	18.04	0.20
	ABG	-1	n/a	-1		
	BC	-1	n/a	-1		
	ABCG	-1	n/a	-1		

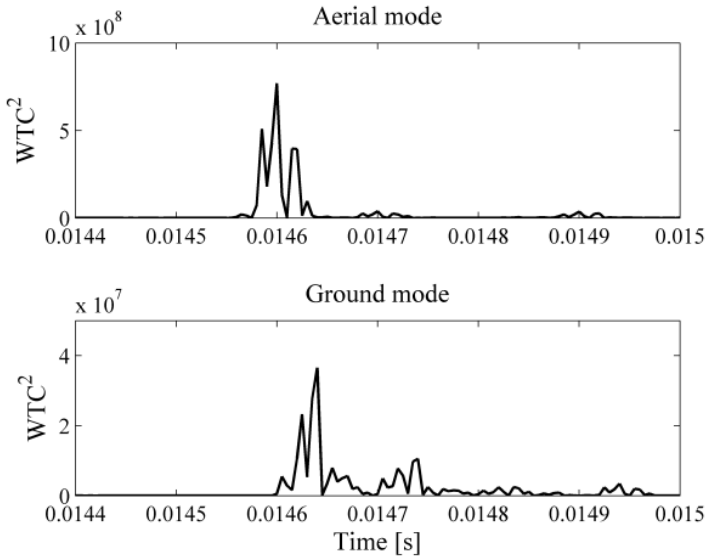

Figure 41. Voltage WTC^2s at bus S in aerial and ground mode in scale-2 for a phase-*b*-ground fault at 105 miles away from bus S in underground cable

6.11. Summary

This chapter proposes a single-ended traveling wave-based fault location method for a hybrid transmission line: an overhead line combined with an underground cable. Modal transformation and DWT are applied to the transient voltages recorded at the sending-end of overhead line. The normalized voltage wavelet energies and the normalized current energies are used for SVM faulty section/half identification. The SVM classifiers use smaller set of inputs and are independent of fault type. The location of the fault is calculated by using the aerial mode voltage wavelets. The transient simulations are carried out using ATP software and the method is tested on MATLAB by using Wavelet Toolbox and SVM Toolbox. The performance of the proposed method is tested for various fault scenarios including different fault resistances, fault inception angles, fault locations, loading levels, non-linear high-impedance and non-ideal faults with satisfactory results.

*Chapter VII: Fault Location for Segmented HVDC Transmission Lines**

7.1. Introduction

HVDC transmission systems have increasingly been used in modern power transmission networks due to many advantages, such as, providing higher power transmission capability over long distances, interconnecting asynchronous systems and having the potential for accommodating very-large scale intermittent electrical energy (i.e. wind and solar). The European super grid is an HVDC transmission system proposed to transmit renewable energy-based electrical power from the remote locations to the load centers [122]. Combination of overhead lines and underground cables has been deployed as a segmented HVDC transmission system when two networks separated by water need to be connected. In addition, underground cables are utilized to connect off-shore wind farms to the existing grid through overhead lines. However, the complexity of fault location problem increases with the proliferation of such unusual topologies. Accurate and fast detection and location of faults along HVDC transmission lines are vital to improve power system reliability and availability. Traveling wave-based fault location method is proposed for HVDC transmission lines. The traveling wave-based methods have high accuracy and the results are not affected by the parameters, such as ground resistance or loading conditions. Traveling wave-based methods are grouped into two subcategories with respect to the measurements they employ at the receiving and/or sending ends of the transmission lines:

- Single-ended, and
- Multi-ended (synchronized).

This chapter reviews the existing methods in the literature for fault location in HVDC transmission lines and then presents a single-ended traveling wave-based fault location method

*Reprinted with permission from "A single-ended fault location method for segmented HVDC transmission line," by H. Livani and C. Y. Evrenosoglu, 2014. *Electric Power System Research*, vol. 107, pp. 190-198. Copyright 2014 Elsevier.

for segmented high voltage DC (HVDC) transmission lines; an overhead line combined with an underground cable. DC transient voltage and current signals at the sending-end of the overhead line are assumed to be available. DWT is then applied to the DC voltage and current signals. The wavelet energies of voltage and current transients over 16 ms (i.e. 1-cyle in 60-Hz frequency) are calculated and then normalized. The normalized energies are used as the input to a binary SVM classifier for faulty section identification (underground cable or overhead line). Once the faulty section is identified, the faulty half is determined by comparing polarity of the first two current traveling waves. Bewley diagrams are finally observed for the traveling wave pattern and the wavelet coefficients squared of DC voltage are used to locate the fault. The transient voltage and current for different fault locations are simulated using the ATP software. MATLAB is used to process the simulated transients and apply the proposed method. The main contributions of the proposed method are as follows:

- The fault location method is carried out using single–ended measurements.
- The proposed method uses SVM for faulty section identification.
- The proposed SVM classifier uses a two-dimensional input for decision making.

7.2. Existing Solutions

In [123]-[124], a single-ended fault location method for HVDC transmission systems with overhead line is proposed. Current traveling waves are used for fault location. [125] proposes a two-ended traveling wave-based fault location method for a two-terminal HVDC transmission system. Arrival times of the fault initiated traveling waves at both ends of the line are detected using global positioning system (GPS). In [126], a traveling wave-based faulty-pole selection and protection scheme are proposed and implemented. [127] presents a single-ended fault location and protection scheme for multi-terminal HVDC systems. The proposed fault location and protection is based on continuous wavelet transformation (CWT) of measured DC voltage. [128] proposes a fault location and isolation method in multi-terminal HVDC systems. The main purpose of the proposed method is to develop a protection scheme which uses AC circuit breaker to clear the fault.

A single-ended fault detection and location method for HVDC transmission systems using DWT is first proposed in [129]. The two-ended traveling wave-based fault location method for a HVDC transmission system is implemented in [130]. A two-ended fault location method for overhead HVDC transmission line using steady-state voltages and currents is proposed in [131]. The proposed method is based on the distributed parameter line model. The DC voltages at discrete points along the DC line are calculated using the voltage and current measurements from both terminals, separately. The fault location is then estimated by comparing the calculated voltages from both ends.

For segmented HVDC transmission lines, a two-ended traveling wave-based fault location method is proposed in [132] and [133]. CWT is utilized to detect the arrival times of traveling waves at both terminals. The fault location is then calculated using the detected arrival times of traveling waves at both ends. A single-ended traveling wave-based fault location for segmented HVDC transmission line is proposed for the time in [134].

7.3. Proposed Fault Location Method

This section describes the proposed single-ended traveling wave-based fault location method for the segmented HVDC transmission system including an overhead line combined with an underground cable. The one-line diagram of the segmented HVDC transmission system is shown in Figure 42, where L_L is the length of the overhead line and L_C is the length of the underground cable.

The proposed method is developed based on the following assumptions:

- Single-ended measurements at the overhead line are available,
- The measurements are obtained through optic voltage and current recorders
- DC voltage and current signals are measured at high sampling rates (i.e. f >100 kHz),
- Measurement devices are not available at the joint point.

Figure 43 shows the DC terminal of the HVDC system. The current measurement is assumed to be available before DC smoothing reactor as shown in Figure 43, in order to ensure that transient current signals are not filtered out by the reactor.

The general procedure for the proposed fault location method is summarized as follows:

1. The faulty section is first identified using a binary SVM classier.
2. The polarities of the current traveling waves are then observed for faulty half identification.
3. The squared wavelet transform coefficients of DC voltage are finally observed for fault location.

The following sections describe the proposed faulty section/half identification and fault location methods.

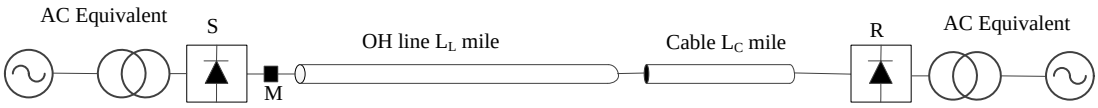

Figure 42. A ±500 kV segmented HVDC transmission system including an overhead line combined with an underground cable

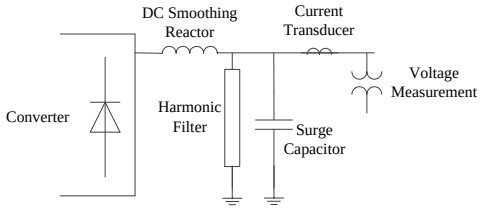

Figure 43. DC side terminal of the HVDC system with voltage and current measurements

7.3.1. SVM Faulty Section Identification

In this section, a traveling wave-based faulty section identification method in the segmented HVDC transmission system, using DWT and SVM is presented. Faulty section identification is performed using one binary support vector machine, SVM. The SVM output implies whether the fault is in the overhead line (+1) or in the underground cable (-1).

The SVM identifier needs to be trained using different fault scenarios in a given topology. Then, the performance of the proposed method is evaluated by using other fault scenarios.

Wavelet energies of DC voltage and current signals are used as the input to the binary SVM. The algorithm for obtaining the input features of the SVM is summarized as the following steps:

1. DC voltage and current signals at the overhead line end are measured.
2. DWT is applied once to DC voltage and current to obtain the wavelet transform coefficients (*WTC*s) using *Haar* mother wavelet in scale-2, which are then squared to clearly identify the arrival instants and denoted as WTC^2s. The selection of scale-2 over scale-1 is due to the better performance for the investigated system in this study.
3. The voltage wavelet energies, E_V and current wavelet energies, E_I are calculated by summation of WTC^2s over 16 *ms* after the fault is detected as

$$E_k = \sum_{m=1}^{M} WTC_k^2(m) \quad \text{for } k \in \{V \,\&\, I\} \tag{7.1}$$

   where M is the number of samples in 16 *ms*.

4. The calculated wavelet energies are normalized using mean (M_k) and standard deviation (STD_k) of training input data set as

$$E_{NK}(j) = \frac{E_k(j) - M_k}{STD_k}, \text{ for } k \in \{V \,\&\, I\} \text{ and } j = 1:N \tag{7.2}$$

$$M_k = \frac{1}{N}\sum_{i=1}^{N} E_k(i) \tag{7.3}$$

$$STD_k = \sqrt{\frac{1}{N}\sum_{i=1}^{N}(E_k(i) - M_k)^2} \tag{7.4}$$

where N is the total number of different fault scenarios with different locations, loadings and fault resistances for training data set. Normalized wavelet energies of transient voltages and normalized energies of transient currents are used as input to the binary SVM classifiers.

The training step for the SVM is carried out to obtain the optimum decision function. The input features are E_{NV} and E_{NI}. Thus, the processed values are stored in an $N \times 2$ training matrix where each column represents one feature and each row represents one training sample. The flowchart of the algorithm is shown in Figure 44. Once the training process is completed and the optimal decision function for the two-class separation is known, the SVM is ready to classify new incoming data sets.

7.3.2. Faulty Half Identification

For a fault occurred in the first half of the line (F_A), as shown in Figure 45 a negative current traveling wave propagates toward bus S, and a positive current traveling wave propagates toward the remote end (i.e. joint). The reflected current traveling wave from bus S travels back toward the fault point and reflects back from the fault point towards bus S with no sign change. Thus, the second observed current traveling wave at bus S has the same polarity as the first observed current traveling wave.

For a fault in the second half of the transmission line (F_B in Figure 45), the first traveling wave arrives at bus S with negative sign. The second traveling wave observed at bus S, is now the forward traveling wave which reflects back from the remote end (i.e. joint point) with positive sign. Since the sign patterns of the first two current traveling waves are different for F_A and F_B, the faulty half of the overhead line or underground cable is determined by comparing the observed current traveling waves.

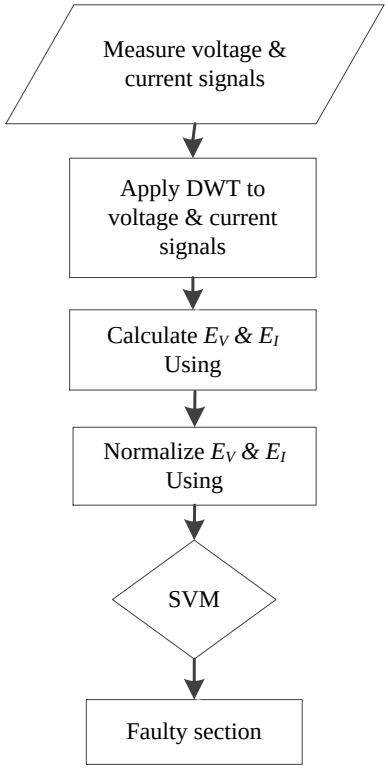

Figure 44. Faulty section identification flowchart

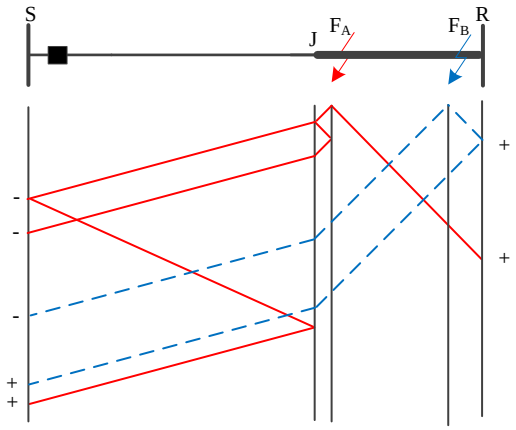

Figure 45. Bewley diagram showing the current traveling wave polarity pattern

7.3.3. Traveling Wave-Based Fault Location

Once the faulty section and the faulty half are identified, the single-ended traveling wave-based method is utilized for fault location.

For the faults located in the underground cable (F_A and F_B in Figure 46), the first peak of the traveling wave arrives at bus *S* at time t_{A1}. The first reflected backward traveling wave from the joint point arrives at bus S after t_{A1} with a time delay 2τ, where τ is the time required for a traveling wave to travel the full length of the line. Since the overhead line traveling wave velocity (v^{line}) and the line length (L_L) are known, 2τ is calculated as

$$2\tau = \frac{2L_L}{v^{line}} \tag{7.5}$$

The traveling waves arriving at time instants $n\tau$ ($n=2, 4, 6,\ldots$) after the first observed traveling wave are *not* used for fault location. For a fault in the first half of the cable, the fault location from bus S is calculated as

$$x = L_L + \frac{v^{cable}\Delta t}{2} \tag{7.6}$$

where $L_L\,[mi]$ is the length of the overhead line, v^{cable} is the propagation velocity along the cable calculated at the frequency corresponding to the middle value of scale-2 and Δt $[s]$ is the time delay between the first (t_{A1}) and the second peak (t_{A2}) aerial mode voltage WTC^2s in scale-2 at

bus S corresponding to backward traveling wave and the reflected backward traveling wave from the fault point, respectively.

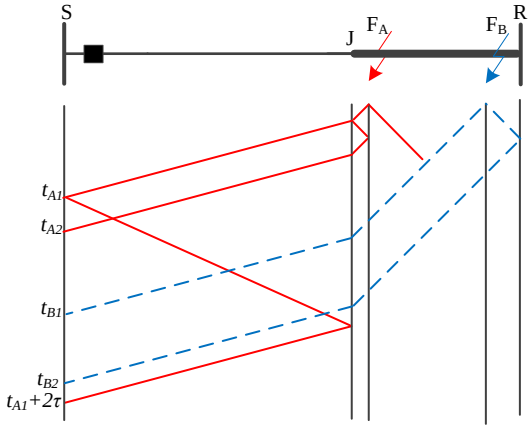

Figure 46. Bewley diagram of faults located in the underground cable

For a fault in the second half of the underground cable, the fault location is calculated as

$$x = L_L + L_C - \frac{v^{cable}\Delta t}{2} \tag{7.7}$$

where $L_C\,[mi]$ is the length of the cable, Δt $[s]$ is the time difference between the first (t_{B1}) and the second peak (t_{B2}) of WTC^2s at bus S corresponding to the backward traveling wave and the reflected forward traveling wave from bus R, respectively.

The single-ended traveling wave-based method developed in is utilized to locate the faults identified by SVMs in overhead line. For a fault in the first half of the overhead line, the time delay between the first and the second traveling waves, Δt $[s]$ is used to calculate the fault location. The time delay is determined by observing aerial mode voltage WTC^2s in scale-2. Fault location is calculated as

$$x = \frac{v^{line}\Delta t}{2} \tag{7.8}$$

where v^{line} $[mi/s]$ is the propagation velocity in the overhead line calculated at the frequency corresponding to the middle value of scale-2. For the faults identified in the second half of the overhead line, the first and the second traveling waves are used to calculate the fault location as

$$x = L_L - \frac{v^{line}\Delta t}{2} \tag{7.9}$$

where Δt [s] is the time delay between the first and the second peak of scale-2 aerial mode voltage WTC^2s at bus S.

7.4. Simulation Results

The simulation results for a ±500 kV HVDC transmission system is presented in this section. Line segments length are L_L=500 miles and L_C=100 miles. Transient simulations are carried out by using ATP software. Overhead line and underground cable are modeled as frequency dependent. The overhead line tower structure and underground cable layout and the utilized data are enclosed in Appendix C. The sampling time interval of voltage and current measurement is 5 μs (the sampling frequency, f_s=200 *kHz*). The traveling wave velocities calculated using ATP software at 37.5 kHz in overhead line and underground cable are 1.85×10^5 and 0.98×10^5 *mi/s*, respectively. MATLAB Wavelet Toolbox and SVM Toolbox are finally used to implement the proposed method.

Gaussian RBF kernel function is considered for training and testing the SVM fault section identifier. The kernel function parameter (γ) is tuned to achieve sufficient accuracy.

In order to consider the measurement noise, Gaussian noise is added to the measured voltage and current signals in all simulations. The noise has zero mean and standard deviation equal to 1% of the sampled voltage or current signal.

The performance of the proposed method is evaluated with different fault scenarios under various system conditions (loading, R_f and fault location). The simulations are carried out with the following values:

1) Two different loading from bus S to bus R (800 and 1000 MW),
2) R_f=0.1 Ω, 1 Ω, 10 Ω, 50 Ω and 100 Ω,
3) L_f =1%, 2%… 99% of the lines length.

A total of 1062 different cases, which includes all of the conditions itemized above, are simulated. The feature extraction steps are performed on all simulation results. The obtained input features and their corresponding outputs (i.e. +1 for the faults in the line and -1 for the faults in the cable) in the first loading level (800 MW) are used to train the SVM faulty section identifier.

The trained SVM is then tested using the data set corresponding to all fault conditions at the second load level. Other fault scenarios with different fault resistances (R_f) corresponding to the intermediate fault locations in the training set (e.g. fault with R_f=1.5 Ω, L_f = 35.5%) are also tested. The faulty section identification accuracy is calculated using (6.10).

The accuracy for SVM faulty section identification with three different kernel functions is provided in Table 14. As observed, the Gaussian RBF has better accuracy than the other two kernel functions. In order to compare the proposed method results with another classification method, the faulty section identification accuracies using a decision three (DT) is also presented in Table 14. Note that the accuracies of SVM classifiers are better than the accuracies of DT.

Table 14. SVM faulty section identification accuracy with different kernel functions

Kernel function	η (%)
Gaussian RBF	98.2
Polynomial	95.5
Linear	93.2
Decision Tree (DT)	88.1

Next, the fault location results using the proposed method for two fault scenarios are discussed. First scenario assumes a single-pole-to-ground fault located in the overhead line at 153 *miles* from the sending-end of the overhead line. The fault resistance is R_f =0.5 Ω. The normalized wavelet energies E_{NV} & E_{NI} are calculated which are then utilized as the input to SVM for faulty section identification. The SVM output is +1 which identifies the fault in the overhead line. The current transient signals are then observed to identify the faulty half of the line. As it is shown in Figure 47, the first two current traveling waves have the same polarity of change. Thus, the fault is identified in the first half of the overhead line.

Once the faulty half is identified, the DC voltage WTC^2s is observed to determine Δt. Figure 48 shows the DC voltage WTC^2s and Δt is 1.65 *ms*. The fault location is then calculated as

$$x = \frac{165 \times 10^{-5} \times 1.85 \times 10^{5}}{2} = 152.63 mi$$

The second scenario is another single-pole-to-ground fault, located in the underground cable at 566 *miles* from bus S (i.e. 66 *miles* from the joint point). The normalized wavelet energies, E_{NV} & E_{NI} are used as the input to the faulty section identification SVM resulting in -1 which implies an underground cable fault. The faulty half of the cable is then identified using the current signal. Figure 49 shows the current signal in the faulty pole. As the first and the second current traveling waves have apposite polarities, the fault is identified in the second half of the cable. DC voltage WTC^2s are then observed to determine Δt. According to the obtained WTC^2s in Figure 50, Δt is 0.68 *ms*. The fault location is finally calculated as

$$x = 500 + 100 - \frac{68 \times 10^{-5} \times 0.98 \times 10^{5}}{2} = 566.68 mi$$

The effectiveness of the proposed fault location method is evaluated using the error which is calculated as a percentage of the total system length using (5.6).

The fault location results of single-pole-to-ground faults with different locations and resistances are presented in Table 15. The fault locations in the underground cable are calculated with respect to bus S. The results given in Tables 15, show good accuracy of the proposed method for fault location.

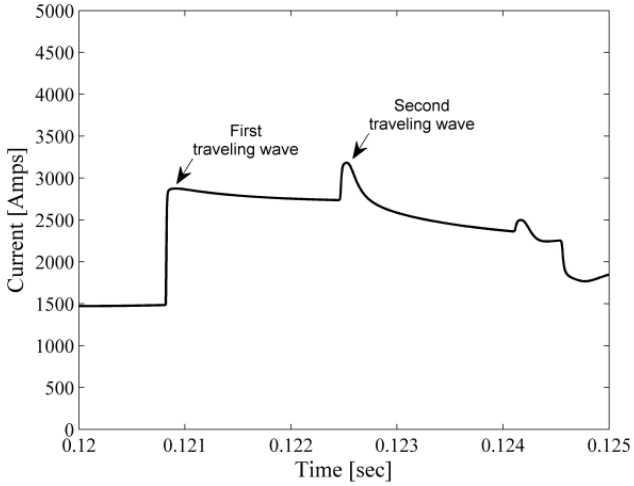

Figure 47. Pole-1 current for a single-pole-to-ground fault at 153 miles in the overhead line

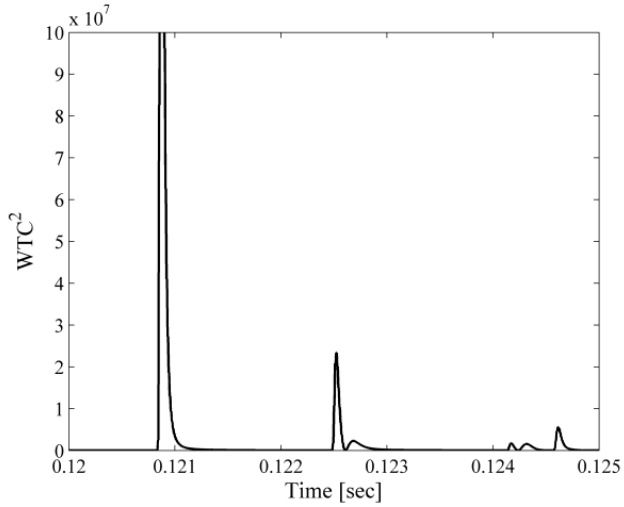

Figure 48. DC Voltage *WTC*^{2}s in scale-2 for a single-pole-to-ground fault at 153 miles in the overhead line

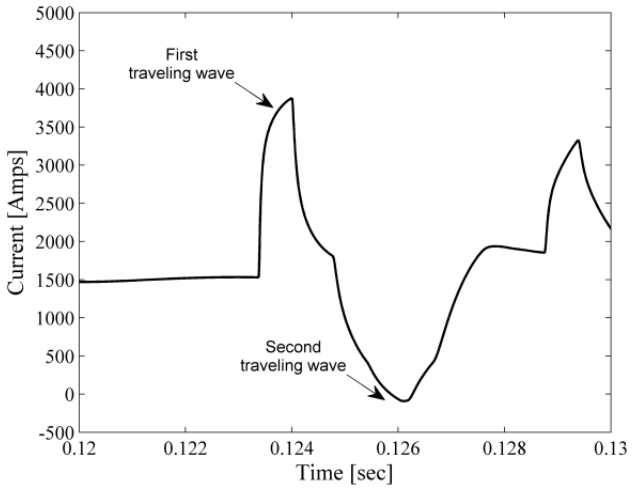

Figure 49. Pole-1 current for a single-pole-to-ground fault at 566 miles in the underground cable

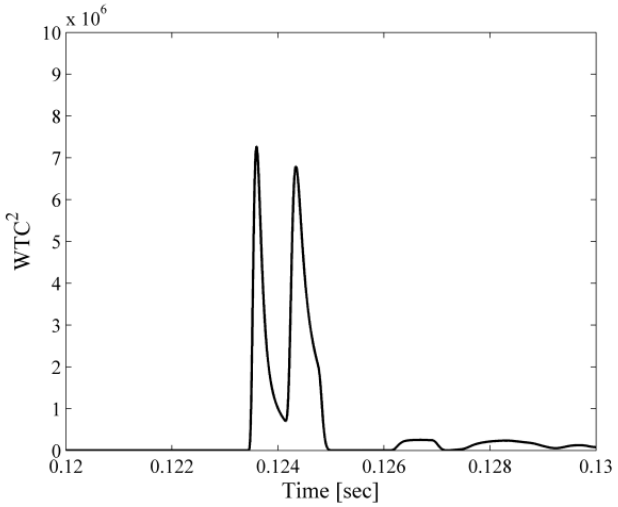

Figure 50. DC Voltage WTC^2s in scale-2 for a single-pole-to-ground fault at 566 miles from bus S in the underground cable

7.5. The Effect of Fault Resistance

In order to consider the effect of fault resistance on the performance of the proposed method, single-pole-to-ground faults in the line and cable are simulated with different fault resistances. The performance of the method is tested for a wide range of fault resistance from 0.5 to 70 Ω. The fault location results for three different fault resistances are shown in Table 16 for four different fault locations. Note that the fault impedance affects the severity of the traveling waves; however, as the time delay between the traveling waves is used to determine the fault location, the method remains insensitive to different fault resistances.

7.6. The Effect of Non-Linear High Impedance Fault

A dynamically time varying resistance model is used to evaluate the performance of the proposed method with non-linear high impedance fault (NLHIF) using equations and parameters provided in chapter V in (5.7)-(5.10).

A single-pole-to-ground NLHIF is located at 363 miles in the overhead line. The method first identifies the fault as a line fault according to the output of SVM faulty section identifier. The half side identification is then performed considering the current traveling waves polarity changes. The transient current is shown in Figure 51. As the first and the second current traveling

waves have apposite polarities, the fault is in the second half of the line. The fault location is finally calculated by observing DC voltage WTC^2s given in Figure 52 by using (7.9) as

$$x = 500 - \frac{148 \times 10^{-5} \times 1.85 \times 10^{5}}{2} = 363.10\, mi$$

Table 15. Fault location error analysis for different cases

Fault Section	Actual fault distance (mi)	Fault resistance (Ω)	Calculated fault distance (mi)	Error (%)
Line	5	0.5	5.55	0.11
	53	1.5	52.73	0.05
	87	0.2	86.95	0.01
	156	10	155.60	0.08
	306	0.01	305.75	0.05
	372	25	372.28	0.05
	426	2	426.93	0.18
Cable	509	0.01	508.82	0.18
	517	0.05	517.33	0.33
	526	0.5	26.46	0.46
	538	0.2	38.22	0.22
	554	1.5	53.94	0.06
	569	3	569.13	0.13
	583	0.6	582.85	0.15

Table 16. Faulty section identification and fault location for single-pole-to-ground fault with different resistances

Actual fault location (mi)	R_f (Ω)	SVM	Calculated fault distance (mi)	Error (%)
Line fault at 217	0.5	1	217.38	0.08
	2	1		
	70	1		
Line fault at 454	0.5	1	453.75	0.05
	2	1		
	70	1		
Cable fault at 523	0.5	-1	523.52	0.52
	2	-1		
	70	-1		
Cable fault at 588	0.5	-1	588.24	0.12
	2	-1		
	70	-1		

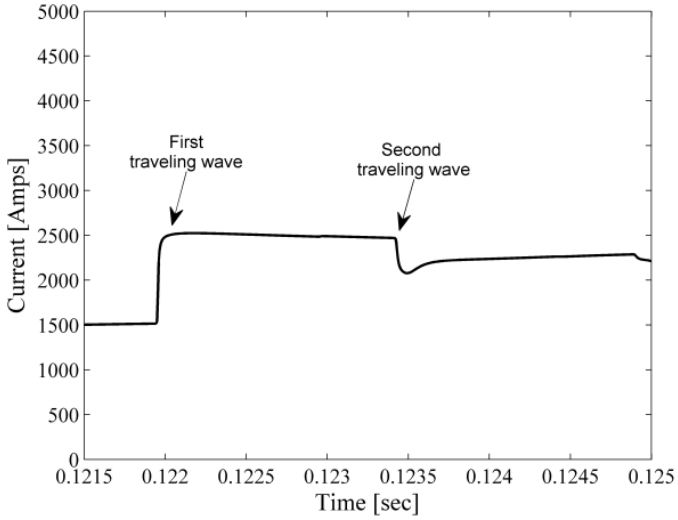

Figure 51. Pole-1 current for a single-pole-to-ground NLHIF at 363 miles in the overhead line

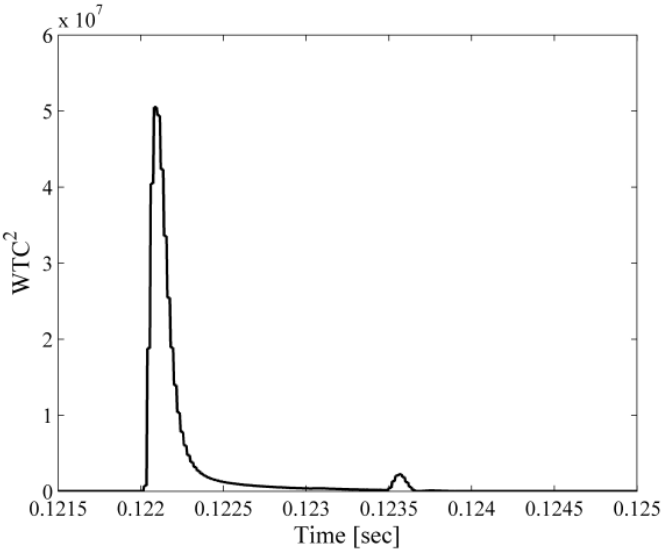

Figure 52. DC Voltage WTC^2s in scale-2 for a single-pole-to-ground NLHIF at 363 miles in the overhead line

7.7. The Sensitivity of Faulty Section Identification

The magnitude of voltage and current transients change with respect to fault location and fault resistances subsequently affecting the calculated voltage wavelet energies and current energies and deteriorate the performance of the SVM classifier. In this section, the performance of the proposed method for faulty section identification to fault resistance is presented. Our investigations show that the misclassification zone around the joint point of the line and cable is 5 miles for extreme high-resistance (i.e. $R_f \geq 50\ \Omega$) faults.

7.8. Cable Aging Consideration

The traveling wave velocity in cables decreases with aging due to the increase in cable inductance. The accuracy of single-ended traveling wave-based fault location degrades as the electromagnetic traveling wave velocity in the cable changes during the years.

As an example, a single-pole-to-ground fault is simulated in the aged underground cable located at 37 miles from the joint (i.e. 537 miles from bus S). The aged underground is simulated by increasing the relative permeability (μ_r) of each phase from 1 to 1.5. The fault resistance is R_f = 0.5 Ω. The observed Δt in the voltage WTC^2s at bus S is 0.9 *ms*. The traveling wave velocity calculated using ATP software at 37.5 *kHz* in the aged underground cable is 0.8×10^5 *mi/s*. However, the fault location calculated by utilizing traveling wave velocity in the original cable (i.e. 0.98×10^5 *mi/s*) is

$$x = 500 + \frac{90\times10^{-5}\times0.98\times10^{5}}{2} = 544.10\,mi$$

Note that the fault location error is 7.1%. As expected; the change in inductance due to aging affects the traveling wave- velocity, subsequently deteriorating the performance of the algorithm. This shortcoming can be addressed by introducing a correction factor, which translates the change in cable parameters to a change in velocity. Correction factor can be determined by carrying out site tests in certain time intervals or by employing a parameter estimation tool.

7.9. Summary

In this chapter, a single-ended traveling wave-based fault location method for segmented HVDC transmission systems is proposed. The segmented HVDC system is composed of an overhead line combined with an underground cable. The proposed fault location is performed in three main steps. DWT is applied to the transient DC voltage and current signals to obtain wavelet energies. The calculated normalized energies are used as the input to the SVM classifier for faulty section identification (i.e. overhead line or underground cable) as the first step. The faulty half identification is then performed as the second step by comparing the current traveling wave's polarities observed at the measurement end. The DC voltage WTC^2s are finally observed to determine the exact time delay between the first and the second traveling waves. The obtained time delay is utilized for fault location along the HVDC transmission system based on traveling wave's theory. The performance of the proposed method is tested with various fault scenarios including different fault resistances, and locations. The method is also tested with NLHIF and it gives satisfactory results for all fault conditions.

Chapter VIII: Conclusions

8.1. Summary

An electric power grid comprises of power generation, transformers, transmission, and distribution lines. Transmission lines are used to transmit electric power to load centers. The rapid growth of electric power demand and the advent of renewable energy-based power generation over the past few decades have resulted in a large increase of complex transmission lines in operation. These lines are exposed to faults as a result of lightning, short circuits, faulty equipment, mis-operation and human errors, overloading, and aging. These faults cause short to long-term power outages for customers and result in significant economic losses especially for the manufacturing industry. Most electrical faults result in mechanical damages, which must be repaired before restoring the line back to service. Faulty transmission line restoration can be accelerated if the fault location is either known or can be estimated with a reasonable accuracy. A quick detection, repair and maintenance process directly leads to improve the power availability to customers and consequently to enhance the overall reliability and efficiency of power grids.

This dissertation presents new fault location methods for smart power grids by using discrete wavelet transformation (DWT) and support vector machine (SVM). The new fault location methods are developed for complex transmission topologies as, three-terminal transmission lines, hybrid HVAC transmission lines and segmented HVDC transmission lines. The proposed fault location algorithms are traveling wave-based. DWT is utilized to extract the traveling wave information from the transient voltage and current measurements. SVM is utilized for fault classification and faulty section identification. Extensive studies are carried out to select the best kernel functions for each classifier and to tune the selected kernel function parameters. The selected kernel functions with the tuned parameters are used to classify the fault type or to identify the faulty section in the transmission line. The best kernel function and their tuned parameters are selected based on better fault classification and/or faulty section identification accuracies in the training step. The dissertation contributions are summarized in the following section.

8.2. Dissertation Contributions

Proliferation of advanced measurement technologies such as optic current and voltage transducers (CTs and VTs) can provide a venue for the implementation of traveling wave-based fault location methods. Optic CTs and VTs are capable of capturing high-frequency transients in high- and extra-high-voltage power systems. These modern technologies offer the advantages of high accuracy, optical isolation, and wide range of frequency response. Thus, the realization of precise fault location method using optical measurements with high sampling frequency (e.g. 200 kHz) becomes a reality with the proliferation of such modern technologies. Research contributions of this dissertation are summarized below under three different topics.

8.2.1. Fault Classification and Location for Three-Terminal Transmission Lines

A fault classification and location method for three-terminal power transmission systems is proposed in this section. The proposed method is based on the high-frequency traveling-wave information extracted from the voltage and current signals measured at two terminals. In the proposed method, DWT is utilized to extract transient information from the recorded voltages at only two terminals. SVM classifiers are then used to classify the fault type and faulty line/half in the transmission lines. The first contribution of the proposed method is that it utilizes normalized wavelet voltage energies from only two terminals. Thus, the total cost of implementation is decreased by avoiding installation cost of optic voltage transducer and the required communication devices at the third terminal. The second contribution of the proposed method is the elimination of using time delay between the aerial mode and the ground mode traveling wave's arrival times for faulty half identification used in existing traveling wave–based fault location methods. Instead the proposed method uses SVM for faulty half identification. This overcomes the challenging task of capturing the delay in the aerial mode and the ground mode traveling wave's arrival time as the wave velocities in these two modes are close to each other. The third contribution of the proposed method is that the SVM classifiers employ 8-dimensional input, which is significantly less than the dimension of the inputs used in the existing methods. Bewley diagrams are observed for the traveling wave patterns and the wavelet coefficients of the aerial mode voltage are used to locate the fault precisely.

8.2.2. Fault Location for Hybrid HVAC Transmission Lines

In this section, a single-ended traveling wave-based fault location method is proposed for a hybrid high HVAC transmission line: an overhead line combined with an underground cable. DWT is utilized to extract transient information from the measured voltages and currents. SVM classifiers are then utilized to identify the faulty section/half. The first contribution of the proposed method is that it utilizes a binary SVM classifier instead of using the time delay between arrival times of traveling waves in the aerial mode and the ground mode. The second contribution of the proposed method is that the SVM classifiers employ 8-dimensional input, which is significantly less than the dimension of the inputs used in the existing methods. Exact fault location is calculated by observing Bewley diagrams corresponding to the wavelet coefficients of the aerial mode voltage to find the traveling wave patterns.

8.2.3. Fault Location for Segmented HVDC Transmission Lines

The main challenge in traveling wave-based fault location for segmented HVDC transmission lines (i.e. overhead line combined with underground cable) is faulty section identification. This challenge is due to the reflections of the fault signal from the joint-point and the fault point as well as the unequal traveling wave velocities in line and cable. This dissertation presents a new single-ended traveling wave-based fault location method for segmented HVDC transmission lines. DC transient voltage and current signals at the sending-end of the overhead line are assumed to be available through optic measurements. DWT is then applied to DC voltage and current signals. The normalized voltage and current wavelet energies are used as the input to a binary SVM classifier for faulty section identification. The first contribution of the proposed method is that it requires measurement at only one terminal. The second contribution of the proposed method is that the SVM classifiers employ 2-dimensional input, which is less than the dimension of the inputs used in the existing methods. The faulty half is determined by comparing polarity of the first two current traveling waves once the faulty section is identified. Bewley diagrams are finally observed for the traveling wave pattern and the squared wavelet coefficients of DC voltages are used to locate the fault.

REFERENCES

[1] M. M. Saha, J. Izykowski and E. Rosolowski, *Fault Location on Power Networks*, Springer, 2010.

[2] Alstom, "*Optical Solutions for AC*" [Online]. Available: http://www.nxtphase.com/products-ac.php, March 2014.

[3] Alstom, "*Optical Solutions for DC*" [Online]. Available: http://www.nxtphase.com/products-dc.php, March 2014.

[4] ABB, "*Fiber-Optic Current Sensor*" [Online]. Available: http://www.abb.us/product/us/9AAC125572.aspx?country=US, March 2014.

[5] SEL, "*Advanced Line Differential Protection, Automation, and Control System*" [Online]. Available: https://www.selinc.com/SEL-411L/?ref=wave, March 2014.

[6] L. Coffeen, J. McBride, and D. Cantrelle, "Initial development of EHV bus transient voltage measurement: an addition to on-line transformer FRA," *EPRI Substation Equipment Diagnostics Conference*. Orlando, Mar. 2008.

[7] S. H. Horwitz and A. G. Phadke, *Power System Relaying*, Third Edition, John Wiley & Sons, 2008.

[8] S. Vasilic, *Fuzzy Neural Network Pattern Recognition Algorithm for Classification of The Events in Power System Networks*, Ph.D. Dissertation, Texas A&M University, College Station, Texas, 2004.

[9] J. De La Ree, Y. Liu, L. Mili, A. G. Phadke, and L. Dasilva, "Catastrophic failures in power systems: causes, analyses, and countermeasures," *Proc. of the IEEE*, vol. 93, no. 5, pp.956-964, May 2005.

[10] J. D. Glover, M. S. Sarma and T. J. Overbye, *Power System Analysis and Design*: Forth Edition, Thomson, 2008.

[11] H. W. Dommel, *EMTP Theory Book*, Second Edition. Vancouver, BC: Microtran Power System Analysis Corporation, 1992.

[12] C. Y. Evrenosoglu, *Novel Techniques for Fault Location, Voltage Profile Calculation and Visualization of Transients*, Ph.D. Dissertation, Texas A&M University, College Station, Texas, 2006.

[13] J. R. Marti, "Accurate modeling of frequency dependent transmission lines in electromagnetic transient simulations," *IEEE Trans. Power App. Syst*, vol. PAS-101, pp. 147-155, Jan. 1982.

[14] J. R. Carson, J.R., "Wave propagation in overhead wires with ground return," *Bell System Technical Journal*, vol. 5, pp 539-554, 1926.

[15] L. V. Bewley, *Travelling Waves on Transmission Systems*. New York: John Wiley & Sons, 1951.

[16] L. F. Woodruff, "Transmission line transients in motion movies," *AIEE Trans*, vol. 57, pp. 391-400, Jul. 1938.

[17] IEEE Standard PC37.114, *Draft Guide for Determining Fault Location on AC Transmission and Distribution Lines*. New York City, NY, 2004.

[18] T. Takagi, Y. Yamakoshi, M. Yamaura, R. Kondow and T. Matsushima, "Development of a new fault locator using the one-terminal voltage and current data," *IEEE Trans. Power App. Syst.*, vol. PAS-101, no. 8, pp. 2892–2898, Aug. 1982.

[19] L. Eriksson, M. M. Saha, and G.D. Rockfeller, "An accurate fault locator with compensation for apparent reactance in the fault resistance resulting from remote-end infeed," *IEEE Trans. Power App. Syst*., vol. PAS-104, no. 2, pp. 424–436, Feb. 1985.

[20] D. Novosel, D. G. Hart, E. Udren, and M. M. Saha, "Fault location using digital relay data," *IEEE Trans., Computer App in Power*., vol. 8, no. 3, pp. 45–50, Jul. 1995.

[21] C. E. M. Pereira, and L. C. Zanetta, "Fault location in transmission lines using one-terminal post-fault voltage data," *IEEE Trans. Power Del*., vol. 19, no. 2, pp. 603-608, Apr. 2004.

[22] M. B. Djuric, Z. M. Radojevic, and V. V. Terzija, "Distance protection and fault location utilizing only phase current phasors," *IEEE Trans. Power Del*., vol. 13, no. 4, pp. 1020-1026, Oct. 1998.

[23] A. A. Girgis, and E. B. Makram, "Application of adaptive Kalman filtering in fault classification, distance protection and fault location using microprocessors," *IEEE Trans. Power Del*., vol. 3, no. 1, pp. 301-309, Jan. 1988.

[24] Q. Zhang, Y. Zhang, W. Song, and F. Dazhong, "Transmission line fault location for single-phase-to-earth fault on non-direct-ground neutral system," *IEEE Trans. Power Del*., vol. 13, no. 4, pp. 1086-1092, Oct. 1998.

[25] Q. Zhang, Y. Zhang, W. Song, and F. Dazhong "Fault location of two-parallel transmission line for non-earth fault using one-terminal data," *IEEE Trans. Power Del*., vol. 14, no. 3, pp. 863-867, Oct. 1999

[26] Q. Zhang, Y. Zhang, W. Song, and F. Dazhong, "Transmission line fault location for double phase-to-earth fault on non-direct-ground neutral system," *IEEE Trans. Power Del*., vol. 15, no. 2, pp. 520-524, Apr. 2000.

[27] S. M. Brahma, and A. A. Girgis, "Fault location on a transmission line using synchronized voltage measurements," *IEEE Trans. Power Del*., vol. 19, no. 4, pp. 1619-1622, Oct. 2004.

[28] M. Kezunovic, and B. Perunicic , "Automated transmission line fault analysis using synchronized sampling at two ends," *IEEE Trans. Power Sys*., vol. 11, no. 1, pp. 954-960, Feb. 1996.

[29] M. Kezunovic, J. Mrkic, and B. Perunicic, "An accurate fault location algorithm using synchronized sampling," *Electric Power System Research*, vol. 29, no. 3, pp. 161-169, May. 1994.

[30] Y. H. Lin, C. W. Liu, and C. S. Chen, "A new PMU-based fault detection/location technique for transmission lines with consideration of arcing fault discrimination-part I: theory and algorithms," *IEEE Trans. Power Del*., vol. 19, no. 4, pp. 1587-1593, Oct. 2004.

[31] Y. H. Lin, C. W. Liu, and C. S. Chen, "A new PMU-based fault detection/location technique for transmission lines with consideration of arcing fault discrimination–Part II: Performance Evaluation," *IEEE Trans. Power Del*., vol. 19, no. 4, pp. 1594-1601, Oct. 2004.

[32] Y. H. Lin, C. W. Liu, and C. S. Yu, "A new fault locator for three-terminal transmission lines–using two-terminal synchronized voltage and current phasors," *IEEE Trans. Power Del*., vol. 17, no. 2, pp. 452-459, Apr. 2002.

[33] D. Novosel, D.G. Hart, E. Udren, and J. Garitty, "Unsynchronized two-terminal fault location estimation," *IEEE Trans. Power Del*., vol. 11, no. 1, pp. 130-138, Jan. 1996.

[34] A. L. Dalcastagne, S. N. Filho, H. H. Zurnet, and R. Seara, "An iterative two-terminal fault-location method based on unsynchronized phasors," *IEEE Trans. Power Del.*, vol. 23, no. 4, pp. 2318-2329, Oct. 2008.

[35] M. S. Sachdev, and R. K. Aggarwal, "A technique for estimating line fault locations from digital distance relay measurements," *IEEE Trans. Power Del.*, vol. 3, no. 1, pp. 121-129, Jan. 1988.

[36] A. Gopalakrishnan , M. Kezunovic, H. M. Mckennaet, and D. M. Hamai, "Fault location using the distributed parameter transmission line model," *IEEE Trans. Power Del.*, vol. 15, no. 4, pp. 1169-1174, Oct. 2000.

[37] Y. Liao, and N. Kang, "Fault-location algorithms without utilizing line parameters based on the distributed parameter line model," *IEEE Trans. Power Del.*, vol. 24, no. 2, pp. 579-584, Apr. 2009.

[38] Y. Liao Y, and M. Kezunovic, "Optimal estimate of transmission line fault location considering measurement errors," *IEEE Trans. Power Del.*, vol. 22, no. 3, pp. 1335-1341, Jul. 2007.

[39] G. Song, J. Suonan, Q. Xu, P. Chen, and Y. Ge, "Parallel transmission lines fault location algorithm based on differential component net," *IEEE Trans. Power Del.*, vol. 20, no. 4, pp. 2396-2406, Oct. 2005.

[40] C. E. M. Pereira, and L. C. Zanetta, "Optimization algorithm for fault location in transmission lines considering current transformers saturation," *IEEE Trans. Power Del.*, vol. 20, no. 2, pp. 603-608, Apr. 2005.

[41] A. A. Girgis, D. G. Hart and W. L. Peterson, "A new fault location technique for two- and three-terminal lines," *IEEE Trans. Power Del.*, vol. 7, no. 1, pp. 98-107, Jan. 1992.

[42] R. K. Aggarwal, D. V. Coury, A. T. Johns and A. Kalam, "A practical approach to accurate fault location on extra high voltage teed feeders," *IEEE Trans. Power Del.*, vol. 8, no. 3, pp. 874-883, Jul. 1993.

[43] T. Nagasawa, M. Abe, N. Otsuzuki, T. Emura, Y. Jikihara and M. Takeuchi, "Development of a new fault location algorithm For multi-terminal two parallel transmission lines," *IEEE Trans. Power Del.*, vol. 7, no. 3, pp. 1516-1532, Jul. 1992.

[44] Y. H. Lin, C. W. Liu and C. S. Yu, "A new fault locator for three-terminal transmission lines-using two-terminal synchronized voltage and current phasors," *IEEE Trans. Power Del.*, vol. 17, no. 2, pp. 452-459, Apr. 2002.

[45] J. Izykowski, E. Rosolowski, M. M. Saha, M. Fulczyk, and P. Balcerek, "A fault location method for application with current differential relays of three-terminal lines," *IEEE Trans. Power Del.*, vol. 22, no. 4, pp. 1169-1174, Oct. 2007.

[46] M. M. Saha, J. Izykowski, E. Rosolowski and B. Kasztenny, "A new accurate fault locating algorithm for series compensated lines," *IEEE Trans. Power Del.*, vol. 14, no. 3, pp. 789-797, Jul. 1999.

[47] C. S. Yu, C. W. Liu, S. L. Yu and J. A. Jiang, "A new PMU-based fault location algorithm for series compensated lines," *IEEE Trans. Power Del.*, vol. 17, no. 1, pp. 33-46, Jan. 2002.

[48] J. Sadeh, N. Hadjsaid, A. M. Ranjbar and R. Feuillet, "Accurate fault location algorithm for series compensated transmission lines," *IEEE Trans. Power Del.*, vol. 15, no. 3, pp. 1027-1033, Jul. 2000.

[49] M. Al-Dabbagh, and S. K. Kapuduwage, "Using instantaneous values for estimating fault locations on series compensated transmission lines," *Electric Power System Research*, vol. 76, no. 1-3, pp. 25-32, Sep. 2005.

[50] B. Lian and M. Salama, "An overview of digital fault location algorithms for power transmission lines using transient waveforms," *Electric Power System Research*, vol. 29, pp.17-25, 1994.

[51] P. A. Crossley and P. G. McLaren, "Distance protection based on traveling waves," *IEEE Trans. Power App. Syst.*, vol. PAS-102, no. 9, pp. 2971–2983, Sep. 1983.

[52] A. O. Ibe and B. J. Cory, "A travelling wave-based fault locator for two and three terminal networks," *IEEE Trans. Power Del.*, vol. PWRD-1, no. 2, pp. 283–288, Apr. 1986.

[53] F. H. Magnago and A. Abur, "Fault location using wavelets," *IEEE Trans. Power Del.*, vol. 13, no. 4, pp. 1475–1480, Oct. 1998.

[54] C. Y. Evrenosoglu and A. Abur, "Travelling wave based fault location for teed circuits," *IEEE Trans. Power Del.*, vol. 20, no. 2, pp. 1115-1121, Apr, 2005.

[55] Z. Q. Bo, M. A. Redfern, and G. C. Weller, "Positional protection of transmission line using fault generated high frequency transient signals," *IEEE Trans. Power Del.*, vol. 15, no. 3, pp. 888-894, Jul, 2000.

[56] W. Chen, O. P. Malik, X. Yin, D. Chen, and Z. Zhang, "Study of wavelet-based ultra-high speed directional transmission line protection," *IEEE Trans. Power Del.*, vol. 18, no. 4, pp. 1134-1139, Oct, 2003.

[57] D. J. Zhang, Q. H. Wu, Z. Q. Bo, and B. Caunce, "Transient positional protection of transmission lines using complex wavelets analysis," *IEEE Trans. Power Del.*, vol. 18, no. 3, pp. 705-710, Jul, 2003.

[58] M. Gilany, D. K. Ibrahim, and E. S. T. Eldin, "Traveling-wave-based fault-location scheme for multiend-aged underground cable system," *IEEE Trans. Power Del.*, vol. 22, no. 1, pp. 82-89, Jan, 2007.

[59] P. Jafarian, and M. Sanaye-Pasand, "A traveling-wave-based protection technique using wavelet/PCA analysis," *IEEE Trans. Power Del.*, vol. 25, no. 2, pp. 588-599, Apr, 2010.

[60] H. Livani and C. Y. Evrenosoglu, "A Traveling wave based single-ended fault location algorithm using DWT for overhead lines combined with underground cables," *in Proc. IEEE/PES General Meeting*, Minneapolis, Jul. 2010.

[61] M. M. Tawfik and M. M. Morcos, "ANN-based techniques for estimating fault location on transmission lines using prony method," *IEEE Trans. Power Del.*, vol. 16, no. 2, pp. 219-224, Apr, 2001.

[62] J. Gracia, A. J. Mazón, and I. Zamora, "Best ANN structures for fault location in single and double-circuit transmission lines," *IEEE Trans. Power Del.*, vol. 20, no. 4, pp. 2389-2395, Oct, 2005.

[63] M. Joorabian M, S. M. A. Taleghani-Asl, and R. K. Aggarwal, "Accurate fault locator for EHV transmission lines based on radial basis function neural networks," *Electric Power System Research*, vol. 71, no. 3, pp. 195-202, Nov. 2004.

[64] P. K. Dash, A. K. Pradhan, and G. Panda, "Novel fuzzy neural network based distance relaying scheme," *IEEE Trans. Power Del.*, vol. 15, no. 3, pp. 902-907, Oct, 2000.

[65] D. Novosel, B. Bachmann, D. Hart, Y. Hu, and M. M. Saha, "Algorithms for locating faults on series compensated lines using neural network and deterministic methods," *IEEE Trans. Power Del*., vol. 11, no. 4, pp. 1728-1736, Oct, 1996.

[66] J. Sadeh, H. Afradi, "A new and accurate fault location algorithm for combined transmission lines using adaptive network-based fuzzy inference system," *Electric Power System Research*, vol. 79, no. 11, pp. 1538-1545, Nov. 2009.

[67] R. Salat, and S. Osowski, "Accurate fault location in the power transmission line using support vector machine approach," *IEEE Trans. Power Sys*., vol. 19, no. 2, pp. 979-986, May. 2004.

[68] U. B. Parikh, B. Das and R. P. Maheshwari, "Combined wavelet-SVM technique for fault zone detection in a series compensated transmission line," *IEEE Trans. Power Del*., vol. 23, no. 4, pp. 1789-1794, Oct. 2008.

[69] A.A. Yusuffa, C. Fei, A.A. Jimoha and J.L. Munda, "Fault location in a series compensated transmission line based on wavelet packet decomposition and support vector regression," *Electric Power System Research*, vol. 81, no. 7, pp. 1258-1265, Apr. 2011.

[70] P. K. Dash, S. R. Samantaray and G. Panda, "Fault classification and section identification of an advanced series compensated transmission line using support vector machine," *IEEE Trans. Power Del*., vol. 22, no. 1, pp. 67-73, Jan. 2007.

[71] J. A. Jiang, C. L. Chuang, Y. C. Wang, C. H. Hung, J. Y. Wang, C. H. Lee and Y. T. Hsiao, "Hybrid framework for fault detection, classification, and location part I: concept, structure, and methodology," *IEEE Trans. Power Del*., vol. 26, no. 3, pp. 1988-1997, Jul. 2011.

[72] J. A. Jiang, C. L. Chuang, Y. C. Wang, C. H. Hung, J. Y. Wang, C. H. Lee and Y. T. Hsiao, "Hybrid framework for fault detection, classification, and location part II: implementation and test results," *IEEE Trans. Power Del*., vol. 26, no. 3, pp. 1999-2008, Jul. 2011.

[73] A. Grapps, "An Introduction to Wavelets," *IEEE Computational Science and Engineering*, vol. 2, no. 2, Summer 1995.

[74] C. H. Kim and R. Aggarwal, "Wavelet transforms in power systems. I. General introduction to the wavelet transforms," *Power Engineering Journal*, vol. 14, no. 2, pp. 81-87, Apr. 2000.

[75] Z. L. Gaing, "Wavelet-based neural network for power disturbance recognition and classification," *IEEE Trans. Power Del*., vol. 19, no. 4, pp. 1560-1568, Oct. 2004.

[76] S. Santoso, E. J. Powers, W. Mack Grady, and P. Hofmann, "Power quality assessment via wavelet transform analysis," *IEEE Trans. Power Del*., vol. 11, no. 3, pp. 924-930, Apr. 2011.

[77] S. J. Huang, C. T. Hsieh and C. L. Huang, "Application of Morlet wavelets to supervise power system disturbances," *IEEE Trans. Power Del*., vol. 14, no. 1, pp. 235-243, Jan. 1999.

[78] J. Barros and R. I. Diego, "Application of the wavelet-packet transform to the estimation of harmonic groups in current and voltage waveforms," *IEEE Trans. Power Del*., vol. 21, no. 1, pp. 533-535, Jan. 2006.

[79] T. Tarasiuk, "Hybrid wavelet–Fourier method for harmonics and harmonic subgroups measurement-case study," *IEEE Trans. Power Del*., vol. 22, no. 1, pp. 4-17, Jan. 2007.

[80] F. Liang and B. Jeyasurya, "Transmission line distance protection using wavelet transform algorithm," *IEEE Trans. Power Del*., vol. 19, no. 2, pp. 545-553, Apr. 2004.

[81] W. Chen, O. P. Malik, X. Yin, D. Chen, and Z. Zhang, "Study of wavelet-based ultra high speed directional transmission line protection," *IEEE Trans. Power Del*., vol. 18, no. 4, pp. 1134-1139, Oct. 2003.

[82] A. I. Megahed, A. M. Moussa, and A. E. Bayoumi, "Usage of wavelet transform in the protection of series-compensated transmission lines," *IEEE Trans. Power Del*., vol. 21, no. 3, pp. 1213-1221, Jul. 2006.

[83] X. Liu, A. H. Osman, and O. P. Malik, "Hybrid traveling wave/boundary protection for monopolar HVDC line," *IEEE Trans. Power Del*., vol. 24, no. 2, pp. 569-578, Apr. 2009.

[84] A. J. Conejo, M. A. Plazas, and A. B. Molina, "Day-ahead electricity price forecasting using the wavelet transform and ARIMA models," *IEEE Trans. Power Systs*., vol. 20, no. 2, pp. 1035-1042, May. 2005.

[85] N. M. Pindoriya, S. N. Singh, and S. K. Singh, "An adaptive wavelet neural network-based energy price forecasting in electricity markets," *IEEE Trans. Power Systs*., vol. 23, no. 3, pp. 1423-1432, Aug. 2008.

[86] P. Mandal, A. Ul Haque, J. Meng, A. K. Srivastava, and R. Martinez, "Novel hybrid approach using wavelet, firefly algorithm, and fuzzy ARTMP for day-ahead electricity price forecasting," *IEEE Trans. Power Systs*., vol. 28, no. 2, pp. 1041-1051, May. 2013.

[87] M. H. J. Bollen, I. Y. H Gu, *Signal Processing of Power Quality Disturbances*. IEEE Press, NJ, 2006.

[88] V. Vapnik, *Statistical Learning Theory*. John Wiley & Sons, NY, 1998.

[89] P. Janik and T. Lobos, "Automated classification of power-quality disturbances using SVM and RBF networks," *IEEE Trans. Power Del*., vol. 21, no. 3, pp. 1663-1669, Jul. 2006.

[90] W. M. Lin, C. H. Wu, C. H. Lin, and F. S. Cheng, "Detection and classification of multiple power quality disturbances with wavelet multiclass SVM," *IEEE Trans. Power Del*., vol. 23, no. 4, pp. 2575-2582, Oct. 2008.

[91] B. Ravikumar, D. Thukaram, and H. P. Khincha, "Comparison of multiclass SVM classification methods to use in a supportive system for distance relay coordination," *IEEE Trans. Power Del*., vol. 25, no. 3, pp. 1296-1305, Jul. 2010.

[92] Y. Zhang, M. D. Ilic, and O. K. Tonguz, "Mitigating Blackouts via Smart Relays: A Machine Learning Approach," *IEEE Proc*., vol. 99, no. 1, pp. 94-118, Jan. 2011.

[93] A. D. Rajapakse, F. Gomez, K. Nanayakkara, P. A. Crossley, and V. V. Terzija, "Rotor angle instability prediction using post-disturbance voltage trajectories," *IEEE Trans. Power Syst*., vol. 25, no. 2, pp. 947-956, May. 2010.

[94] F. R. Gomez, A. D. Rajapakse, U. D. Annakkage, and I. T. Fernando, "Support vector machine based algorithm for post-fault transient stability status prediction using synchronized measurements," *IEEE Trans. Power Syst*., vol. 26, no. 3, pp. 1474-1483, Aug. 2011.

[95] J. Hua Zhao, Z. Y. Dong, Z. Xu, and K. P. Wong, "A statistical approach for interval forecasting of the electricity price," *IEEE Trans. Power Syst*., vol. 23, no. 2, pp. 267-276, May. 2008.

[96] B. J. Chen, M. W. Chang, and C. J. Lin, "Load forecasting using support vector machines: a study on EUNITE competition 2001," *IEEE Trans. Power Syst*., vol. 19, no. 4, pp. 1821-1830, Nov. 2004.

[97] Y. Wang, Q. Xia, and C. Kang, "Secondary forecasting based on deviation analysis for short-term load forecasting," *IEEE Trans. Power Syst*., vol. 26, no. 2, pp. 500-507, May. 2011.

[98] S. Rajendra and P. G. McLaren, "Travelling-wave techniques applied to the protection of teed circuits: Multi-phase/multi-circuit system," *IEEE Trans. Power App. Syst.*, vol. PAS-104, no. 12, pp. 3351–3557, Dec. 1985.

[99] M. da Silva, D. V. Coury, M. Oleskovicz, and E. C. Segatto, "Combined solution for fault location in three-terminal lines based on wavelet transforms," *IET Gener. Transm. Distrib*, vol. 4, iss. 1, pp. 94-103, 2010.

[100] E. E. Ngu and K. Ramar, "Combined impedance and traveling wave based fault location method for multi-terminal transmission lines," *Electric Power System Research*, vol. 33, no. 10, pp. 1767-1775, Dec. 2011.

[101] H. Livani and C. Y. Evrenosoglu, "A fault classification and location method for three-terminal circuits using machine learning," *IEEE Trans. Power Del*., vol. 28, no. 4, pp. 2282-2290, Oct 2013.

[102] H. Livani and C. Y. Evrenosoglu, "A fault classification method in power systems using DWT and SVM classifier". *in Proc. IEEE/PES Trans & Dist. (T&D)*, Orlando, May 2012.

[103] M. Kizilcay and T. Pniok, "Digital simulation of fault arcs in power systems," *ETEP Journal*, vol., 1, no. 1, pp. 55-60, Jan 1991.

[104] X. Yang, M. S. Choi, S. J. Lee, C. W. Ten, and S. I. Lim, "Fault location for underground power cable using distributed parameter approach," *IEEE Trans. Power Syst*., vol. 23, no. 4, pp. 1809–1816, Nov. 2008.

[105] Z. Xu and T. S. Sidhu, "Fault location method based on single-end measurements for underground cables," *IEEE Trans. Power Del.*, vol. 26, no. 4, pp. 2845-2854, Oct. 2011.

[106] M. S. Mashikian, R. Bansal, and R. B. Northorp, "Location and characterization of partial discharge sites in shielded power cables," *IEEE Trans. Power Del.*, vol. 5, no. 2, pp. 833-839, Apr. 1990.

[107] H. E. Gallagher, D. R. Mize, and A. F. Dickerson, "Fault location system for transmission-type cable," *IEEE Trans. Power App. Syst.*, vol. PAS-101, no. 6, pp. 1700–1710, Jun. 1982.

[108] C. M. Wiggins, D. E. Thomas, T. M. Salas, F. S. Nickel, and H. W. Ng, "A novel concept for URD cable fault location," *IEEE Trans. Power Del.*, vol. 9, no. 1, pp. 591-597, Jan. 1994.

[109] N. Inoue, T. T. Tsunekage, and S. Sakai, "On-line fault location system for 66kV underground cables with fast O/E and fast A/D technique," *IEEE Trans. Power Del.*, vol. 9, no. 1, pp. 579-584, Jan. 1994.

[110] W. Zhao, Y. H. Song, and W. R. Chen, "Improved GPS traveling wave fault locator for power cables by using wavelet analysis," *International Journal of Electrical Power & Energy Systems*, vol. 23, no. 5, pp. 403-411, Jun. 2001.

[111] E. S. T. Eldin, M. M. A. Aziz, D. K. Ibrahim, and M. Gilany, "Fault location scheme for combined overhead line with underground power cable," *Electric Power System Research*, vol. 76, no. 11, pp. 928-935, Jul. 2006.

[112] C. W. Liu, T. C. Lin, C. S. Yu, and J. Z. Yang, "Fault location technique for two-terminal multi-section compound transmission lines using synchronized phasor measurements," *IEEE Trans. Smart Grid.*, vol. 3, no. 1, pp. 113-121, Mar. 2012.

[113] D. Spoor and J. G. Zhu, “Improved single-ended traveling-wave fault- location algorithm based on experience with conventional substation transducers,” *IEEE Trans. Power Del.*, vol. 21, no. 3, pp. 1714-1720, Jul. 2006.

[114] M. J. Reddy and D. K. Mohanta, “A wavelet-fuzzy combined approach for classification and location of transmission line faults,” *International Journal of Electrical Power & Energy Systems*, vol. 29, no. 9, pp. 669-678, Nov. 2007.

[115] D. Chanda, N. K. Kishore, and A. K. Sinha, “A wavelet multiresolution analysis for location of faults on transmission lines,” *International Journal of Electrical Power & Energy Systems*, vol. 25, no. 1, pp. 59-69, Jan. 2003.

[116] C. K. Jung, K. H. Kim, J. B. Lee, and B. Klöckl, “Wavelet and neuro-fuzzy based fault location for combined transmission systems,” *International Journal of Electrical Power & Energy Systems*, vol. 29, no. 6, pp. 445-454, Jul. 2007.

[117] I. Niazy and J. Sadeh, “A new single ended fault location algorithm for combined transmission line considering fault clearing transients without using line parameters,” *International Journal of Electrical Power & Energy Systems*, vol. 44, no. 1, pp. 616-623, Jan. 2013.

[118] C. K. Jung, J. B. Lee, X. H. Wang, and Y. H. Song, “Wavelet based noise cancellation technique for fault location on underground power cables,” *Electric Power System Research*, vol. 77, no. 10, pp. 1342-1369, Aug. 2007.

[119] P. S. Bhowmik, P. Purkait, and K. Bhattacharya, “A novel wavelet transform aided neural network based transmission line fault analysis method,” *International Journal of Electrical Power & Energy Systems*, vol. 31, no. 5, pp. 213-219, Jun. 2009.

[120] H. Livani and C. Y. Evrenosoglu, “A machine learning and wavelet-based fault location method for hybrid transmission lines". *IEEE Trans. Smart Grid*, vol. 5, no. 1, pp. 51-59, Jan. 2014.

[121] H. Livani and C. Y. Evrenosoglu, "A hybrid fault location method for overhead line combined with underground cable using DWT and SVM". *in Proc. IEEE/PES General Meeting*, San Diego, July 2012.

[122] S. Gordon, “Supergrid to the rescue,” *IET Pow Eng*., vol. 20, no. 5, pp. 30-33, Oct. 2006.

[123] M. Ando M, E. O. Shweitzer, and R. A. Baker, “Development and field-data evaluation of single-end fault locator for two-terminal HVDC transmission lines Part I: data collection system and field data,” *IEEE Trans. Power App Syst*., vol. PAS-104, no. 12, pp. 3524–30, Dec. 1985.

[124] M. Ando, E. O. Shweitzer, and R. A. Baker RA, “Development and field-data evaluation of single-end fault locator for two-terminal HVDC transmission lines Part II: algorithm and evaluation,” *IEEE Trans. Power App Syts*., vol. PAS-104, no. 12, pp. 3531-3537, Dec. 1985.

[125] M. B. Dewe, S. Sankar, and J. Arrillaga, “The application of satellite time references to HVDC fault location,” *IEEE Trans Power Del*., vol. 8, no. 3, pp.1295-1302, Jul. 1993.

[126] Y. Zhang, N. Tai, and B. Xu, “Fault analysis and traveling-wave protection scheme for bipolar HVDC lines,” *IEEE Trans Power Del*., vol. 27, no. 3, pp. 279-288, Jul. 2012.

[127] K. De Kerf, K. Sirvastava, M. Reza, D. Bekaert, S. Cole, D. Van Hertem, and R. Belmans, "Wavelet-based protection strategy for DC faults in multi-terminal VSC-HVDC systems," *IET Gen Trans Dist.*, vol. 5, no. 4, pp. 496-503, Sep. 2010.

[128] L. Tang L and B. T. Ooi, "Locating and isolating DC faults in multi-terminal DC systems," *IEEE Trans Power Del.*, vol. 22, no. 3, pp. 1877-1884, Jul. 2007.

[129] L. Shang, G. Herold, J. Jaeger, R. Krebs, and R. Kumar, "High-speed fault identification and protection for HVDC line using wavelet technique," *in Proc. IEEE Power Tech Conf*. Porto, Portugal, 2001.

[130] P. Chen, B. Xu, and J. Li, "A traveling wave based fault locating system for HVDC transmission lines," *in Proc. Int. Conf Power Con*, Chongqing, China, 2006.

[131] J. Suonan, S. Gao, G. Song, Z. Jiao, and X. Kang, "A novel fault-location method for HVDC transmission lines," *IEEE Trans Power Del*., vol. 25, no. 2, pp. 1203-1209, Apr. 2010.

[132] O. M. K. K. Nanayakkara, A. D. Rajapakse, and R. Wacha, "Location of DC line faults in conventional HVDC systems with segments of cables and overhead lines using terminal measurements," *IEEE Trans Power Del.*, vol. 27, no. 1, pp. 279–288, Jan. 2012.

[133] O. M. K. K. Nanayakkara, A. D. Rajapakse, and R. Wachal, "Fault location in extra long HVDC transmission lines using continuous wavelet transform," *in Proc. Power Syst Transients Conf*, Delft, The Netherlands, June, 2011.

[134] H. Livani and C. Y. Evrenosoglu, "A single-ended fault location method for segmented HVDC transmission line," *Electric Power System Research*, vol. 107, pp. 190-198, Feb 2014

APPENDIX A

CONDUCTOR AND TOWER CONFIGURATION DATA

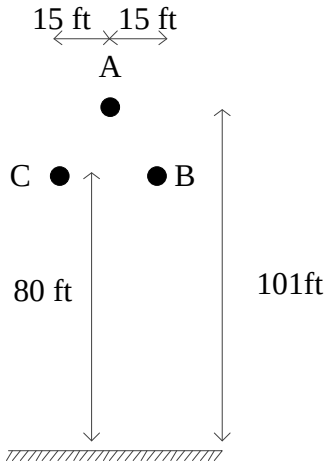

Figure 53. 20 kV transmission line tower configurations

Table 17. Data for 220 kV transmission line

Ph.	Skin	R [Ω/mi]	IX	X	D [in]	Hor. [ft]	Vtower [ft]
0	0.5	6.74	4	0	0.36	45	114
0	0.5	6.74	4	0	0.36	75	114
1	0.5	0.0984	4	0	1.196	60	101
2	0.5	0.0984	4	0	1.196	45	80
3	0.5	0.0984	4	0	1.196	75	80

Ph.	Vmid [ft]	Separ. [in]	α [deg]	NB
0	114	0	0	0
0	114	0	0	0
1	101	18	0	2
2	80	18	0	2
3	80	18	0	2

APPENDIX B

HVAC CONDUCTOR AND CABLE CONFIGURATION DATA

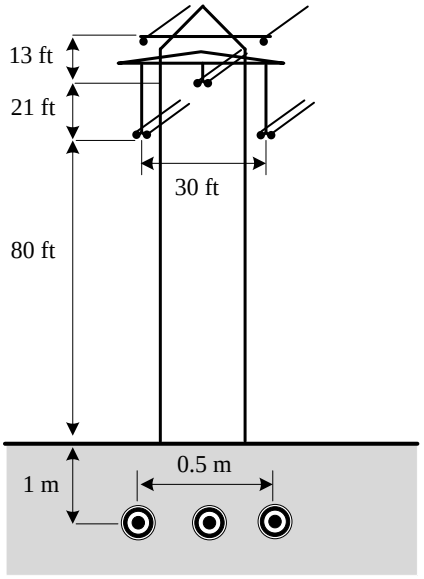

Figure 54. Overhead line tower structure and underground cable layout

Table 18. Data for 220 kV underground cable

Ph.	In. rad. core [cm]	Out. rad. core [cm]	In. rad. sheath [cm]	Out. rad. sheath [cm]	Out. rad. insul. [cm]	R_{core} [Ω-m]	R_{sheath} [Ω-m]
1	0	2.34	3.85	4.13	4.84	0.017×10^{-6}	0.21×10^{-6}
2	0	2.34	3.85	4.13	4.84	0.017×10^{-6}	0.21×10^{-6}
3	0	2.34	3.85	4.13	4.84	0.017×10^{-6}	0.21×10^{-6}

Ph.	In. insul. tanδ	Out. insul. tanδ	In. insul. ε_r	Out. insul. ε_r	All relative perm. μ_r	R_{ground} [Ω-m]
1	0.001	0.001	3.5	8	1	100
2	0.001	0.001	3.5	8	1	100
3	0.001	0.001	3.5	8	1	100

Ph.	Hor. [m]	Ver. [m]
1	0	1
2	0.25	1
3	0.5	1

APPENDIX C

HVDC CONDUCTOR AND CABLE CONFIGURATION DATA

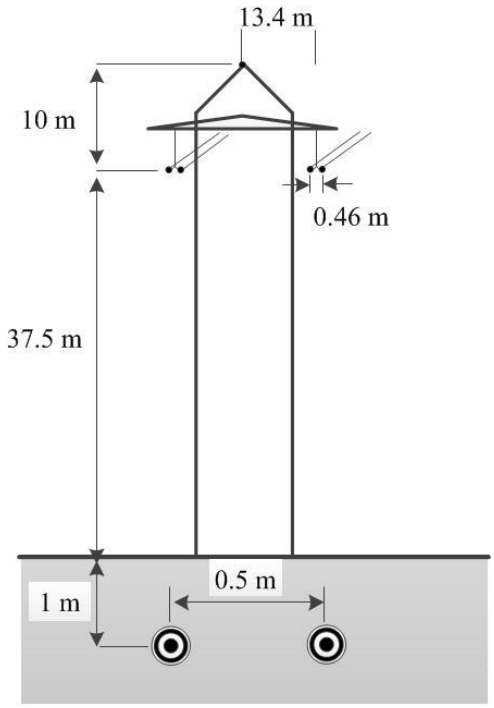

Figure 55. Overhead line tower structure and underground cable layout

Table 19. Data for HVDC underground cable

Ph.	In. rad. core [cm]	Out. rad. core [cm]	In. rad. sheath [cm]	Out. rad. sheath [cm]	Out. rad. insul. [cm]	R_{core} [Ω-m]	R_{sheath} [Ω-m]
1	0	1.04	1.6	2.05	2.15	0.0282×10^{-6}	0.0186×10^{-6}
2	0	1.04	1.6	2.05	2.15	0.0282×10^{-6}	0.0186×10^{-6}

Ph.	In. insul. tanδ	Out. insul. tanδ	In. insul. ε_r	Out. insul. ε_r	All relative perm. μ_r	R_{ground} [Ω-m]
1	0.001	0.001	4.1	2.3	1	100
2	0.001	0.001	4.1	2.3	1	100

Ph.	Hor. [m]	Ver. [m]
1	0	1
2	0.4	1